Aging, Oxidative Stress, and Schwann Cell Regulation: Implications for Neuromuscular Health

by

Steve D. Guzman

A dissertation submitted in partial fulfillment
of the requirements for the degrees of
Doctor of Philosophy
(Molecular and Integrative Physiology)
in the University of Michigan
2024

Doctoral Committee:

Professor Susan V. Brooks-Herzog, Chair
Associate Professor Carlos A. Aguilar
Professor Daniel Beard
Associate Professor Stephen C.J. Parker

Steve Derek Guzman

sdguzman@umich.edu

ORCID iD: 0000-0002-7934-7132

Dedication

To my beloved mother, Gloria Calderon, whose unyielding sacrifices for our family and unwavering belief in my potential to contribute more to the world, have been my constant source of inspiration and strength.

Acknowledgements

First and foremost, I would like to give a heartfelt thank you to my thesis advisor, Dr. Sue Brooks. You've been instrumental in keeping my enthusiasm for science alive and guiding me to mature as a scientist. Your trust in allowing me to explore my own ideas has been invaluable. More than a mentor, you've been a true friend and unwavering supporter. Also, I'm genuinely grateful to my dissertation committee for your generous time, insightful advice, and steady support. Your contributions have been crucial to my journey.

To Dr. Pete Macpherson, I cannot overstate the value of your mentorship and guidance throughout these years. Our engaging scientific discussions have been deeply enriching, and your friendship is a cornerstone of my memorable experience in the Brooks Lab. To Carol, I extend my deepest appreciation for your exceptional lab management, which significantly contributed to my focus and productivity in my research. To Lloyd, a heartfelt thank you for being an incredible friend. You have been with me through all the ups and downs, providing a sounding board for my scientific endeavors and life aspirations. To Ahmad, your dedication in the lab and passion for science have made mentoring you a truly rewarding experience. I'm thankful for the countless hours you spent working alongside me and for your steadfast belief in our shared journey. To, James, Lem, and Sunny, the knowledge I gained from each of you has been immense, and your presence made my time in the lab genuinely enjoyable. Additionally, I extend my sincere thanks to Dr. Dan Michele for your mentorship. Your invaluable guidance has been crucial in shaping my

academic path, career ambitions, and personal life. Your constant availability and willingness to support me at every turn have been deeply appreciated.

I'd like to express my deep gratitude to my friends in both Ann Arbor and Los Angeles. You have been pillars of strength for me over these years. To Jackie, I would not have come out to Ann Arbor without your trust and friendship. You are an amazing person and leader to many young Hispanic scientists around the world. To Chris, Vi, and Warren, I appreciate all those happy hotpot gatherings we had together. I am looking forward to many more to come. In addition, thank you Chris for always having my back and being an incredible friend. I'm also grateful to my peers, professors, and staff in the MIP department for fostering a family-like atmosphere that made my graduate school experience so rewarding. To my lifelong friends back in Los Angeles – Andy, Arthur, Daniel, Albert, Lupita, Santino, Karen, and Gabriel: you're more than friends, you're family and my greatest supporters. Your love and support have been crucial in maintaining my mental health.

To my family – Stephanie, Zaira, Abuelita, Tio Joel, and Mother, your unconditional love and sacrifices are the bedrock of my motivation and success. I am dedicated to making you proud with everything I do.

Lastly, to Grace, my life partner and best friend, your presence in my life continually uplifts me and makes me a better person. I am deeply grateful for your love and support.

Table of Contents

List of Tables

List of Figures

Abstract

This dissertation investigates the complex interplay between muscle-resident Schwann cells and neuromuscular junction (NMJ) maintenance and remodeling with a focus on the implications for aging-associated muscle atrophy and motor unit adaptation. The primary objective is to elucidate the cellular and molecular mechanisms underlying skeletal muscle and glial function in denervating conditions. The research employs a comprehensive approach, combining advanced in vivo and in vitro techniques, to uncover key elements that sustain NMJ integrity and overall neuromuscular health. We first examined the role of senescent cell accumulation in the decline of muscle function in aging mice. A genetic strategy to ablate p16INK4A-expressing cells in aged mice revealed that their removal at 20 months of age leads to modest preservation above untreated controls in muscle mass (+11%) and force (+11.5%) by 26 months. This finding indicates a tangible benefit of senescent cell elimination in mitigating age-associated muscle decline and suggests that changes in proliferative cell dynamics may mediate muscle health during aging. We next shifted to focus on the transcriptional responses of Schwann cells under oxidative stress and their role in modulating AChR density in muscle cells. Findings from this segment demonstrate a notable upregulation in key repair markers like *Ngfr*, *Gdnf*, and *Agrn* in Schwann cells in culture exposed to a ROS-inducing agent. Conditioned media from these cells, when applied to myotubes in vitro, not only enhanced AChR clustering but also synergistically potentiated the effects of Agrin-induced AChR clustering, indicating a direct Schwann cell-to-muscle signaling mechanism supporting post-synaptic structures. Further investigations explore Schwann cell behavior under

conditions of denervation and reinnervation in vivo using *Sod1*$^{-/-}$ mice, a recognized model of progressive NMJ degeneration. This part of the study identifies a key window for NMJ regeneration and offers a detailed single cell RNA-Sequencing analysis of muscle-resident Schwann cells. This analysis identifies multiple subpopulations of Schwann cells, including the novel identification of a synapse-promoting terminal Schwann cell (tSC) cluster that emerges during denervation. Particularly noteworthy is the discovery of enhanced secreted phosphoprotein 1 (SPP1) signaling emanating from myelin Schwann cells in denervated muscles. Validation studies showed that neutralizing intramuscular SPP1 signaling in wildtype mice with nerve injuries impaired or delayed muscle fiber reinnervation, accompanied by a reduced number of tSCs. These experiments reveal intricate gene expression profiles associated with the SPP1 pathway and Schwann cell repair mechanisms, providing a deeper understanding of muscle reinnervation processes. Overall, this dissertation synthesizes its findings to significantly advance the fields of Schwann cell biology and neuromuscular remodeling. The insights gained offer a profound step forward in our understanding of neuromuscular health. By identifying key gaps in current knowledge and suggesting future research directions, it lays the groundwork for novel therapeutic approaches targeting Schwann cells and NMJ integrity in aging and neuromuscular disorders.

Chapter 1 Introduction

1.1 Sarcopenia

As societies globally witness an increase in the size of the elderly population due to advancements in medical care, the complexities associated with aging have come under sharp focus. While life expectancy has been on a steady rise, the quality of those added years, termed 'healthspan', has not shown a proportionate improvement[1]. A striking manifestation of this discrepancy is the phenomenon of sarcopenia – a severe decline in skeletal muscle mass, strength, and functionality that shadows the aging process. Sarcopenia is not merely an age-related inconvenience but a profound health challenge. Between the ages of 50 and 80, individuals experience a staggering loss of 30-50% of their muscle mass, leading to a consequential reduction in strength[2]. The repercussions of this muscle degeneration are far-reaching in their prevalence, clinical implications, and societal impacts. Initial symptoms of sarcopenia can be observed in 5-13% of individuals aged between 60-70 years[3]. Alarmingly, by the time they cross 80, this number escalates to encompass half of the population. The diminished muscle strength heightens the risk of falls, drastically reduces mobility, and often culminates in the loss of independence. Such physical vulnerabilities significantly elevate mortality rates among the elderly. Beyond the personal toll, sarcopenia places considerable strain on healthcare systems and societal structures, emphasizing the urgent need for targeted interventions[4]. The present effective strategies to counteract sarcopenia predominantly revolve around exercise regimes[5,6]. While exercise can elicit adaptations even at advanced ages, it is only partially effective for preventing sarcopenia and

participation in vigorous exercise is not universally feasible. Thus, the quest for alternative interventions is paramount.

Consensus in the medical and research communities posits that degenerative alterations at the neuromuscular junctions (NMJ) represent a pivotal early event that in the initiation of sarcopenia[7]. The NMJ, serving the communication hub between motor nerves and muscles, plays a crucial role in muscle contraction and overall function. The NMJ is the final synapse of the neuromuscular system, comprising of the pre-synaptic motor neuron, the post-synaptic muscle fiber, and the terminal Schwann cells (or perisynaptic Schwann cells) that cap the junction. The deterioration of NMJs with aging severely impairs muscle functionality, advancing the onset of sarcopenia[8]. However, the specific triggers and underlying mechanisms responsible for NMJ degeneration remain poorly understood. The NMJ is a complex structure and like many other physiological entities undergoes turnover and remodeling through the lifespan of an organism, consisting of early NMJ development, postnatal maturation, maintenance and ultimately late-life associated remodeling.

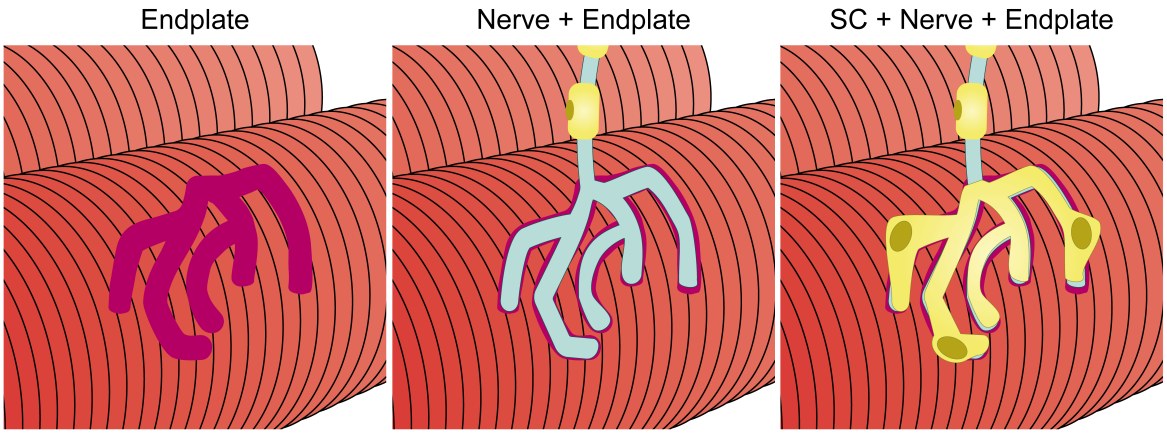

Figure 1.1: Depictions of the tripartite cellular components of the neuromuscular junction. The postsynaptic element consists of clusters of acetylcholine receptors (AChR) highlighted in red at the muscle endplate, which is innervated by a singular motor axon terminal depicted in blue. Overlying this structure, terminal Schwann cells, illustrated in yellow, envelop the neuromuscular junction, offering critical support to this synaptic interface.

1.2 NMJ remodeling

During embryonic development, motor neuron axons grow out from the spinal cord and search for their target muscle fibers[9]. Once they connect with a muscle fiber, a synaptic site is chosen, and the NMJ begins to form. A key protein in early NMJ development is Agrin, a proteoglycan made and secreted by motor neurons[10]. Agrin binds to LRP-4 and signals to the Muscle-Specific Kinase (MuSK) on the muscle cell membrane[11–13]. This binding activates a signaling cascade that leads to the clustering of acetylcholine receptors (AChRs) and other proteins necessary for NMJ function[14]. In the initial stages, more than one motor neuron may innervate a single muscle fiber. However, through competition, one neuron usually dominates, and the others retract[15].

Post-synaptically, early in development, there's a notable isoform switch in the nicotinic AChR at the NMJ. Initially, the embryonic AChR, composed of α2βγδ subunits, dominates. However, postnatally, the γ subunit is replaced by the ε subunit, transitioning to an α2βεδ configuration, the adult form[16]. This ε-AChR not only accelerates the AChR channel's responses but also resists calcium blockage. In the embryonic form, the presence of calcium ions can partially block the AChR channels, which modulates the strength and duration of muscle contractions. However, the adult form with the ε subunit is less susceptible to this blockage, ensuring more efficient and consistent neuromuscular transmission[17]. Concurrently, the NMJ's structure matures from its initial plaque-like form to a more intricate "pretzel-like" morphology, optimizing surface area for increased AChR density and efficient neurotransmission[18]. This mature NMJ retains significant plasticity, vital for its adaptability to alterations in muscle activity or injury. Such adaptability is reflected in the capacity to modulate AChR density on the post-synaptic membrane in response to neural activity changes and to adjust neurotransmitter vesicle release pre-

synaptically for maintaining function[19]. Furthermore, depending on the muscle activity, muscle fiber type composition may undergo transitions, influencing NMJ morphology and functionality[20]. This intricate dance of molecular and structural adaptations ensures that the NMJ facilitates optimal neuromuscular communication throughout life.

As organisms age, NMJs can become fragmented. Instead of the mature, pretzel-like shape, the NMJ may appear as multiple smaller plaques. This fragmentation may have the potential to affect neuromuscular transmission efficiency or NMJ fatigue, however, more detailed experiments are required to develop clear correlations of NMJ structure and function. Nevertheless, the remodeling of AChR clusters into smaller fragments is reliably observed after lack of physical activity and after nerve and muscle injury[6,21,22]. Aging is also associated with a reduction in the density of AChRs, potentially leading to reduced muscle strength and responsiveness[23]. In addition to these post-synaptic changes, NMJs that lack innervation accumulate in skeletal muscle during aging; however, neighboring healthy neurons can send out sprouts to reinnervate the orphaned fibers, a process termed collateral reinnervation[24]. Although the process of collateral reinnervation is an effective compensatory mechanism for retaining muscle fibers and preserving muscle function, mechanisms that regulate this remodeling are poorly understood. Understanding these remodeling events throughout life is critical as disruptions in these processes can lead to the denervation-induced muscle fiber loss associated with some neuromuscular disorders. Moreover, gaining mechanistic insights into the NMJ morphological changes can pave the way for therapeutic strategies to combat age-related neuromuscular degeneration and muscle weakness.

1.2 Motor unit remodeling and expansion as a mechanism to rescue denervated muscle fibers and muscle function

Within muscle tissue, muscle fibers are arranged into motor units, consisting of a single motor neuron and the muscle fibers it innervates[25] (**Figure 1.2A**). When activated by an action potential, the muscle fibers within a motor unit contract synchronously making the motor unit the foundational element of muscle physiology as the smallest amount of muscle that can be activated voluntarily in vivo. The dispersion of the fibers within a motor unit throughout the muscle ensures coordination and unison in contraction. Smaller motor units, innervating fewer muscle fibers, govern fine motor control such as finger movements, while larger ones, associated with more fibers, drive forceful movements typical in limbs[26].

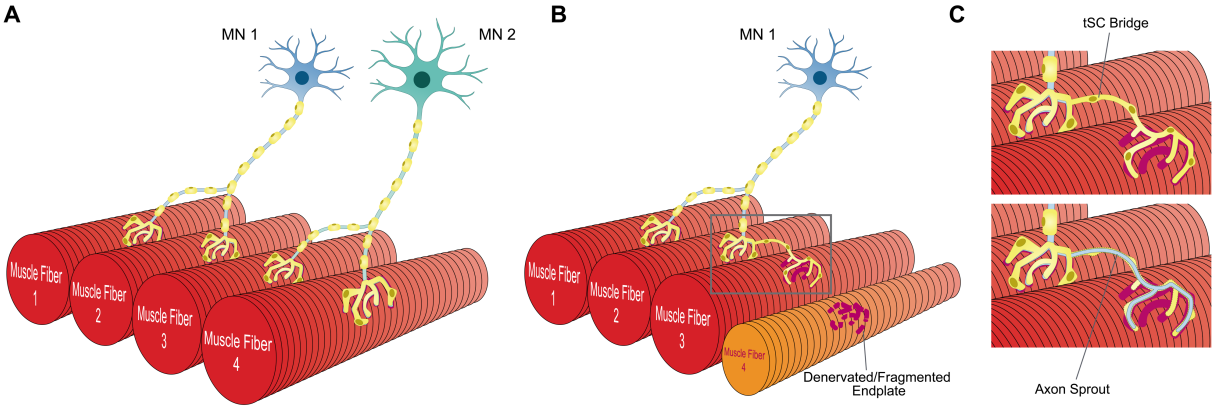

Figure 1.2: Visual representation of motor unit architecture and dynamics. (**A**) Shows two motor units, each consisting of a motor neuron (MN) connected to a pair of muscle fibers. (**B**) Illustrates motor unit remodeling and expansion, highlighting the scenario where Muscle Fiber 4 experiences denervation, leading to a degenerated muscle endplate, while Muscle Fiber 3 is being co-opted by Motor Unit 1 for reinnervation. (**C**) Demonstrates the process of motor unit expansion facilitated by terminal Schwann cells (tSC), which extend their cytoplasmic projections to form bridges to neighboring muscle endplates, thus enabling axonal sprouts from NMJ 2 to connect with and reinnervate the denervated NMJ 3.

Denervation, the process whereby muscles lose their nerve supply, can stem from various causes including trauma, neurodegenerative diseases like amyotrophic lateral sclerosis (ALS), or aging. Denervated muscle fibers are incapacitated from voluntary contraction and, over time,

atrophy and can be lost, resulting in muscle weakness or even paralysis[27,28]. However, the body's inherent resilience is exemplified by motor unit remodeling, a mechanism that entails the 're-wiring' of denervated muscle fibers (**Figure 1.2B,C**). A seminal study in the 1970s delineated this process; after inducing partial denervation by destroying specific motor axons innervating a muscle, it was observed that the residual motor neurons produced new axonal sprouts. These sprouts subsequently reinnervated the orphaned muscle fibers, effectively rescuing them from impending atrophy[29].

This phenomenon of axonal sprouting culminates in the expansion of the motor unit, with the motor neuron now commanding its innate muscle fibers in addition to the reclaimed ones. This adaptation, while serving the dual purpose of functional recovery and atrophy prevention, has inherent constraints. The sprouting maintains muscle fibers and potentially recuperates lost muscular function. Concurrently, it preempts or ameliorates muscle atrophy by restoring nerve supply[29]. However, as motor units enlarge due to this compensatory mechanism, they innervate more fibers, compromising the precision of muscle control by limiting the capacity for fine motor movements. This has been observed in studies of small hand muscles where MU remodeling was associated with reduced coordination of finger movements[30–32]. The capacity for motor unit expansion in young healthy muscle is extremely robust, but with aging and disease the expanded motor units reach their compensatory threshold, beyond which muscle weakness and atrophy escalate[33,34]. This dichotomy is starkly evident in progressive neuromuscular conditions like ALS and sarcopenia. Although initial motor unit expansion occurs as a protective response, the relentless attrition of motor neurons eventually precipitates muscle denervation, with subsequent atrophy and muscle weakness becoming inevitable[35].

Motor unit expansion differs from recoverable nerve injuries that induce temporary damage without causing irreversible disruption to the nerve's structural continuity. One classical example is the nerve crush injury, where an external force compresses the nerve, but the essential architecture, especially the epineurium surrounding the axon bundles, remains intact[36]. Unlike nerve transection injuries, where the nerve is completely cut, recoverable injuries preserve the neural pathway, setting the stage for potential regeneration[37–39]. Both motor unit expansion and recoverable nerve injury responses depend on similar biological processes involving the activation of Schwann cell mediated responses, further highlighted in the proceeding sections.

1.3 The role of terminal Schwann cells in seeking and guiding axons from innervated motor units to denervated synapses

Terminal Schwann cells (tSCs) are specialized glial cells that cover the neuromuscular junction (NMJ). Over the years, evidence has accumulated suggesting that tSCs play an active role in NMJ maintenance, regeneration, and the reinnervation of denervated muscle fibers[40–44]. With the advent of in vivo imaging techniques, researchers have been able to directly observe the behavior of tSCs following nerve injury. In one such study from the Thompson Lab, tSCs were observed to extend processes in search of axons after acute nerve injury in transgenic mice with fluorescently labeled tSCs[45]. These studies highlighted that tSCs actively seek out and align with regenerating axons, directing them to denervated synapses. When a muscle fiber becomes denervated, such as after a nerve injury, the associated tSCs undergo several morphological and biochemical changes[44]. These cells extend processes, often referred to as "bridges", which seem to actively seek out and guide regenerating motor neuron axons back to the denervated muscle fibers. In cases of more severe nerve damage, tSCs, in conjunction with other Schwann cells, form

structures called Bands of Büngner [43,45] . These structures serve as physical and molecular pathways to guide regenerating axons to their appropriate targets.

Molecular signals that Schwann cells use to communicate with regenerating axons have been identified, with neurotrophic factors such as brain-derived neurotrophic factor (BDNF) and glial cell line-derived neurotrophic factor (GDNF) playing pivotal roles. These factors are released by Schwann cells and are essential for supporting and guiding the growth of axons during regeneration after nerve injury[46–48]. The gene expression of GDNF, in particular, exhibits a marked increase in denervated rat skeletal muscle 1-2 weeks after axotomy, indicating its role in the initial stages of nerve repair[49]. When comparing GDNF gene expression under a variety of muscle conditions, ranging from healthy tissues to those that were denervated, denervated with sensory protection, or had immediate re-innervation. In denervated muscle, GDNF expression was markedly elevated, reinforcing the concept that GDNF upregulation is closely associated with the reinnervation process, whereas healthy muscle displayed the lowest levels of GDNF expression[50]. Interesting, overexpression of GDNF by skeletal muscle fibers, under the control of myogenin promotor, results in hyperinnervation of the NMJ marked by polyinnervation of 2 or more axons per NMJ[51]. The implications of GDNF promoting muscle innervation become even more pronounced when considering the aging process. Following injury, GDNF expression was lower in nerve extracts from older mice compared to those from younger mice[52]. This reduction in GDNF could contribute to the less efficient reinnervation observed in aged muscles, where there is often a prolonged phase of denervation, potentially exacerbating the muscle fiber atrophy. Studies comparing young and old animals found that tSCs in aged animals have a diminished capacity to guide axonal regeneration, possibly due to reduced expression of key neurotrophic factors[53,54], however, it is unknown whether tSC trophic gene expression is reduced with aging.

Netrin and Growth Associated Protein 43 (GAP-43) are two critical molecules implicated in nerve regeneration processes, both exhibiting intricate interactions with Schwann cells[55,56] . Netrin, a family of laminin-related secreted proteins, plays a pivotal role in numerous cellular functions, including axonal guidance, cell migration, morphogenesis, and angiogenesis[57]. In relation to axonal guidance, netrin-1 can have both attractive and repulsive effects on axons. When interacting with the Deleted in Colorectal Cancer (DCC) receptor or the Neogenin receptor, netrin-1 serves as an attractant for axons[58]. Release of netrin-1 from Schwann cells along with its action as a chemoattractant for axons, guiding axon growth cones toward their target sites has been demonstrated[59]. In the context of injury, Schwann cells upregulate netrin-1, creating a gradient that helps regenerating axons navigate through the injury site[55]. Conversely, netrin-1 repels axons when binding to the Uncoordinated receptor family, specifically Unc5 receptors[60]. In vivo siRNA mediated DCC mRNA inhibition at the growing tips of injured sciatic nerves has been reported to hinder Schwann cell activation, leading to a notable reduction in axon regeneration. The suppression of DCC coincides with an increase in Unc5H2 expression in the unaffected SCs. Interestingly, when Unc5H2 was specifically knocked down at the site of injury, axonal regrowth was enhanced, suggesting that Unc5H2 inherently acts as a brake for nerve regeneration[61].

GAP-43 is a key protein, particularly in the context of axonal regeneration and growth cone dynamics. GAP-43 is found abundantly within growth cones and plays a vital role in the intricate processes that guide an axon's trajectory towards its synaptic targets[62]. This protein's association with actin filaments is believed to be central to the growth cone's structural adaptability, which in turn affects its ability to respond to navigational cues[63]. In vivo studies using mouse models have elucidated the role of GAP-43 in axonal regeneration following trauma. These studies have shown that injury-induced upregulation of GAP-43, such as after a sciatic nerve crush or induced paralysis

via botulinum toxin A (BotA), correlates with an increase in neurite extension. Furthermore, overexpression of GAP43 was shown to potentiate neurite growth, suggesting a dose-dependent response of axonal repair mechanisms.[64] In vitro studies employing cultured neurons from GAP-43 knockout mice further supported these findings. These neurons exhibited growth cones with compromised spread and stability, highlighting the direct involvement of GAP-43 in modulating growth cone morphology[65]. Moreover, in hippocampal neurons, an increase in GAP-43 phosphorylation was directly correlated with an increase in growth cone mobility and axonal elongation[66]. GAP-43 knockout mice have been paramount in elucidating the protein's influence on axonal regeneration and neural plasticity in vivo. This model has consistently shown that in the absence of GAP-43, deficits in axonal recovery post-injury, as well as in specific synaptic plasticity processes such as long-term potentiation are observed[67]. Recent findings also indicate that GAP-43 functions beyond axonal guidance, as it interacts with other signaling pathways like PKC and calmodulin-dependent protein kinase II (CaMKII), which have known roles in growth cone dynamics[68]. Collectively, these insights emphasize the fundamental role of GAP-43 in the mechanisms underpinning axonal growth, guidance, and regeneration. While GAP-43 is prominently observed in axon growth cones, it is also found in terminal Schwann cells (tSCs) after nerve injury[56]. The exact role of GAP-43 in tSCs is not fully elucidated, but its presence in these cells hints at its importance in nerve repair processes.

1.4 Regulation of Schwann cell function

Despite the importance of Schwann cells in promoting nerve regeneration and muscle fiber reinnervation, understanding of Schwann cell biology and physiology remains incomplete. Schwann cell function is governed by a range of cellular and molecular regulators, extensively studied during developmental stages and nerve regeneration in adult rodents[69]. Yet, knowledge of

the molecular regulators and regulation of tSCs is limited, largely due to their rarity and the technical challenges associated with their isolation and the study of specific molecular pathways. One characteristic of Schwann cells that is clear is their notable plasticity, which allows them to dedifferentiate into progenitor states or transdifferentiate into repair-specific phenotypes[70]. This section focuses on some known regulatory factors that drive Schwann cell dedifferentiation and promote the repair phenotype after muscle denervation and associated with the studies described in this dissertation.

Redox Regulation

Reactive oxygen species (ROS) have emerged as critical regulators of tSC activity, particularly in response to nerve injury. A significant player in this regulatory network is hydrogen peroxide (H_2O_2), a stable ROS derived from stressed cellular mitochondria. In the context of motor axon terminal damage, mitochondria release substantial amounts of H_2O_2[71]. Given the intimate association between axon terminals and tSCs within NMJs, H_2O_2 can readily permeate to tSCs before being neutralized by cellular antioxidant systems. Within tSCs, H_2O_2 serves as a second messenger, initiating signal transduction via the chemoselective oxidation of specific cysteine residues in signaling proteins and activating the ERK pathway[71]. This is consistent with research demonstrating the role of H_2O_2 as a chemoattractant in the context of injury in other cell types and its contribution to cellular proliferation and regeneration[72–75]. In studies using neurotoxins, degenerating nerve terminals were found to release H_2O_2 of mitochondrial origin, which in activate MAPK signaling pathway, both in vitro and in vivo[71,75]. The importance of H_2O_2 in this scenario is further emphasized by observations that reducing H_2O_2 activity, such as via the application of catalase, hinders nerve regeneration in vitro[71]. Beyond H_2O_2, other mitochondrial alarmins like

mtDNA and Cytochrome c have been implicated in tSC activation post nerve injury. Collectively, these findings underscore the multifaceted role of ROS, especially H_2O_2, in regulating tSC behavior during nerve degeneration and subsequent regeneration.

Mitogen-activated protein kinase/extracellular signal-regulated kinase

The MAPK/ERK (Mitogen-activated protein kinase/extracellular signal-regulated kinase) pathway is a central signaling cascade implicated in numerous cellular processes, including proliferation, differentiation, and survival[76,77]. In Schwann cells, the MAPK/ERK pathway has been identified as a primary regulator of dedifferentiation[78] , a process by which differentiated Schwann cells revert to an immature cell progenitor state, characterized by increased proliferative capacity and the ability to support nerve regeneration. The activation of Schwann cells begins post-nerve injury when axonal connections to Schwann cells are disrupted and the Schwann cells enter a state of plasticity where they undergo molecular and morphological changes, characterized by demyelination and elongation. After nerve injury, there is an upregulation in the activity of the ERK1/2 proteins in Schwann cells[78,79]. Active ERK1/2 is localized primarily in the nuclei of Schwann cells in the injured nerve. Importantly, inhibiting the ERK pathway reduces the ability of Schwann cells to dedifferentiate and revert to a more progenitor-like state. Moreover, the upregulation of the transcription factor c-Jun, which is downstream of the MAPK/ERK pathway, is essential for Schwann cell dedifferentiation[80]. Elevated levels of c-Jun repress myelin-specific gene expression, further illustrating the complex interplay of molecular events following nerve injury. Inhibition of the MAPK/ERK pathway, can impair Schwann cell dedifferentiation and negatively impact nerve regeneration, highlighting the pathway's therapeutic potential in enhancing peripheral nerve repair. The roles of MAPK/ERK and c-Jun in muscle-resident

Schwann cells are not well-understood, yet the Durregotti et al. (2012) study indicates that MAPK/ERK plays a crucial role in the dedifferentiation of perisynaptic Schwann cells. This underscores the adaptability of the MAPK/ERK pathway in driving dedifferentiation in both myelinating and non-myelinating Schwann cells.

Trophic regulation and the repair phenotype

The Nerve Growth Factor Receptor (NGFR) or $p75^{NTR}$ is a central player in the sophisticated molecular Schwann cell mediated response that unfolds following peripheral nerve injuries. Typically, Schwann cells, in response to nerve damage, undergo a transition from a myelinating phenotype to a repair specific molecular signature, characterized by altered molecular marker expression[69]. Prominent in this altered landscape is the marked elevation of NGFR expression[69,81]. NGFR is a versatile repair-associated receptor that contains a broad ligand binding portfolio, predominantly featuring members of the neurotrophin family. This includes ligands such as Nerve Growth Factor (NGF), Brain-Derived Neurotrophic Factor (BDNF), Neurotrophin-3 (NT-3), and Neurotrophin-4/5 (NT-4/5)[82]. These neurotrophins, primarily synthesized by neurons, hold the reins to vital processes including neuronal survival, differentiation, and axonal extension. Interestingly, their expression isn't limited to neurons but spans to other cell types like Schwann cells, muscle fibers, and specific immune cells, underlining their multifaceted role in the post-injury milieu[83].

The dynamic interplay between neurotrophins and NGFR is intricate and context dependent. For instance, NGF binding to NGFR can dictate the balance between Schwann cell survival and apoptosis. Meanwhile, interactions with BDNF and NT-3 have implications for cellular differentiation and synaptic dynamics[84] . Following nerve injuries, the surge in NGFR

expression in Schwann cells is synchronous with neurotrophin release, leading to a cascade of autocrine and paracrine signals that are instrumental for nerve repair[85].

The engagement of NGFR with its ligands instigates a series of intracellular events. Though devoid of intrinsic kinase activity, the NGFR signaling is mediated by its association with various adaptor proteins and co-receptors. A notable sequence involves the recruitment of TRAF6 upon neurotrophin binding, ensuing in a cascade that activates the IKK complex, culminating in NF-κB's nuclear translocation to modulate gene expressions[86]. Concurrently, the JNK pathway, known for its role in apoptosis, is initiated. This pathway's activation results in the upregulation of pro-apoptotic genes, steered by the phosphorylation and nuclear translocation of JNK[87]. The cellular fate, be it survival or apoptosis, post neurotrophin binding to NGFR, hinges on a delicate balance of these pathways, the cellular environment, co-receptor presence, and the specific neurotrophin in question.

The multifaceted roles of NGFR, ranging from guiding Schwann cell phenotypic transitions to coordinating intricate ligand interactions, demonstrates its critical role in nerve repair. Furthermore, its potential as a biomarker for Schwann cell repair phenotypes accentuates its clinical and biological significance[88]. A thorough understanding of the NGFR expression profile across cell types is crucial for leveraging its therapeutic potential in peripheral nerve repair strategies.

Cellular Senescence

Cellular senescence is a state of irreversible cell cycle arrest, a phenomenon originally identified in human fibroblasts undergoing finite population doublings in culture[89]. While historically associated with age-related decline, senescence is now understood as a multifaceted biological response that can be triggered by various stressors, such as DNA damage, oxidative

stress, and telomere shortening. Though it has evolved as a tumor-suppressive mechanism, paradoxically, its accumulation has been implicated in driving various aspects of aging and age-related diseases, including the decline of certain facets of skeletal muscle function. A hallmark of senescent cells is their resistance to apoptotic signals and the secretion of a complex mixture of bioactive molecules, referred to as the senescence-associated secretory phenotype (SASP). This SASP includes pro-inflammatory cytokines, chemokines, growth factors, and proteases[90]. On a molecular level, pathways such as p53/p21 and $p16^{INK4a}$/RB are frequently activated in senescent cells, ensuring cell cycle arrest.

Although skeletal muscle is considered a post-mitotic tissue based on the generally accepted view that myonuclei do not divide, muscle is a highly dynamic and regenerative tissue that relies on numerous proliferative cell types to maintain homeostasis. For example, a pool of muscle stem cells (satellite cells) is required for repair following muscle fiber damage and proliferating Schwann cells are critical for motor unit remodeling and reinnervation in denervating conditions. With advancing age, the number and function of satellite cells declines, with many adopting a senescent phenotype[54] that may contribute to the diminished regenerative capability of aged muscles. The SASP from senescent muscle cells may further exacerbate muscle aging, by the creation of a chronic low-grade inflammatory environment, which has been linked to muscle atrophy, and fibrosis[91]. Clearing senescent cells or modulating the SASP are emerging as promising strategies to combat age-related diseases. Drugs known as senolytics, which selectively induce apoptosis in senescent cells, have shown potential in rejuvenating tissues, including skeletal muscle[92]. Additionally, interventions targeting SASP components could mitigate its deleterious effects on muscle function. Whether cell senescence is a factor in the depletion of tSCs from NMJs in muscles of old animals has not been examined.

1.5 Goals of thesis and outline of chapters

The preceding discussion on NMJ remodeling highlights several unresolved issues pertaining to the cellular biology physiology of muscle-resident Schwann cells. It also raises questions about how changes in the regulatory mechanisms of these cells—or potentially other proliferative cell types—may contribute to muscle atrophy associated with denervation in aging, and the extent to which they may restrict the expansion of motor units in the elderly or in conditions marked by the loss of muscle fiber innervation. The experimental work presented in this thesis aims to fill these knowledge voids by methodically investigating the complex cell and molecular biology that underpins skeletal muscle and associated glial function. This research places particular emphasis on the aging process, response to oxidative stress, and neuromuscular recovery mechanisms. Employing cutting-edge in vivo and in vitro techniques, the studies aim to pinpoint critical elements that maintain NMJ integrity and overall neuromuscular health in mouse models.

Chapter 2 details investigations asking the question of whether the accumulation of senescent cells during aging contributes to declining skeletal muscle function in aged mice. We specifically targeted and removed p16(INK4A)-expressing cells in 20-month-old mice and subsequently assessed muscle function, chemokine levels, and quantified intramuscular stem cells and macrophages at 26 months. The results underscore the potential therapeutic merits of senescent cell elimination in older mice and highlight the significance of proliferating cells attenuated with age.

In Chapter 3, the focus shifts to investigations of one particular proliferating cell type in skeletal muscle. Schwann cells and glial cells critical for the nerve-muscle axis, known for their *proliferative* response during motor unit and NMJ structural remodeling. The experiments described in this chapter studied Schwann cells in culture and aimed to define the transcriptional

responses of Schwann cells under oxidative stress conditions, and the potentiality of Schwann cell-derived factors in augmenting AChR density within muscle cells.

Chapter 4 addresses similar question of the cellular and molecular regulation of Schwann cells under conditions of denervation and reinnervation in vivo. Using young Sod1 deficient mice (*Sod1*$^{-/-}$ mice), a widely studied model of chronic in vivo oxidative stress and progressive NMJ degeneration, we scrutinized NMJ remodeling during a defined 'regenerative window' and discerned the dynamics of muscle-resident Schwann cells during denervation/reinnervation events. Methodologies encompassed muscle mechanics, NMJ high-resolution imaging, and single cell RNA-Sequencing (scRNA-Seq) of muscle-resident Schwann cells and other skeletal muscle mononuclear cells. This chapter sheds light on a novel temporal window within the lifespan of *Sod1*$^{-/-}$ mice, critical for identifying regulators of NMJ regeneration, and offers an extensive scRNA-Seq dataset of muscle-resident Schwann cells, including tSCs. The scRNA-Seq analysis further uncovers a unique cellular origin of secreted phosphoprotein 1 (SPP1) signaling from myelin Schwann cells (mSCs) targeting tSCs.

In Chapter 5, we present validation studies conducted on wildtype mice subjected to nerve injuries, aiming to determine the role of SPP1 signaling in Schwann cell-mediated muscle reinnervation. We detail our findings on the gene expression profiles associated with the SPP1 pathway and the repair phenotype of Schwann cells following nerve injury. Further, we evaluate the effects of inhibiting intramuscular SPP1 post peroneal nerve injury, probing its significance in muscle reinnervation and its potential modulation of tSCs.

Chapter 6 offers a synthesis of the contributions of this thesis to the fields of Schwann cell biology and aging highlighting important knowledge gaps that the work helps to fill. The chapter also outlines avenues for future research supported by this work

Chapter 2 Removal of *p16^{INK4}* Expressing Cells in Late-Age Mice has Moderate Effects on Skeletal Muscle Function

2.1 Abstract

Aging results in the progressive accumulation of senescent cells in tissues that display loss of proliferative capacity and acquire a senescence-associated secretory phenotype (SASP). The tumor suppressor, p16^{INK4A}, which slows the progression of the cell cycle, is highly expressed in most senescent cells and the removal of p16-expressing cells has been shown to be beneficial to tissue health. Although much work has been done to assess the effects of cellular senescence on a variety of different organs, little is known about the effects on skeletal muscle and whether reducing cellular senescent load would provide a therapeutic benefit against age-related muscle functional decline. We hypothesized that whole-body ablation of p16-expressing cells in the advanced stages of life in mice would provide a therapeutic benefit to skeletal muscle structure and function. Treatment of transgenic p16-3MR mice with ganciclovir (GCV) from 20-26 months of age resulted in reduced p16 mRNA levels in muscle. At 26 months of age, the masses of tibialis anterior, extensor digitorum longus, gastrocnemius and quadriceps muscles were significantly larger in GCV-treated compared with vehicle-treated mice, but this effect was limited to male mice. Maximum isometric force for gastrocnemius muscles was also greater in GCV-treated male mice compared to controls. Further examination of muscles of GCV- and vehicle-treated mice showed fewer CD68-positive macrophages present in the tissue following GCV treatment. Plasma cytokine levels were also measured with only one, granulocyte colony stimulating factor (G-CSF),

out of 22 chemokines analyzed was reduced in GCV-treated mice. These findings show that genetic ablation of $p16^{+}$ senescent cells provides moderate and sex specific therapeutic benefits to muscle mass and function.

2.2 Introduction

Biological aging is characterized by the progressive accumulation of tissue damage that leads to an overall reduction in both lifespan and healthspan. Unlike congenital diseases that can be attributed to a single gene mutation, the dysfunction and pathologies that accompany aging are a result of abnormalities in many cellular and molecular processes. These include genomic instability, telomere attrition, mitochondrial dysfunction, stem cell exhaustion, loss of proteostasis, and cellular senescence [94].

The cellular and molecular processes associated with organismal aging contribute to tissue aging in varying degrees and temporal onsets depending on the organ, as well as hereditary and environmental factors [95–97]. With skeletal muscle aging, there are several broad clinical and physiological presentations that are associated with frailty. These hallmarks consist of a progressive decline in muscle mass and resultant decrease in strength, termed sarcopenia [98,99]. Currently, the only available and effective interventions for ameliorating age-associated muscle loss are caloric restriction and exercise [100]. Thus, there is a critical need to elucidate the mechanisms responsible for age-related muscle atrophy and weakness to develop more effective and broadly applicable treatments for increasing healthspan.

---

[93]This chapter has been published in the journal of *Frontiers in Aging*: **Guzman, S. D**., Judge, J., Shigdar, S. M., Paul, T. A., Davis, C. S., Macpherson, P. C., Markworth, J. F., van Remmen, H., Richardson, A., McArdle, A., & Brooks, S. v. (2021). Removal of p16 INK4 Expressing Cells in Late Life has Moderate Beneficial Effects on Skeletal Muscle Function in Male Mice. *Frontiers in Aging*, *2*, 821904. https://doi.org/10.3389/FRAGI.2021.821904/

Cellular senescence is characterized by a terminal state of cell growth and has been shown to contribute to the aging process in many different tissues [101]. Upon entering the state of cellular senescence, cells adopt a senescence associate secretory phenotype (SASP), which involves an upregulation of pro-inflammatory cytokine expression and protein secretion that further reinforces the cellular senescence program in cells within the microenvironment [102]. Reducing cellular senescence appears to improve physical performance in old age [103–105]. Furthermore, repression of cellular senescence through $p16^{INK4A}$ silencing and inhibition of reactive oxygen species (ROS) generation in muscle stem cells has been found to improve stem cell quiescence and autophagy [106,107]. To date there are few studies investigating the impact of cellular senescence directly on age-associated muscle atrophy and weakness.

In the present study, we assessed muscle function in an aged genetic mouse model (p16-3MR) in which $p16^{INK4A}$-expressing senescent cells can be eliminated upon treatment with the drug ganciclovir (GCV). Here we show that male p16-3MR mice treated with GCV starting at 20-months of age through to 26-months of age exhibited reduced muscle atrophy and increased force generation in select hindlimb muscles compared with vehicle-treated mice in which p16-expressing cells were not deleted.

2.3 Materials and Methods

2.3.1 Animals

Aged p16-3MR mice were obtained from the laboratory of Dr. Arlan Richardson at the Oklahoma University Health Sciences Center at ~19 months of age and adult (4-6 months) C57BL/6 mice were obtained from Charles River Laboratories and served as young adult controls. All mice were housed under specific pathogen-free conditions with ad-libitum access to food and water in the

University of Michigan Unit for Laboratory Animal Medicine. p16-3MR mice have been previously characterized and validated [108]. These transgenic mice contain a truncated herpes simplex virus 1 (HSV-1) thymidine kinase (HSV-TK) that is driven by the $p16^{INK4a}$ promoter. This design allows for selective ablation of p16 expressing cells upon exposure to the guanosine analog antiviral, ganciclovir (GCV). GCV interacts with HSV-TK and leads to conversion of GCV into a toxic DNA chain terminator resulting in death of non-dividing senescent cells via mitochondrial DNA damage and caspase-dependent apoptosis [108,109]. To determine the effects of late-life removal of p16-expressing senescent cells on skeletal muscle function, starting at 20 months of age, p16-3MR mice were treated with GCV (25 mg/kg) for five consecutive days during each of the first two weeks of the study and then an additional 5 days once per month until the mice reached 25-months of age (**Figure 2.1A**). Control p16-3MR mice (GCV^-) were injected with an equal volume of saline (**Figure 2.1A**). At 26 months of age, 4 weeks after last treatment, muscle force generation was measured as described below and hind limb muscles and blood were collected and processed for analysis.

2.3.2 In vivo and in situ force testing

Mice were anesthetized with initial intraperitoneal injections of Avertin (tribromoethanol, 250 mg/kg) with supplemental injections to maintain an adequate level of anesthesia during all procedures. For in vitro contractile properties, soleus, and extensor digitorum longus (EDL) muscles were carefully removed from the animal and placed in a horizontal bath containing buffered mammalian Ringer solution (in mM: 137 NaCl, 24 NaHCO3, 11 glucose, 5 KCl, 2 CaCl2, 1 MgSO4, 1 NaH2PO4, and 0.025 turbocurarine chloride) maintained at 25°C and bubbled with 95% O2-5% CO2 to stabilize pH at 7.4. One tendon was tied to a force transducer (model BG-50, Kulite Semiconductor Products, Leonia, NJ) and the other tendon to a servomotor (model 305B,

Aurora Scientific, Aurora, ON). Muscles were stimulated by square pulses delivered by two platinum electrodes connected to a high-power biphasic current stimulator (model 701B, Aurora Scientific). Custom-designed software (LabVIEW 2018, National Instruments, Austin, TX) controlled electrical pulse properties and servomotor activity and recorded data from the force transducer. The voltage of pulses was increased, and optimal muscle length (L_o) was subsequently adjusted to give maximum twitch force [110]. The L_o was measured with digital calipers. Muscles were held at L_o and subjected to trains of pulses to generate isometric contractions. Pulse trains were 300 ms for EDL muscles and 900 ms for soleus muscles. Stimulus frequency was increased until the maximum isometric force (P_o) was achieved [110]. Previously established L_f-to-L_o ratios of 0.44 for EDL muscles and 0.71 for soleus muscles [110] were used to calculate L_f for each muscle. The physiological cross-sectional area (CSA) of muscles was determined by dividing the mass of the muscle by the product of L_f and 1.06 g/cm^3, the density of mammalian skeletal muscle. P_o was normalized by the CSA to calculate specific P_o (sP_o), as a measure of intrinsic force generating capacity.

Gastrocnemius (GTN) muscle contractile properties were measured in situ, as described by Larkin et al. (2011). In anesthetized mice, the whole GTN muscle was isolated from surrounding muscle and connective tissue using great care not to damage the nerve and/or blood vessels during the dissection. A 4-0 silk suture was tied around the distal tendon and the tendon was severed. The animal was then placed on a temperature-controlled platform warmed to maintain body temperature at 37°C. The hindlimb was securely tied to a fixed post with 4-0 monofilament nylon suture at the knee and the foot was clamped to the platform. The distal tendon of the GTN muscle was then tied to the lever arm of a servomotor (model 6650LR, Cambridge Technology). A continual drip of saline warmed to 37°C was administered to the GTN muscle to maintain its

temperature. The muscle was activated by stimulation of the tibial nerve using a bipolar platinum wire electrode. Similar to the *in vivo* force testing protocol used for the EDL and TA, the optimal voltage and L_o was determined based on the maximal twitch force. The same procedure was then repeated, but rather than activating the muscle via the tibial nerve, a cuff electrode was placed around the proximal and distal ends of the muscle for direct muscle stimulation. After force measurements, the GTN was removed trimmed of tendons, blotted and weighed. GTN muscle fiber length (L_f) was calculated by multiplying L_o by 0.45. CSA and sPo were calculated as described above.

EDL, soleus, and GTN muscles were also removed, trimmed, and weighed and all muscles were either snap-frozen for molecular analyses or coated in tissue-freezing medium (Electron Microscopy Sciences) and rapidly frozen in isopentane cooled with liquid nitrogen for histologic analysis.

2.3.3 Immunofluorescent imaging and analysis

Cross-sections (10 μm) were cut from the muscle mid-belly in a cryostat at −20°C and adhered to SuperFrost Plus slides. Prepared slides for immune cell staining were blocked and permeabilized in blocking buffer (5% normal goat serum and 0.2% Triton X-100 in PBS) for 30 minutes at room temperature followed by overnight incubation at 4°C with primary antibodies. The following day, slides were incubated with Alexa Fluor conjugated secondary antibodies DAPI and mounted using Fluorescence Mounting Medium (Agilent Dako, S302380). A subset of slides was incubated with Alexa Fluor conjugated wheat germ agglutinin (Invitrogen, W32466). Slides prepared for satellite cell staining were lightly fixed with 2% PFA for 5 minutes and rinsed with 0.1% Triton X-100 in PBS (PBST), then blocked with 10% AffinePure Fab Fragment Goat Anti-Mouse IgG (Jackson ImmunoResearch), 2% bovine serum, and 5% normal goat serum overnight in 4°C. Primary anti-

Pax7 (1:10) antibodies were applied to slides for 30 minutes at room temperature, followed by incubation with Alexa Fluor conjugated secondary antibody and DAPI (1 μg/mL) for 30 minutes at room temperature. The following primary antibodies (Abs) were used: rat anti-CD68 (Bio-Rad MCA1957), rabbit anti-Laminin (Abcam #7463), and mouse anti-Pax7 (DHSB #Pax7). Fluorescent images were captured using a Nikon A1 confocal microscope. Muscle morphology was analyzed on stitched panoramic images of the entire muscle cross-section by high-throughput fully automated image analysis with the MuscleJ plugin for FIJI/ImageJ [111]. Immune cells and satellite cells were manually counted throughout the entire cross-section and then normalized to tissue area and fiber number as determined by MuscleJ. In all cases, the experimenter was masked to the experimental group.

2.3.4 Reverse transcription quantitative PCR

Frozen muscles were homogenized in Trizol (Thermo Fisher Scientific, Waltham, MA, USA). RNA was extracted and isolated with chloroform separatory extraction and isopropyl alcohol precipitation. The RNA samples were then treated with DNase (Invitrogen). Total RNA was reverse transcribed with SuperScript Reverse Transcriptase III using random hexamers to prime the extension (Thermo Fisher Scientific) to produce cDNA, which was then used for quantitative PCR (RT-qPCR) using SYBR Green qPCR Master Mix (Bio-Rad Laboratories, Hercules, CA, USA), according to the manufacturer's protocol. Whole muscle gene expression was measured by RT-qPCR on a CFX96 Real-Time PCR Detection System (Bio-Rad, 1855195) in 20 μL reactions of iTaq™ Universal SYBR® Green Supermix (Bio-Rad, #1725124) with 1 μM forward and reverse primers (Table 1) or with TaqMan® probes. Relative mRNA expression was determined using the $2^{-\Delta\Delta Ct}$ method. The following primers/probes were used:

Table 2.1: List of primers used in this study

Primers		
Gene		Sequence (5'-3')
TNF-α	Forward	ATGGCCTCCCTCTCATCAGT
	Reverse	TGGTTTGCTACGACGTGGG
IL-6	Forward	TCCGGAGAGGAGACTTCACA
	Reverse	TTGCCATTGCACAACTCTTTTCT
AChRα	Forward	GCCATTAACCCGGAAAGTGAC
	Reverse	CCCCGCTCTCCATGAAGTT
MuSK	Forward	ACCGTCATCATCTCCATCGTGT
	Reverse	CTCAATGTTATTCCTCGGATACTCC
18s	Forward	GCTTGCTCGCGCTTCCTTACCT
	Reverse	TCACTGTACCGGCCGTGCGTA
Probes		
Gene		Assay ID
p16(INK4a)		Mm00494449_m1 (Thermo Fisher Scientific)

2.3.5 Plasma protein analysis

Blood samples from p16-3MR mice were collected from the descending aorta while mice were under anesthesia (isoflurane). Blood samples were collected into EDTA coated microcentrifuge tubes and centrifuged at 10,000 g for 10 mins at 4°C and plasma samples were

collected. Multiplex analysis for cytokines, chemokines and other factors was performed using the Luminex Bio-Plex Pro Mouse Cytokine 23-plex Assay (#M60009RDPD

2.3.6 Statistical analyses and data presentation

Data are presented as the mean ± SEM. Statistical analysis was performed in GraphPad Prism 9. Between-group differences were tested by two-tailed unpaired students t-tests (2 groups) or by one-way ANOVA (more than 2 groups). $p \leq 0.05$ was used to determine statistical significance.

2.4 Results

2.4.1 Reduced p16 expression in skeletal muscle in GCV treated p16-3MR mice

To verify successful depletion of p16-expressing cells, quantitative-PCR (qPCR) was performed in skeletal muscle (gastrocnemius muscles). A roughly 50% reduction of p16 expression was found in skeletal muscles of GCV treated mice (GCV^+) compared to saline treated controls (GCV) (**Figure 2.1**). These data show that removal of muscle-resident p16-expressing cells can be achieved with the p16-3MR model.

2.4.2 Muscle mass and force is greater in select hind limb muscles after removal of p16-expressing cells

Figure 2.1: GCV$^+$ muscle showed reduced expression of *p16^{INK4A}*. (A) p16-3MR mice were given ganciclovir (GCV$^+$) or vehicle (GCV$^-$) via intraperitoneal (IP) injection at 20-months of age for 10 days over two weeks. Additional 5-day treatments were administered over one week in five subsequent months until sacrifice after six months. Tissue was harvested at 26-months of age. **(B)** p16 mRNA relative to 18s mRNA was reduced nearly ~50% in gastrocnemius muscles of GCV$^+$ mice compared to saline treated controls (GCV$^-$). Bars show the mean ± SEM of 3–5 mice per group with dots representing data from each individual mouse. Blue and red data points represent male and female mice, respectively. ** Denotes p <0.001 between groups for each tissue by one-way ANOVA with Tukey post hoc test.

Body mass did not differ between GCV$^+$ and GCV$^-$ mice regardless of sex (Supplemental Materials (**Figure 2.2**), therefore, muscle masses are expressed in absolute terms, rather than normalized by body mass. Extensor digitorum longus (EDL), tibialis anterior (TA), gastrocnemius (GTN), and quadriceps (Quads) muscle masses were 12%, 19%, 11%, and 16% greater, respectively, in male GCV$^+$ mice compared to vehicle controls (**Figure 2.3**), whereas plantaris and soleus muscle masses were not different between GCV$^+$ and GCV$^-$ mice. Despite the modestly higher muscle masses found in GCV$^+$ compared with GCV$^-$mice, the effect on muscle mass was observed in the majority of the hind limb muscles examined, suggesting a broad effect to preserve muscle mass. In addition, the similarity in the degree of muscle mass preservation between muscles after late-life removal of p16 suggests that the effect is not specific to a particular muscle fiber composition. Despite broad effects in male mice, female GCV$^+$ and GCV$^-$ mice displayed no differences in mass for any of the muscles studied (**Figure 2.4**).

Figure 2.2: Body masses of male and female mice. Body mass did not differ between GCV$^+$ and GCV$^-$ mice. Bars show the mean ± SEM of 4-16 mice per group with dots representing data from each individual mouse. NS denotes *p*-value > 0.05 between groups by two-tailed unpaired *t*-test.

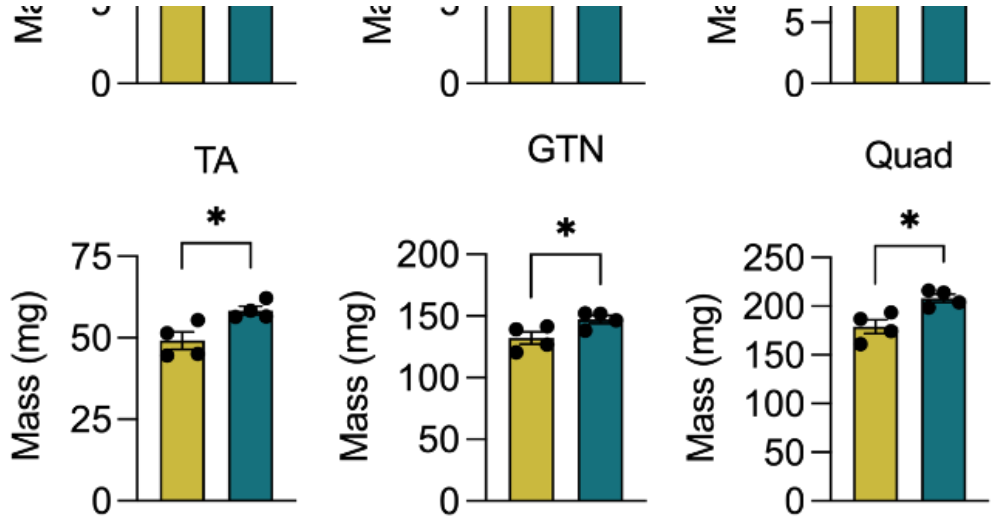

Figure 2.3: Hind limb muscle masses were preserved in male GCV$^+$ mice. Masses are shown for extensor digitorum longus (EDL), tibialis anterior (TA), gastrocnemius (GTN) and quadriceps (Quad) muscles in milligrams for male ganciclovir treated (GCV$^+$) and vehicle treated (GCV$^-$) mice. Bars show the mean ± SEM of four mice per group with dots representing data from each individual male mouse. *Denotes $p < 0.05$ between groups by two-tailed unpaired *t*-test.

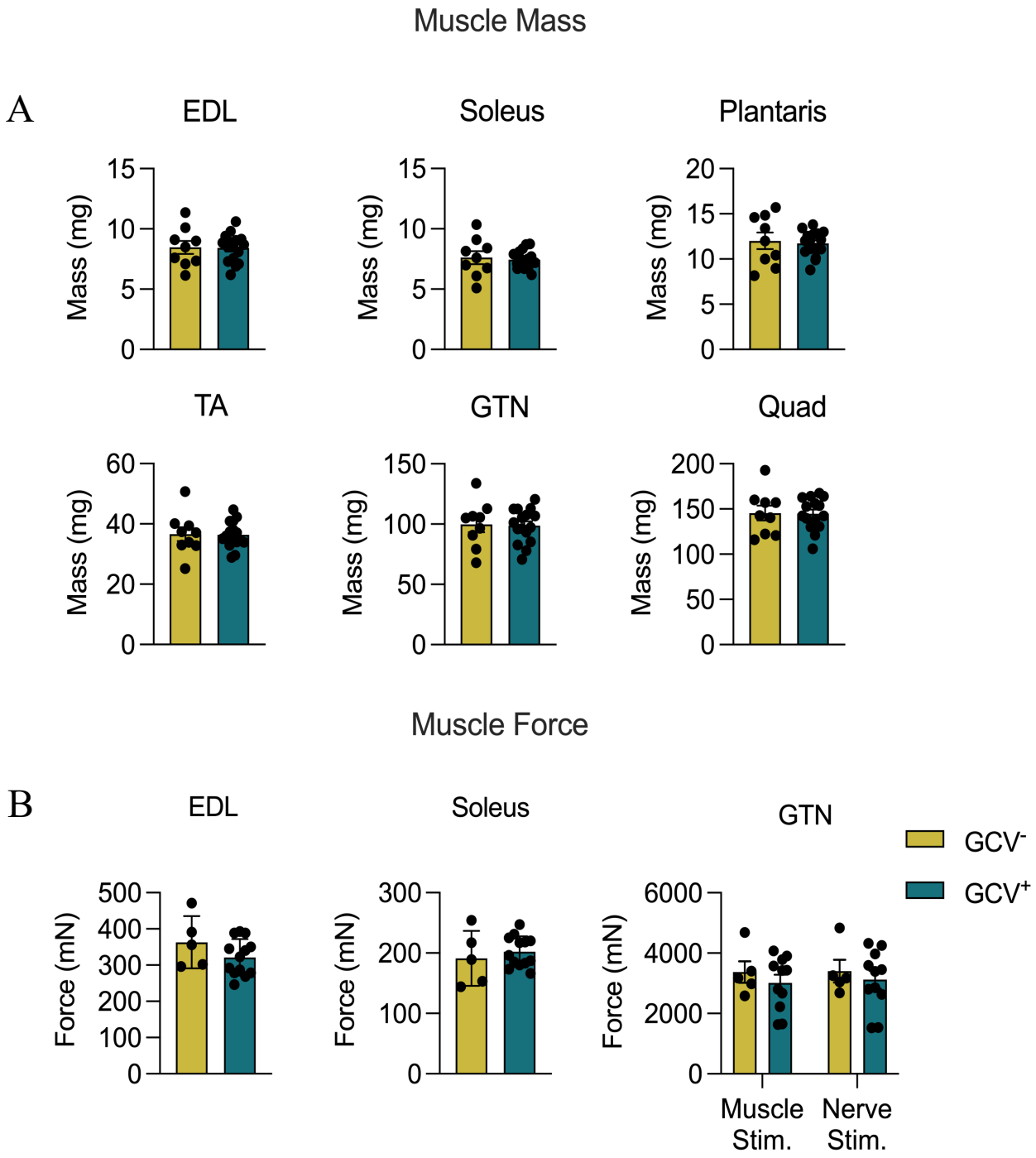

Figure 2.4: Absolute muscle mass and force did not differ between female GCV^+ and GCV^- mice. (A) Extensor digitorum longus (EDL), soleus, plantaris, tibialis anterior (TA), gastrocnemius (GTN) and quadriceps (Quad) muscle masses were not significantly different between GCV^+ and GCV^- mice. (B) Similarly, EDL, soleus, and GTN absolute muscle forces were not significantly different. Bars show the mean ± SEM of 5-16 mice per group with dots representing data from each individual mouse.

To determine the effects of $p16^+$ cell depletion on muscle function we performed both *in vitro* and *in situ* muscle force testing. GCV treatment resulted in 13% and 10% greater maximum isometric tetanic force (P_o) for GTN muscles with direct muscle stimulation and nerve simulation, respectively (**Figure 2.4**). These data are consistent with the higher GTN muscle mass for GCV^+ mice and indicate that the increase in force generating capacity was attributable to an increase in functional muscle mass. Furthermore, specific forces (specific P_o, sP_o) did not differ between GCV^+ and GCV^- mice (**Figure 2.6**) indicating no effect of the removal of p16 expressing cells on the intrinsic force generating capacity of the muscle. We also found no alterations in the expression of acetylcholine receptor subunit alpha (AChRα) or muscle-specific kinase (MuSK), canonical neuromuscular junction related genes, between GTN muscles in GCV^+ and GCV^- mice (**Figure 2.7**). P_o was not different between GCV^+ and GCV^- groups for EDL or soleus muscles from male mice or for any muscles of female mice.

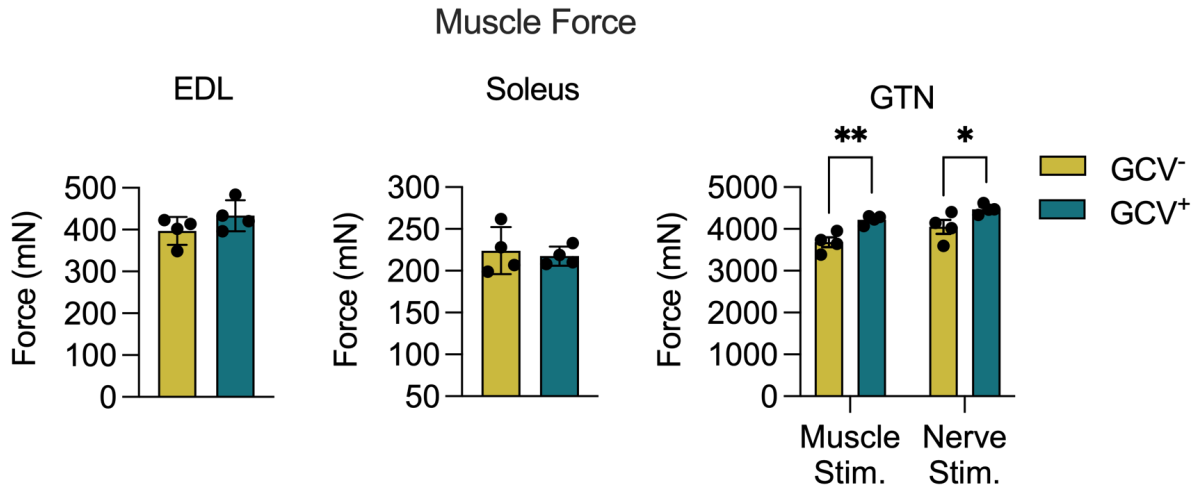

Figure 2.5: Gastrocnemius (GTN) muscles from male ganciclovir treated (GCV^-) mice generated higher forces than muscles from vehicle treated (GCV^-) mice. Data are shown for maximum isometric tetanic force (P_o) generated by extensor digitorum longus (EDL), soleus and GTN muscles expressed in millinewtons (mN). EDL and soleus muscles were evaluated *in vitro*, while GTN muscles were evaluated *in situ* using both direct muscle stimulation and nerve stimulation. Bars show the mean ± SEM of four mice per group with dots representing data from each individual male mouse. *Denotes $p < 0.05$ and ** denotes $p < 0.01$ between groups by two-tailed unpaired *t*-test.

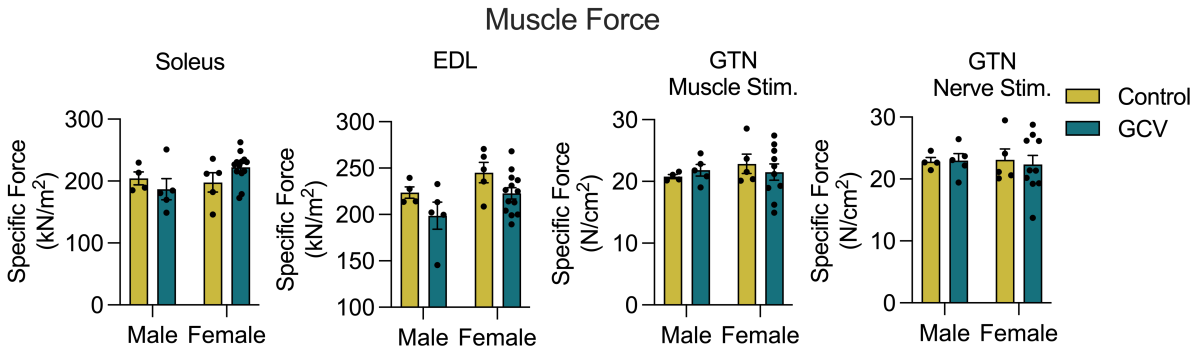

Figure 2.6: Specific forces did not differ between GCV^{+} and GCV^{-} mice, regardless of sex. Soleus, EDL, and GTN specific muscle forces were not significantly different. Bars show the mean ± SEM of 5-16 mice per group with dots representing data from each individual mouse.

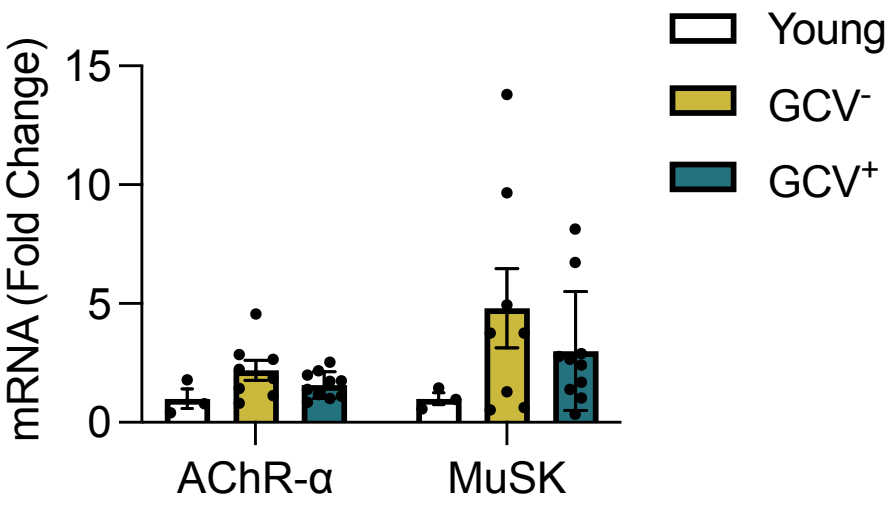

Figure 2.7: AChRα and MuSK mRNA expression in gastrocnemius muscles were not significantly different in young, GCV-, and GCV+ mice. Bars show the mean ± SEM of 3-8 mice per group with dots representing data from each individual mouse.

2.4.3 CD68^{+} positive cell numbers are reduced in EDL muscles of GCV^{+} mice

Since the presence of senescent cells is thought to contribute to a pro-inflammatory environment, we assessed the total number of macrophages (CD68^{+} cells) in muscles of GCV^{+} and GCV^{-} mice. Compared with control GCV^{-} mice, EDL muscles of GCV^{+} mice showed a reduced number of intramuscular CD68^{+} cells. The magnitude of the difference was ~25%, whether the number of cells were expressed relative to the cross-sectional area of the section or relative to the number of muscle fibers in the section (**Figure 2.8A,B**). We cannot establish from these experiments if the CD68^{+} cell depletion was due to genetic ablation of CD68^{+}/p16^{+} cells following GCV treatment or due to a reduction in the inflammatory state of the tissue secondary to the loss of other senescent cell populations. Nevertheless, these data suggests that depletion of p16^{+} reduces intramuscular macrophage number in these aged mice and as such likely also impacted upon immune responses and function.

2.4.4 Pax7^{+} cell content is not impacted by removal of p16-expressing cells

With growing evidence of increased cellular senescence markers in post-mitotic fibers [112,113] and increased expression of *p16^{INK4A}* in resting geriatric and progeric muscle stem cells [106], we chose to analyze the numbers of Pax7^{+} muscle stem cells (MuSC, satellite cells), which are critical regulators of the health and repair of skeletal muscle [114,115]. We evaluated Pax7^{+} cells in cross sections of soleus muscles based on the higher prevalence of satellite cells associated with slow compared to fast muscle fibers with age [116,117]. In contrast to the reduction in CD68^{+} macrophages following depletion of p16^{+} cells, the numbers of Pax7^{+} cells were not different between GCV^{+} and GCV^{-} mice whether expressed relative cross-sectional area or relative to the number of muscle fibers (**Figure 2.8C,D**).

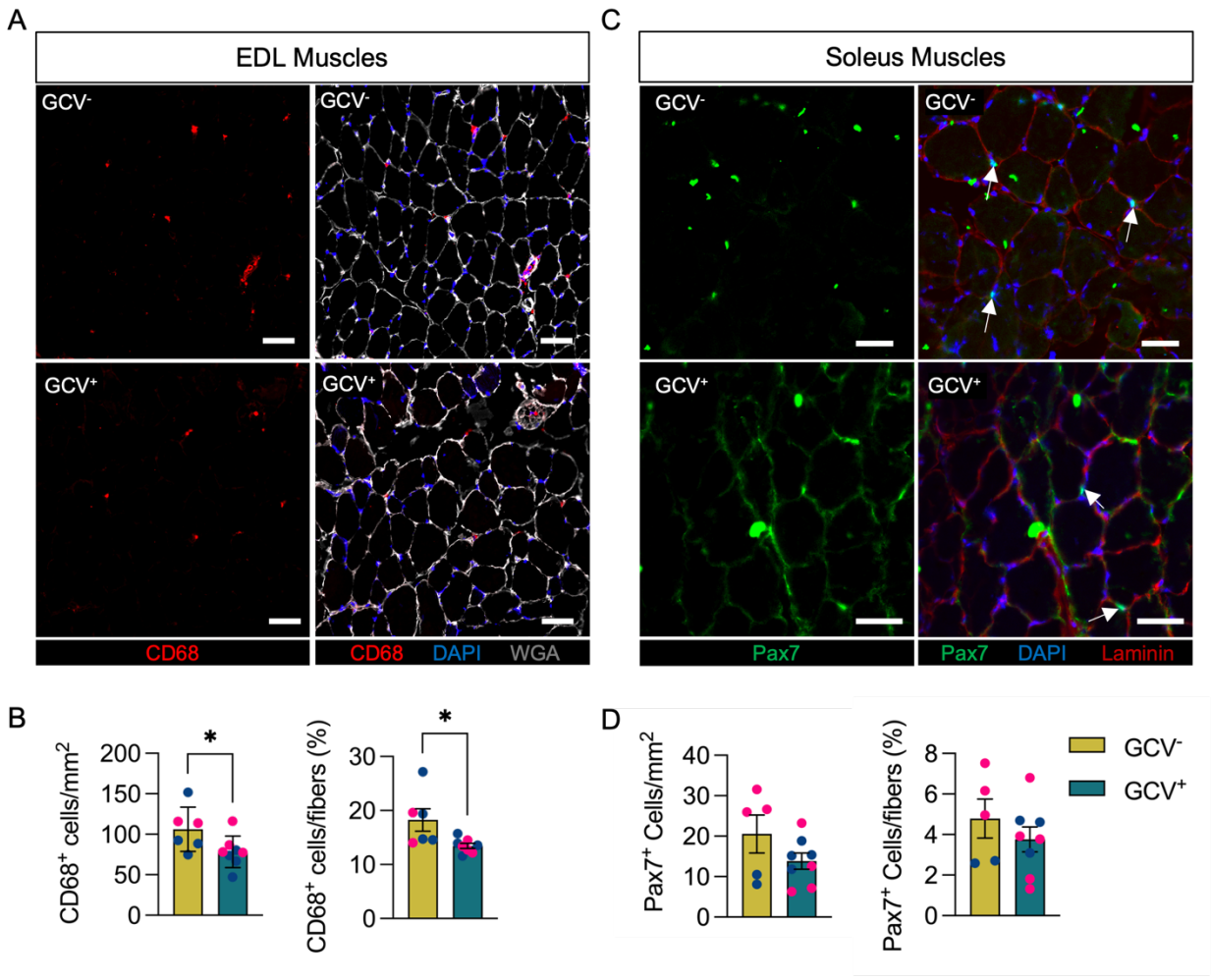

Figure 2.8: CD68-positive but not Pax7-positive cells were reduced in GCV$^+$ mice. (A) Representative images are shown for cross sections of extensor digitorum longus (EDL) muscles stained with an antibody to the macrophage marker CD68 (red) as well as wheat germ agglutinin (WGA, white) and DAPI (blue). **(B)** Data showing counts of intramuscular CD68-positive cells are shown for cross sections from ganciclovir (GCV$^+$) and vehicle treated (GCV$^-$) mice. **(C)** Representative images are shown for cross sections of soleus muscles stained with an antibody to the satellite cell marker Pax7 (green) as well as laminin (red) and DAPI (blue). White arrows indicate Pax7-positive cells that overlap with DAPI and are between sarcolemma and basal lamina of muscle fibers. **(D)** Data showing counts of intramuscular Pax7-positive cells are shown for cross sections from ganciclovir (GCV$^+$) and vehicle treated (GCV$^-$) mice. For both DC68 and Pax7, cell counts are expressed either relative the area analyzed (mm^2) or by the number of muscle fibers in the sections (%). Bars show the mean ± SEM of 5-8 mice per group with dots representing data from each individual mouse. Blue and red data points represent male and female mice, respectively. *Denotes $p < 0.05$ between groups by two-tailed unpaired *t*-test. Scale bar = 50 µm.

2.4.5 Plasma inflammatory factors and muscle cytokine expression are minimally impacted by p16-positive cell depletion

Since GCV treatment in p16-3MR mice results in whole-body depletion of $p16^{+}$ cells in tissues that are accessible to GCV treatment, we assessed plasma profiles for a wide array of inflammatory mediators and mRNA levels for select cytokines from skeletal muscle isolates. Out of a panel of 22 inflammatory mediators assessed in plasma, only granulocyte colony-stimulating factor (G-CSF), to be lower in GCV^{+} mice compared to GCV^{-} controls (**Figure 2.9A**). Furthermore, mRNA expression of tumor-necrosis factor alpha (TNF-α) and interleukin-6 (IL-6) mRNA, were not modified in GTN muscles of GCV^{+} mice (**Figure 2.9B**). These data suggest that alterations in inflammatory gene and protein expression are not largely affected after a late-life 5-month long $p16^{+}$ cell depletion regimen.

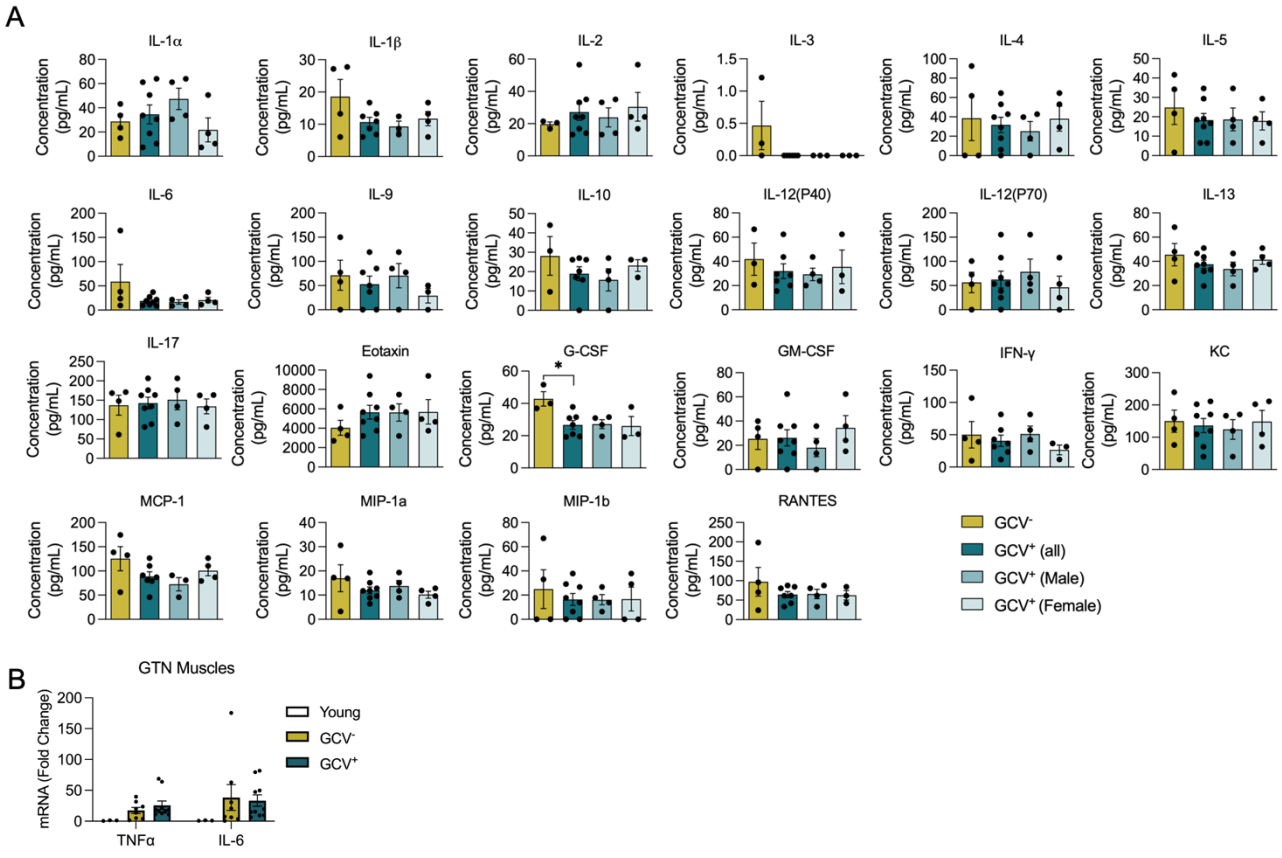

Figure 2.9: Plasma inflammatory factors and skeletal muscle cytokine mRNA expression were largely unaffected with p16-positive cell deletion. (A) Plasma protein levels (pg/mL) for 22 inflammatory mediators are shown for saline treated controls (GCV^-), combined male and female GCV treated mice, GCV^+ (all), male GCV treated mice, GCV^+ (Male), and female GCV treated mice, GCV^+(Female). **(B)** TNFα and IL-6 mRNA expression relative to 18s mRNA in gastrocnemius (GTN) muscles were not significantly different in young, GCV^-, and GCV^+ mice. Bars show the mean ± SEM of 3-8 mice per group with dots representing data from each individual mouse. *Denotes $p < 0.05$ between groups by one-way ANOVA.

2.5 Discussion

Herein we report the effects of late-life removal of $p16^+$ cells on skeletal muscle function. Our study shows that modest muscle mass and muscle force preservation can be achieved with genetic ablation of $p16^+$ cells in male mice. The degree of muscle mass (+11%) that was preserved in the GTN muscles with GCV treatment closely reflected the degree of increased force generation (+11.5%). These findings suggest that the mass preservation achieved through elimination of $p16^+$ expressing cells was in fact preservation of contractile tissue with no change in inherent contractility, a conclusion supported by no effect of GCV treatment on specific force (force/CSA). Since GCV treatment results in whole-body removal of $p16^+$ cells, the preservation in mass is likely a result of systemic influences on the skeletal muscle tissue rather than caused by direct changes to skeletal muscle fibers. TA, EDL, and quadriceps muscles also showed preservation of mass in GCV^+ mice. We did not assess force generating capacity in TA or quadriceps muscles, and although differences in EDL muscles did not reach statistical significance, the trend was for an increase in treated mice when compared with saline treated controls did not reach statistical significance. Despite the similarity in force generation, increased muscle mass provides additional benefits as skeletal muscle serves other functional roles such as acting as a protein repository and as a site for glycolipid metabolism. Therefore, the preservation of muscle mass could provide other metabolic health benefits.

The current study utilized a treatment regimen that spanned many months, and muscles were evaluated at the most advance stages of life. It is possible that benefits in muscle function through deletion of $p16^{+}$ cells were achieved earlier during the treatment protocol. However, direct rigorous assessments of isolated muscle function are terminal procedures and as such we were unable to longitudinally assess the effects of GCV treatment on muscle function. Our findings of some evidence of preservation of muscle masses and strength were consistent with the report by Xu et al. (2018) of greater maximal walking speed, hanging endurance, grip strength, treadmill endurance and daily activity in mice as a result of late-life treatment with a senolytic cocktail of dasatinib plus quercetin. Since senolytics work through disabling senescent anti-apoptotic pathways (SCAP), a distinct mechanism of action compared to genetic ablation, our method only specifically removes $p16^{INK4A}$ expressing cells and does not directly affect other senescent promoting pathways such as $p53/p21^{WAF1/CIP1}$ [118]. Nevertheless, our data show that directly attenuating the $p16^{INK4A}$ pathway also results in modest skeletal muscle benefits in male mice.

An interesting finding in our study was the sexual dimorphism observed for our muscle assessments. The significant protective effect observed for muscle mass in male mice by the elimination of $p16^{+}$ cells was not seen for GCV^{+} female mice. A recent study in mice showed that male mice, at 20-months of age, showed higher expression of both p16 and p21 mRNA in various tissues compared to female mice [119]. However, at 30-months of age the numbers of senescent cells were equivalent between both sexes. Considering our treatment regimen began at 20-months of age, differences in the level of p16 expressing cells in male compared with female p16-3MR mice at this time-point may potentially explain the greater benefit of the deletion of $p16^{+}$ cells observed for male mice. Although sarcopenia is equally prevalent in both men and women, the rate of muscle mass and strength decline has also been reported to be faster in men [120]. Therefore,

understanding the sex specific mechanisms that drive sarcopenia are important for advancing therapeutics that promote muscle health benefits.

Tissue resident macrophages are critical for skeletal muscle regeneration after injury and muscle regeneration after injury requires inflammatory signals for proper repair [121,122]. Furthermore, other studies have found that removal of senescent cells at injury sites has a negative impact on tissue regeneration [123,124]. Therefore, whether the observation in the present study of a reduction in intramuscular $CD68^+$ macrophages with $p16^+$ cell ablation provides a functional benefit to muscle tissue remains unclear. Specifically, the effect of the reduction in $CD68^+$ cells and perhaps other p16-expressing cells on the ability to respond to insults such as nerve or muscle injuries remains to be established. However, macrophage number has been shown to increase with age and produce low grade inflammation that contributes to muscle mass and functional decline[125]. Therefore, our finding of reduced macrophage number with GCV^+ may provide a beneficial response in basal conditions. Moreover, another recent study showed that absence of fibro-adipogenic progenitor (FAP) senescence after exercise leads to muscle degeneration with FAP accumulation[126]. Building upon these findings, a more recent study utilized single-cell RNA sequencing (scRNA-Seq) to investigate into the cellular landscape of old skeletal muscles in female mice. This study demonstrated that FAPs from aged muscles upregulated senescence-associated genes, notably p16 and p21.[105]. By using a cocktail of senolytic drugs, they were able to demonstrate functional benefits in the skeletal muscles of older mice, which included increased grip strength and a notable reduction in the expression of p53 signaling pathways, encompassing genes such as Gadd45a, Runx1, and Ankrd1, in comparison to controls treated with a vehicle. However, it is interesting to note that despite these functional improvements, there was no

evidence of preserved cross-sectional area (CSA) or overall muscle mass in mice treated with the senolytic cocktail (DQ) when compared to the vehicle control group.

One benefit to removing cellular senescence is improvement of muscle stem cell function. At baseline, muscle stem cells from geriatric and progeric models have been shown to display an upregulation of senescence-associated genes including *p16*^{INK4A} and a reduced regenerative capacity upon muscle injury [106]. Repression of *p16*^{INK4A} through shRNA restores quiescence and regeneration in aged mice. Our study showed no overall change in the number of Pax7^{+} muscle stems cells in GCV^{+} mice; however, we did not confirm whether the muscle stem cells also co-expressed *p16*^{INK4A} or if there was an effect of clearing p16^{+} cells on regenerative capacity. Future studies should investigate the critical senescent cell types that provide the greatest therapeutic efficacy when removed or modified.

The SASP phenotype is one of the most extensively studied features of cellular senescence [127]. Our group sought out to understand whether removal of p16^{+} cells through a 5-month long treatment program would reduce systemic cytokine expression. We therefore assessed plasma chemokine inflammatory profiles using a 22-factor array. Our experiments showed no difference in overall inflammatory profiles between saline treated controls (GCV^{-}) and GCV^{+} mice (both male and female). Although somewhat surprising, these data are consistent with findings from two independent studies that found no change in serum/plasma cytokine levels with p16^{+} cell ablation and treatment with senolytics [128,129]. Similarly, we found no differences in expression of TNFα or IL-6 mRNA between GCV^{+} and GCV^{-} GTN muscles. These data conflict with Baker et al. (2016), who found significantly reduced levels in both TNFα and IL-6 mRNA in GTN muscles of mice with removal of p16^{+} cells. However, their study used a different model of p16^{+} cell ablation and evaluated mice at a much younger age, with treatments to remove p16^{+} cells beginning at 12

months of age and evaluations performed at 18 months. Our approach in the current study of deleting $p16^{+}$ cells starting at 20-months of age and evaluating mice at the significantly more advanced ages of greater than 26 months may explain the difference between the present findings and those of Baker et al. Further investigation is required to understand the efficacy window for clearing $p16^{+}$ cells to promote muscular function.

Overall, our data show that elimination of $p16^{INK4A}$ expressing cells can provide modest late-life functional improvements and muscle mass preservation. These changes, however, are sex-specific and therefore warrant further examination into the molecular processes that induce muscle health benefits in both male and female. Future studies are needed to determine molecular targets and treatment windows to combat overall skeletal muscle aging.

Chapter 3 Elevated ROS Induces Schwann Cell Derived Signaling to Enhance AChR Clustering in C2C12 Myotubes

3.1 Abstract

Reactive oxygen species (ROS) play dual roles in cellular physiology, ranging from maintaining homeostasis to causing oxidative stress and cellular damage. Particularly in the peripheral nervous system, Schwann cells are pivotal for axonal signal propagation and nerve repair, with their functionality being influenced by ROS dynamics. Despite known roles of ROS in Schwann cell activation, the direct impact on their secretome and subsequent synaptic support remains underexplored. This study investigates the response of Schwann cells to oxidative stress and its subsequent impact on acetylcholine receptor (AChR) clustering, crucial for effective neuromuscular junction (NMJ) functionality. We employed in vitro experiments using primary rat Schwann cell cultures exposed to paraquat (PQ) to induce ROS generation. We evaluated the cytotoxic effects, ROS induction, and changes in trophic gene expression under oxidative stress. Further, we examined the influence of conditioned media from activated Schwann cells on AChR cluster formation in differentiated C2C12 myotubes. PQ treatment led to dose-dependent cytotoxicity and ROS generation in Schwann cells. Sublethal oxidative stress conditions induced the upregulation of repair genes, such as Gdnf and Ngfr, along with markers indicative of Schwann cell repair mechanisms. Conditioned media from PQ-activated Schwann cells significantly enhanced AChR cluster formation in C2C12 myotubes compared to untreated controls. Notably, brief exposure to Agrin followed by treatment with activated Schwann cell media was as effective as prolonged Agrin exposure in inducing AChR clustering. Our findings demonstrate that Schwann

cells respond to oxidative stress by upregulating genes associated with nerve repair and by secreting factors that potentiate AChR clustering in muscle cells. This suggests that modulating ROS levels can enhance Schwann cell-mediated synaptic support at the NMJ. The results highlight the therapeutic potential of targeting Schwann cell responses to oxidative stress in aging and neuromuscular disorders.

3.2 Introduction

Reactive oxygen species (ROS) are highly reactive molecules containing oxygen, emerging as natural byproducts of oxygen metabolism and playing critical roles in cellular signaling and maintaining physiological homeostasis[130]. While essential for homeostasis and defense, excessive ROS — generated during environmental stress or cellular dysfunction — can cause considerable damage, known as oxidative stress, impacting cell structures and functions[131]. This imbalance is implicated in various diseases and is a central theme in the free radical theory of aging[132]. The free radical theory suggests that ROS accumulation inflicts progressive damage to vital macromolecules, precipitating cellular senescence and tissue degeneration. The relationship between ROS and cellular stress responses spans a spectrum. At one end is 'eustress,' which derives from the Greek "eu-" meaning 'good,' and signifies the positive impact of ROS in moderate levels[130]. This beneficial stress is instrumental in pathogen defense[133], intracellular communication[134], and activating protective genetic pathways[135]. On the opposite end, excessive ROS can overwhelm cellular antioxidant systems, causing oxidative stress with broad cellular consequences, including the promotion of age-related pathologies[136,137].

Glial cells, encompassing astrocytes, oligodendrocytes, microglia, and Schwann cells, are essential for neuronal support, contributing to the health and function of the nervous system.

Schwann cells, specific to the peripheral nervous system, are critical not only for facilitating axonal propagation of neural signals, but also for guiding axon regrowth during nerve repair[69,81] and maintaining neuromuscular junctions (NMJs)[40,42,138]. After nerve injury, Schwann cells are stimulated by a variety of cellular cues, including an abrupt increase in ROS[139], to initiate a reparative response[69,81], enhancing their proliferation[140], migratory capacity[141], and ability to support axon guidance[69,81]. The elevated levels of ROS at injury sites[71] and potentially from denervated muscle[136], can initiate complex intracellular signaling within Schwann cells, triggering transcription factors like NF-κB, Nrf2, and c-Jun, which in turn regulate genes essential for tissue repair and regeneration[139,142,143].

Exogenous ROS, such as hydrogen peroxide, have been used experimentally to trigger the MAPK/ERK signaling pathway in Schwann cells, pushing them towards a progenitor-like state capable of reprogramming in response to injury[71]. Activation of pathways including ERK1/2 and p38 MAPK has been associated with demyelination and cellular reprogramming necessary for regeneration[78,79]. Following nerve injury, Schwann cells not only participate in myelin clearance but also in the secretion of a suite of factors that support regeneration including neurotrophins, cytokines, and extracellular matrix (ECM) components that aid the recruitment of immune cells, axonal guidance, and the restoration of synaptic structure and function at the NMJ[144,145]. For example, Schwann cell-secreted factors such as GDNF and BDNF have been shown to specifically promote AChR clustering[146] and muscle fiber reinnervation[51], which is a determinant for effective synaptic transmission at the NMJ. While ROS has been identified as a stimulant for Schwann cell de-differentiation akin to nerve injury, the potential for altered redox states to directly influence the Schwann cell secretome, with implications for synaptic support, is yet to be fully explored.

The study described in this chapter employs in vitro experimentation to investigate the response of Schwann cells to oxidative stress and the impact of the resultant secretory behavior on AChR clustering. We hypothesized that Schwann cells activate trophic support pathways in response to treatment with ROS inducing agents and that the secreted factors promote AChR clustering in differentiated C2C12 myotubes. This research underscores the importance of precise ROS modulation in Schwann cell functionality and points to the therapeutic potential of harnessing this response in aging and neuromuscular disorders.

3.3 Materials and Methods

3.3.1 Schwann cell and C2C12 myotube cultures

Cultures of adult rat Schwann cells

The experimental procedures were ethically reviewed and received approval by the Institutional Animal Care and Use Committee at the University of Michigan, ensuring adherence to the institution's policies as well as USDA and NIH standards for vertebrate animal research. Sciatic nerves were harvested from 3-month-old female rats (what strain). These were immediately excised under sterile conditions, preserved in chilled Leibovitz's L-15 Medium supplemented with 1% Penicillin-Streptomycin-Amphotericin B.

Under a dissecting microscope, each sciatic nerve was meticulously cleared of non-nerve tissue and the outer epineurium was carefully detached. The nerves and epineurium were then separately maintained in fresh L-15 medium. Nerve fascicles were delicately separated to single fibers using specialized forceps, with routine transfer to new L-15 medium to ensure tissue integrity. For cell extraction, the nerve fibers and epineurium were digested enzymatically in a solution containing Dispase II and collagenase in high-glucose (Dulbecco's Modified Eagle

Medium (DMEM), incubated overnight at 37 °C with 5% CO_2. Post-digestion, the cells were isolated by adding fetal bovine serum (FBS) to Hanks′ Balanced Salt Solution (HBSS), followed by centrifugation. The cell pellet was then suspended in DMEM with FBS, filtered through a narrow glass pipet, centrifuged, and re-suspended in DMEM with FBS and antibiotics. Cells were then plated on poly-L-lysine and laminin-prepared plates for expansion. The cultures were incubated overnight at 37 °C in a CO_2 incubator. The dishes were pre-coated with poly-L-lysine and mouse laminin solutions at specified temperatures and durations. The Schwann cell culture medium, composed of DMEM and Ham's F-12 Nutrient Mixture in a 3:1 ratio, was enriched with 2% FBS, penicillin/streptomycin (1%), neuregulin (50 ng/mL), forskolin (2 μM), and N2 supplement (1%). This medium was replaced every two to three days to support Schwann cell growth and minimize fibroblast contamination. Approximately three days post-expansion, the concentration of FBS in the Schwann cell media was increased to 10% to optimize the cell culture conditions.

3.3.2 Assess Schwann cell viability and activation with Paraquat treatment

Paraquat treatment and MTT Assay

To evaluate the response of Schwann cells to oxidative stress via Paraquat (PQ) exposure, we conducted a systematic study employing the 3-(4,5-Dimethylthiazol-2-yl)-2,5-diphenyltetrazolium bromide (MTT) assay for cell viability. Primary Schwann cells were plated at a density of 8,000 cells/well in a 96-well plate pre-coated with poly-L-lysine and laminin. After a day of cell adhesion, the cultures were exposed to varying concentrations of PQ (0, 10, 50, 100, 250, and 500 μM) for 48 hours. After PQ treatment, cells were gently washed with PBS and incubated with MTT (Abcam) in serum-free media at 37°C for 3 hours. Solubilization of the

formazan product was facilitated by MTT solvent, with plates agitated in darkness for 15 minutes prior to quantifying absorbance at 590 nm using a microplate reader (Biotek).

RT-qPCR

For the RT-qPCR analysis, we employed a standardized protocol for RNA extraction and cDNA synthesis. The cells were lysed with Trizol reagent using a cell scraper and the lysate was transferred to microcentrifuge tubes for subsequent RNA isolation via phenol/chloroform extraction. The Qiagen Rneasy Kit was utilized for RNA purification and the concentration of the extracted RNA was measured using a NanoDrop 2000c Spectrophotometer from Thermo Fisher Scientific. To ensure the removal of any contaminating genomic DNA, the RNA samples were treated with Dnase I (Ambion) and the enzyme was subsequently inactivated by heating. We synthesized cDNA from 500 ng of total RNA using the SuperScript III Master Mix with Random Hexamers and dNTPs provided by Invitrogen. Quantitative PCR amplification was performed in a CFX96 Real-Time PCR Detection System from Bio-Rad, using iTaq Universal SYBR Green Supermix in a 20 µL reaction volume that included 1 µM of each primer. The expression levels of the target mRNAs were quantified using the 2-ΔΔCT method, with Gapdh used as a normalization reference. The specific primer sequences used in the study are listed in **Table 2.**

Table 3.1: Primers used for RT-qPCR

Name	Sequence
Agrn (Fwd)	TTCCTCAGCAACTACAAACCTG
Agrn (Rev)	TTCACACACAGCACCAAAGC
Ngfr (Fwd)	TGCCTGGACAGTGTTACGTT
Ngfr (Rev)	ACAGGGAGCGGACATACTCT
Gdnf (Fwd)	CCAGTGACTCCAATATGCCTG
Gdnf (Rev)	CTCTGCGACCTTTCCCTCTG
Gapdh (Fwd)	CACCATCTTCCAGGAGCGAG
Gapdh (Rev)	CCTTCTCCATGGTGGTGAAGAC
Bdnf (Fwd)	TCATACTTCGGTTGCATGAAGG
Bdnf (Rev)	AGACCTCTCGAACCTGCCC
c-Jun (Fwd)	CCTTCTACGACGATGCCCTC
c-Jun (Rev)	GGTTCAAGGTCATGCTCTGTTT
Tnc (Fwd)	CTACCACAGAGGCCTTGCC
Tnc (Rev)	AGCAGCTTCCCAGAATCCAC

3.3.3 Schwann cell conditioned media treatments and aneural clustering assay

Schwann cells were cultivated in T75 flasks until reaching full confluency. Post confluence, cells were washed with warm F12 medium and then incubated with Schwann cell growth medium with either absence (0 μM) or presence (100 μM) of PQ. After a 48-hour period, the conditioned media were collected and prepared by combining equal parts with fresh C2C12 differentiation media, yielding three media variations: control, Schwann cell-conditioned (SC-CM), and activated Schwann cell-conditioned (*a*SC-CM) media. All collected media were sterile filtered with 0.4 μm syringe filter prior to use.

In parallel, C2C12 myoblasts at passages 3-5 were cultured to approximately 70% confluence, after which differentiation was induced using DMEM with 2% horse serum. At day 5

of differentiation, the formed myotubes were treated with control, SC-CM, or *a*SC-CM media for four hours. To produce aneural clusters in the presence of Agrin, some myotube cultures received control media with recombinant Agrin (1 nM) for the same duration to induce AChR clustering. A final set was exposed to a 10 minute pulse of recombinant Agrin, followed by the aforementioned conditioned media treatments for the remainder of the four-hour period. AchRs were labeled by the binding of Alexa Fluor 488 α-Bungarotoxin (α-BTX) (Invitrogen). Myotubes were incubated with the α-BTX diluted (1:500) in differentiation media for 1 hour at 37°C in 5% CO2. The number of AchR clusters per field in their longest dimension (≥25 μm) was measured using ImageJ software.

3.3.4 Schwann cell immunofluorescent staining, imaging, and analysis

For immunofluorescent characterization of Schwann cells, we performed a series of staining procedures to detect specific cell markers. Cultures were first fixed using a 4% paraformaldehyde (PFA) solution for 10 minutes and subsequently treated with ice cold methanol for 1 minute to permeabilize the cells. Blocking was achieved with a 4% solution of goat serum in PBS to prevent non-specific antibody binding, for 30 minutes. Primary antibodies against S100B (DAKO) and Ki67 were applied to the cells and left to bind overnight at 4°C.

Following primary antibody binding, cells were subjected to an hour-long incubation at room temperature with fluorescently-labeled secondary antibodies conjugated to Alexa Fluor dyes (Life Technologies). Concurrently, nuclei were counterstained with 4′,6-diamidino-2-phenylindole (DAPI). Imaging was performed using a Lionheart tabletop inverted microscope (Biotek), capturing images at 10x magnification. We ensured reproducibility and statistical relevance by obtaining three random fields of view from each well for each experimental condition.

3.3.5 Statistical Analysis

Data are presented as the mean ± SEM**.** All statistical analyses were performed using GraphPad Prism 8 (GraphPad Software). Between-group differences were tested by a one-way analysis of variance (ANOVA) followed by Dunnett's multiple comparisons test. Differences were considered to be statistically significant at the $P < 0.05$ level (*p < 0.05, **p<0.01, ***p < 0.001, ns: not significant).

3.4 Results

3.4.1 Schwann cells are activated in response to paraquat treatment and upregulate trophic gene expression

We first examined the cytotoxic impact and reactive oxygen species (ROS) induction by paraquat (PQ) on primary rat Schwann cell cultures across a range of PQ concentrations (**Figure 3.1.A**). Following a 48-hour period of PQ exposure, cell viability assessments revealed a significant decline to 50% at 100 µM PQ and to 25% at 250 µM PQ, with total lethality at 500 µM PQ. ROS generation was confirmed through increased fluorescence intensity in CellROX-stained cells in a dose-responsive manner compared to untreated controls (**Figure 3.1.B**). Immunofluorescence staining for the Schwann cell marker S100B and the proliferation marker Ki67 after PQ treatments corroborated the cell viability findings (**Figure 3.1.C**). Statistical analysis indicated a 50% reduction of S100B+ and Ki67+/S100B+ cell populations at the 100 µM PQ dose relative to both control and 10 µM PQ treatments (**Figure 3.1.D**). RT-qPCR assays post-treatment displayed more than a two-fold increase in *Gdnf* and *Ngfr* mRNA expression at the 100

µM PQ level, implying activation of Schwann cell repair mechanisms. Additionally, the expression of *c-Jun* and *Agrn* was also elevated, indicating a potential shift towards cellular repair

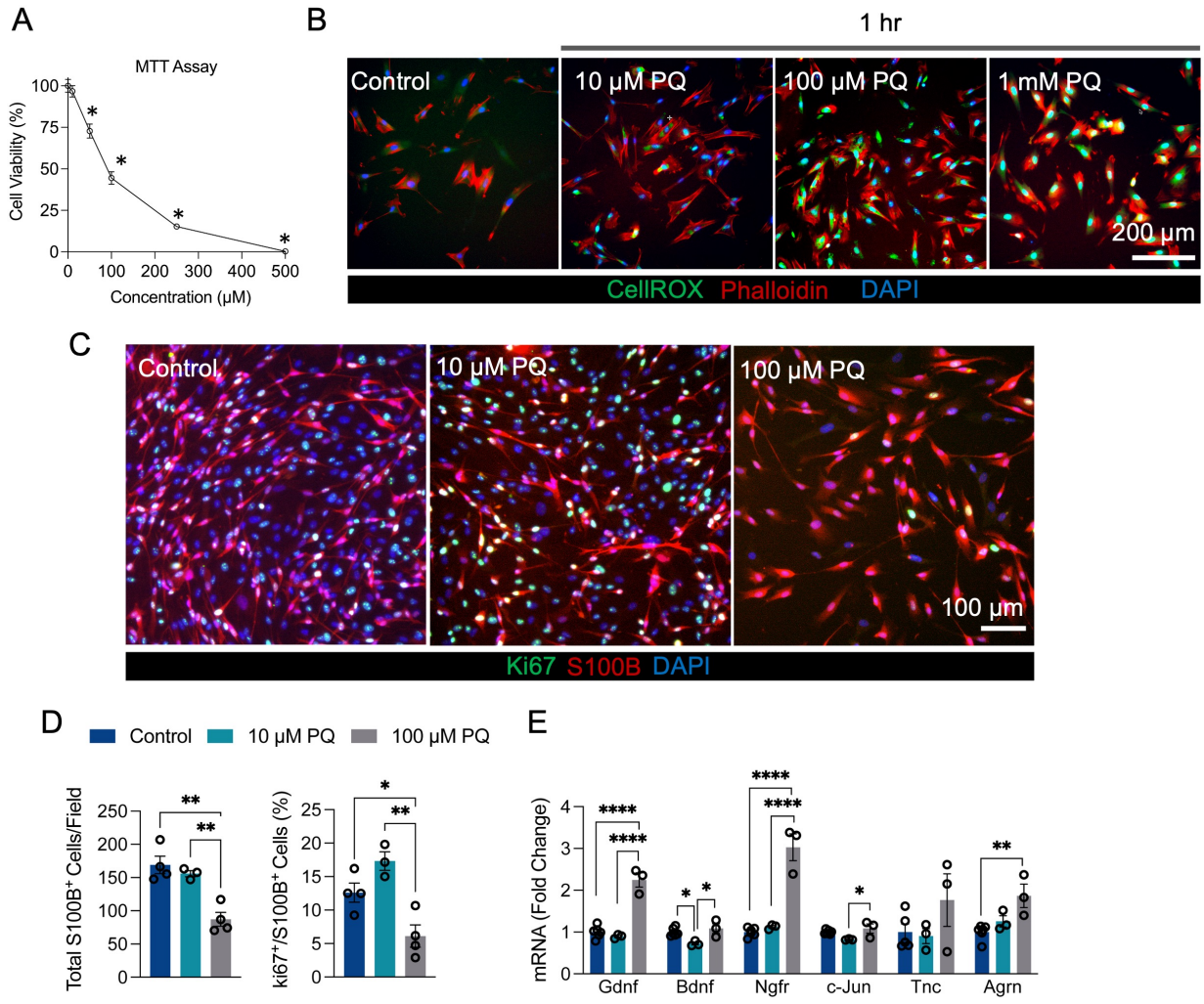

Figure 3.1: Impact of Paraquat on Schwann Cell Dynamics and Gene Expression. (**A**) MTT assays reveal a dose-dependent decrease in cell viability corresponding to higher Paraquat (PQ) concentrations. (**B**) Visualization of primary Schwann cells using CellRox (Green) for oxidative stress, Phalloidin (Red) for cytoskeletal F-actin, and DAPI (Blue) for nuclear staining following one hour of PQ exposure. (**C**) Immunofluorescence images display Schwann cells with S100B (Red) labeling, proliferative activity via Ki67 (Green), and nuclear identification with DAPI (Blue). (**D**) Analysis of immunostained cells demonstrates diminished counts of S100B-positive and double-labeled Ki67/S100B cells post-treatment with 100 µM PQ, relative to control and 10 µM PQ-treated counterparts. (**E**) RT-qPCR data present transcriptional levels of genes indicative of Schwann cell repair phenotype and neuromuscular junction organization under PQ treatment. Error bars represent mean ± SEM. Statistical significance is indicated by an asterisk (*) following One-way ANOVA testing.

processes and the secretion of factors related to post-synaptic AChR clustering. These findings

collectively point to the upregulation of repair pathways in Schwann cells under sublethal oxidative stress conditions.

3.4.2 Enhanced AChR Cluster Formation in C2C12 Myotubes by Activated Schwann Cell Media

We next wanted to determine whether Schwann cells stimulated to upregulate repair programs due to increased ROS levels can influence aneural AChR clustering in differentiated C2C12 myotubes. Conditioned media were collected from both untreated (SC-CM) and 100 µM PQ-activated Schwann cells (*a*SC-CM) after a 48-hour incubation (**Figure 3.2.A**). Differentiated C2C12 myotubes were then exposed to these conditioned media for a period of four hours, after which aneural AChR clustering was assessed (**Figures 3.2.B-C**). The analysis revealed a notable increase in AChR cluster formation in myotubes treated with *a*SC-CM, compared to those treated with SC-CM and untreated control myotubes (**Figure 3.2.C**).

Given the known efficacy of recombinant Agrin in inducing AChR clustering in myotubes in culture, our study further explored the comparative effects of SC-CM and *a*SC-CM in alongside Agrin treatment. Consistent with expectations, a pronounced induction of AChR clusters was noted following a four-hour Agrin exposure (**Figure 3.2.B,D**). Interestingly, a brief ten-minute Agrin application followed by *a*SC-CM treatment for the remainder of the period yielded AChR cluster numbers statistically similar to the extended four-hour Agrin exposure (**Figure 3.2B,D**). This suggests that the presence of factors secreted by Schwann cells under elevated ROS conditions can initiate and enhance AChR clustering, particularly when combined with Agrin. Overall, these findings demonstrate that Schwann cells, when activated by ROS, secrete factors capable of inducing and potentiating AChR clustering in myotubes.

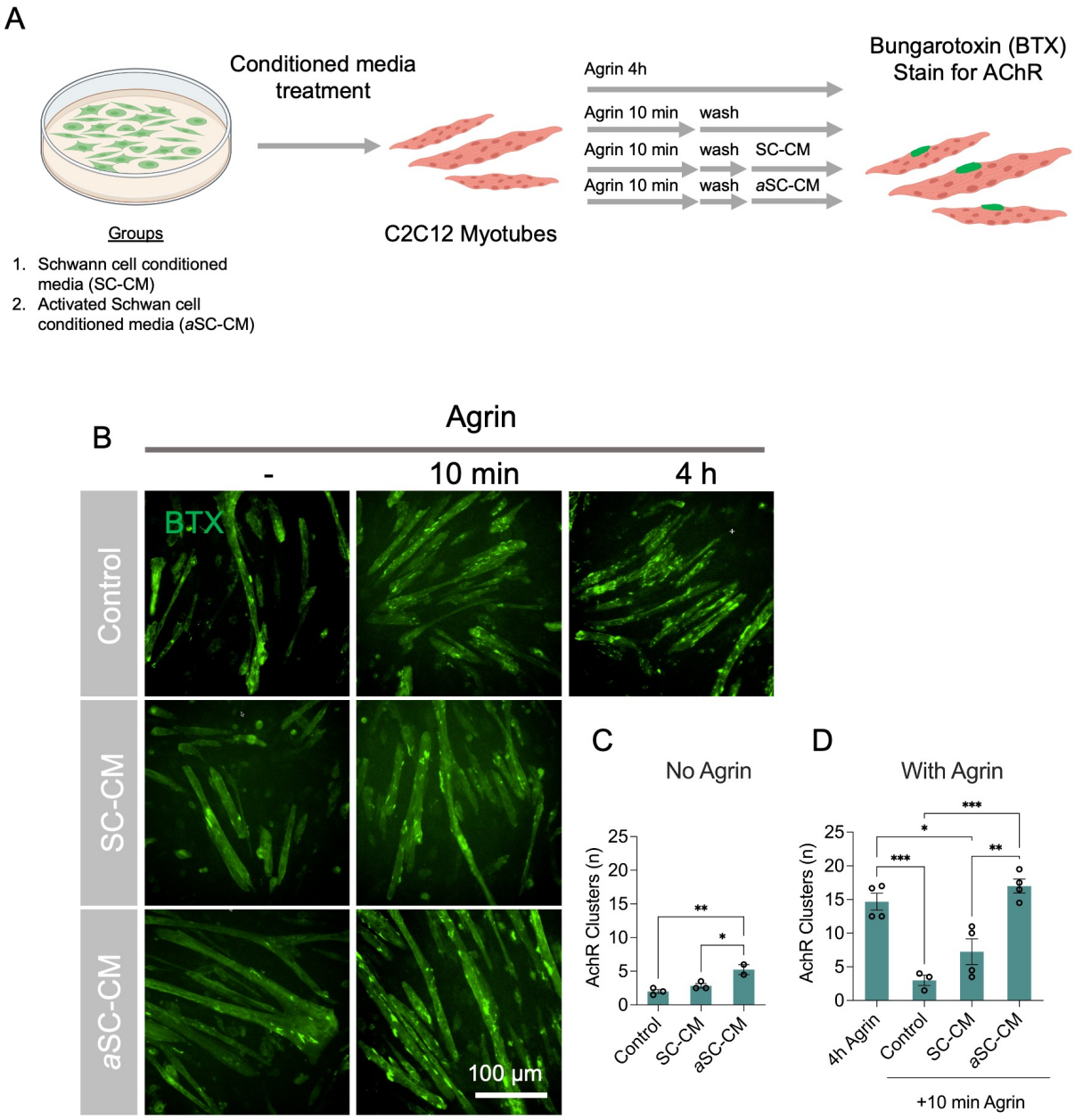

Figure 3.2: Enhanced AChR Cluster Formation in Myotubes by Conditioned Media from Activated Schwann Cells. (**A**) A schematic representation of the experimental design. (**B**) Immunofluorescent (IF) images of myotubes treated with various media: control, Schwann cell conditioned media (SC-CM), activated Schwann cell conditioned media (aSC-CM) treated with 100 µM PQ, and combinations of Agrin treatments (1 nM for 10 minutes or 4 hours, and 10-minute Agrin followed by SC-CM or aSC-CM). (**C**) Analysis of AChR clusters (longer than 25 µm) from IF images revealed a significant increase in cluster formation in myotubes treated with aSC-CM compared to those treated with control media or SC-CM. (**D**) Regarding Agrin-induced clustering, myotubes exposed to 4 hours of Agrin and those treated with a 10-minute Agrin pulse followed by aSC-CM demonstrated a higher count of AChR clusters compared to myotubes treated with a 10-minute Agrin pulse alone or with SC-CM. Bars show the mean ± SEM. *Denotes significance by One-way ANOVA.

3.5 Discussion

This study offers significant insights into the dynamic response of Schwann cells to oxidative stress and their subsequent influence on NMJ architecture, particularly in the context of AChR clustering in myotubes. Our findings reveal a dual aspect of ROS in Schwann cells: a mediator of cellular damage at high concentrations and a trigger for trophic support pathways at sublethal levels.

We observed that exposure to PQ, an inducer of ROS, led to a dose-dependent decline in Schwann cell viability, with a notable reduction at higher concentrations. This outcome is consistent with the known cytotoxic effects of excessive ROS. Intriguingly, at sublethal concentrations, Schwann cells exhibited an upregulation of genes associated with repair mechanisms, such as *Gdnf* and *Ngfr*. This suggests that ROS, at controlled levels, can act as a stimulus for Schwann cells to enter a reparative state, potentially recapitulating the response to nerve injury[81,85].

The influence of Schwann cells on NMJ dynamics was further highlighted by the impact of Schwann cell conditioned media on AChR clustering in C2C12 myotubes. Myotubes treated with media from ROS-activated Schwann cells showed enhanced AChR clustering compared to untreated controls, underscoring the role of Schwann cell-derived factors in modulating NMJ structure. This effect was further amplified when combined with Agrin, a known inducer of AChR clustering[18,147], indicating a synergistic interaction between Schwann cell-secreted factors and Agrin. Given the proximity of terminal Schwann cells to skeletal muscles at the NMJ, and considering our gene expression data which indicated upregulation of *Agrin* and *Gdnf*, we propose that these proteins might play a significant role in either directly inducing or enhancing AChR clustering, respectively. However, the specific mechanisms through which GDNF may influence

endplate size expansion remain unclear and warrant further investigation. Additionally, the possibility that other unidentified proteins or non-protein factors, such as metabolites, in the Schwann cell media contribute to AChR clustering cannot be ruled out. Comprehensive future studies employing techniques like bulk RNA sequencing or proteomics are needed to identify these potential contributing molecules that are producing the AChR clustering effects in vitro and further our understanding of the molecular underpinnings of NMJ remodeling by Schwann cells. Moreover, to substantiate the relevance of these findings within the context of whole muscle tissue, in vivo validation is imperative. Given the strategic localization of tSCs at the post-synaptic membrane and their proximity to subsynaptic myonuclei[148] — the primary myonuclei subtype expressing AChR proteins — it is plausible that a signaling crosstalk between subsynaptic nuclei and tSCs is vital for mediating AChR clustering. This interaction is hypothesized to become more pronounced during muscle denervation, due to an increase in tSC numbers and closer physical association in the absence of the nerve terminal[43,45]. Advanced techniques such as single-nuclei RNA-Sequencing from denervated muscles coupled with intercellular network analysis could offer profound insights into the critical signaling pathways that govern communication between Schwann cells and myonuclei.

Our findings align with the broader understanding of ROS as a double-edged sword in cellular biology. While high levels of ROS are detrimental, moderate ROS elevation can serve as a signaling mechanism, activating pathways that promote tissue repair and regeneration[130,134,135]. In the context of Schwann cells, this balance appears crucial for their role in nerve repair and NMJ maintenance[139]. This study not only advances our understanding of Schwann cell biology but also opens avenues for therapeutic strategies targeting oxidative stress in neuromuscular disorders. By harnessing the ROS-responsive pathways in Schwann cells, it might be possible to enhance nerve

repair and NMJ function, particularly in aging and disease states characterized by oxidative stress. Future investigations into the specific factors secreted by ROS-activated Schwann cells and their direct effects on NMJ components could provide further clarity on this promising therapeutic potential.

Chapter 4 Decoding Muscle-Resident Schwann Cell Dynamics During Neuromuscular Junction Remodeling in *Sod1*$^{-/-}$ Mice

4.1 Abstract

Neuromuscular junction (NMJ) integrity is crucial for effective muscle function and voluntary movement. Disruption of NMJ communication is a hallmark of neuromuscular diseases like amyotrophic lateral sclerosis (ALS) and sarcopenia. Understanding the mechanisms of NMJ maintenance and regeneration is therefore pivotal for developing therapeutic interventions. We utilized Sod1-/- mice, a model exhibiting progressive NMJ degeneration, crossed with S100GFP-tg mice to visualize Schwann cells. We conducted functional, molecular, and morphological evaluations of NMJs between 1 and 3 months of age. This included in situ gastrocnemius muscle contractility assessments, RT-qPCR analysis of genes involved in neuromuscular denervation and Schwann cell activation, and high-resolution imaging to evaluate NMJ structure and Schwann cell responses. Our findings identified a significant NMJ 'regenerative window' in Sod1-/- mice, characterized by a transient but recoverable impairment in neurotransmission, particularly at 2 months. Molecular analyses showed increased expression of genes linked to NMJ remodeling. Morphological assessments revealed an increase in terminal Schwann cell (tSC) numbers and synaptic area, indicating active NMJ repair. Single-cell RNA sequencing of muscle-resident Schwann cells unveiled two distinct tSC subtypes, with the tSC-B subtype being predominantly increased in Sod1-/- mice. This subtype displayed a unique transcriptomic profile associated with synapse organization and neuron projection extension, highlighting its potential role in NMJ reinnervation. Our study reveals critical insights into the dynamics of NMJ remodeling and

reinnervation in a model of progressive NMJ degeneration. We demonstrate the presence of a regenerative window, significant Schwann cell proliferation, and the emergence of a novel Schwann cell subtype during NMJ repair. These findings contribute to our understanding of Schwann cell biology in NMJ maintenance and provide a foundation for future therapeutic strategies targeting neuromuscular degeneration.

4.2 Introduction

The neuromuscular junction (NMJ) is the terminal synapse of the motor system, orchestrating muscle contraction and, by extension, voluntary movement. Effective neurotransmission at the NMJ is paramount for neuromuscular communication, with any degenerative alterations at the synapse having the potential to impair muscle contractile function and overall mobility. NMJ degeneration and denervation are pivotal contributing factors to the onset and progression of degenerative neuromuscular diseases, such as amyotrophic lateral sclerosis (ALS)[149,150], and sarcopenia, the age-related loss of muscle mass and function[7]. Incomplete understanding of mechanisms that control NMJ maintenance and regeneration represents a critical barrier to the development of effective therapeutic interventions for these and other devastating conditions.

The major cellular components of the NMJ are the pre-synaptic motor neuron (MN), the post-synaptic muscle fiber, and supporting glia. The primary glial cell type at the NMJ is a specialized non-myelinating Schwann cell population referred to as terminal Schwann cells (tSCs). tSCs regulate synaptic activity[151], and tSC proliferation is critical to generate a sufficient number of Schwann cells to sustain the physiological regenerative response required for effective muscle reinnervation[43,152]. Despite the importance of SCs and SC proliferation in promoting muscle fiber reinnervation, the cell biology and physiology of muscle resident SCs and their response to denervation remain poorly understood.

Widespread and progressive NMJ degeneration and denervation are prominent phenotypes of *Sod1*$^{-/-}$ mice, which lack the enzyme superoxide dismutase 1 (Sod1), making them a broadly used model for testing hypotheses focused on the regulators of NMJ structure and function[153–155]. An intriguing recent revelation from this mouse model is a distinct timeframe early in life during which the expression in muscles of acetylcholine receptor alpha (Chrna) mRNA levels and mitochondrial reactive oxygen species (mtROS) production are dramatically but transiently elevated[156]. Upregulation of Chrna and mtROS production are both known to increase significantly in response to muscle denervation[136,157,158]. The pattern of transient increases around 2 months of age and return to baseline by 3 months for both Chrna mRNA and mtROS suggests a robust denervation/reinnervation event that identifies a potential 'regenerative window' in which the regulation of NMJ repair processes can be examined in detail.

To comprehensively assess the role of muscle-resident Schwann cells in NMJ remodeling and muscle fiber reinnervation, we crossed *Sod1*$^{-/-}$ mice with *S100GFP*-tg mice[159] that express green fluorescent protein driven by the S100B promoter, to create *S100GFP*-tg *Sod1*$^{-/-}$ mice, in which Schwann cells could be easily visualized and subsequently isolated for detailed molecular analysis. Using these mice, we assessed functional innervation, evaluated morphological features of tSCs in conjunction with pre- and post-synaptic structural attributes of NMJs, and performed single-cell RNA-sequencing on muscle-resident Schwann cells during the putative regenerative window between 1 and 3 months of age. We validated the occurrence and time course of an extensive denervation event followed by a successful reinnervation response that involves substantial tSC proliferation. Our muscle Schwann cell sequencing data provides single-cell resolution unprecedented in existing data sets, elucidating several muscle-resident Schwann cell subtypes,

including the emergence of a previously unreported tSC subtype associated with the denervation-reinnervation response marked by a neurogenic transcriptomic signature.

4.3 Methods

4.3.1 Animal Models

All experimental procedures were approved by the University of Michigan Institutional Animal Care and Use Committee (PRO00010548) and conducted in accordance with National Institutes of Health guidelines. Animals were sacrificed via intraperitoneal injection of tribromoethanol, followed by administration of a pneumothorax.

All mice used for experimentation were bred at the University of Michigan with *Sod1*$^{-/-}$ and WT mice initially provided generously by Dr. Holly Van Remmen while she was at the University of Texas Health Science Center at San Antonio[160]. Mice expressing enhanced Green Fluorescent Protein (GFP) driven by the S100B promoter to visualize Schwann cells (S100GFP-tg Kosmos mice)[159] were generously provided by Dr. Alison Snyder-Warwick at Washington University in St. Louis, MO. *S100GFP*-tg mice were crossed with *Sod1*$^{-/-}$ mice to form a first generation of mice that contained a knockout allele for Sod1 and wild type allele for the Sod1 gene and the S100GFP transgene, S100GFP-tg *Sod1*$^{+/-}$. First generation mice were crossed to generate a second generation of *Sod1*$^{-/-}$ mice expressing GFP under the S100B promoter to be used for our experiments. To maintain a stable colony of *S100GFP*-tg *Sod1*$^{-/-}$ mice, male *S100GFP*-tg *Sod1*$^{-/-}$ and female S100GFP-tg *Sod1*$^{+/-}$ mice were consistently bred to produce litters with approximately 50% of the mice containing the experimental genotype, *S100GFP*-tg *Sod1*$^{-/-}$. Control mice in this study contain the genotype, S100GFP-tg *Sod1*$^{+/+}$, simply referred to as S100GFP-tg.

4.3.2 In situ Force Testing

Mice were anesthetized with initial intraperitoneal injections of Avertin (tribromoethanol, 250 mg/kg) with supplemental injections to maintain an adequate level of anesthesia during all procedures. Gastrocnemius (GTN) or tibialis anterior (TA) muscle contractile properties were measured in situ, as described by Larkin et al. (2011)[161]. In anesthetized mice, the whole GTN or TA muscle was isolated from surrounding muscle and connective tissue using great care not to damage the nerve and/or blood vessels during the dissection. A 4-0 silk suture was tied around the distal tendon and the tendon was severed. The animal was then placed on a temperature-controlled platform warmed to maintain body temperature at 37°C. The hindlimb was secures to the platform, and the tendon was tied to the lever arm of a servomotor (model 6650LR, Cambridge Technology). A continual drip of saline warmed to 37°C was administered to the muscles to maintain temperature. Muscles were activated either by stimulation of the tibial (GTN muscle) or common peroneal (TA muscle) nerve using a bipolar platinum wire electrode or by direct stimulation of the muscle via cuff electrodes wrapped around the proximal and distal ends of the muscle. Custom-designed software (LabVIEW 2018; National Instruments, Austin, TX) controlled electrical pulse properties and servomotor activity and recorded data from the force transducer. The voltage of 0.2 ms stimulus pulses was increased, and optimal muscle length (Lo) was subsequently adjusted, to give maximum twitch force. The Lo was measured with digital calipers. Muscles were held at Lo and subjected to 300 ms trains of pulses with increase stimulation frequencies maximum isometric force (Po) was achieved. Previously established Lf-to-Lo ratios of 0.45 for GTN muscles and 0.6 for TA muscles were used to calculate Lf for each muscle. The physiological cross-sectional area (CSA) of muscles was determined by dividing the mass of the muscle by the product of Lf and 1.06 g/cm3, the density of mammalian skeletal muscle[162]. Po was normalized by the CSA to

calculate specific Po (sPo), as a measure of intrinsic force generating capacity. Functional innervation was assessed by calculating the ratio of force production in response to nerve stimulation relative to the force elicited by direct muscle stimulation. A value of 1.0 indicates high fidelity of the nerve-muscle functional connections, while the extent to which the ratio is less than 1.0 provides an indication of the fraction of muscle fibers that are unable to respond to nerve stimulation.

4.3.3 Immunofluorescent Staining and Imaging

Animals were sacrificed and the muscles were fixed in 4% paraformaldehyde (PFA) in PBS for 15 min and sucrose protected overnight with 20% sucrose, followed by embedding in optimal cutting temperature (OCT) compound (Tissue Tek) and stored at -80°C prior to use. For visualization and examination of neuromuscular junction (NMJ) structure, muscles were dissected using fine forceps to tease muscle fibers into layers consisting of a maximum of 10-20 muscle fibers. The samples were then treated with ice cold methanol for 30 seconds, washed 3 times in PBS for 5 min each, then blocked for 30 minutes at room temperature in 5% goat serum, PBS, triton X-100 (0.5%), and 2% bovine serum albumin (BSA). Fab fragments (10% in blocking solution) were used to block endogenous IgG before applying any mouse monoclonal primary antibodies. Muscle fiber bundles were then stained with antibodies and mounted on a slide, and coverslips were applied.

Primary antibodies used for this experiment were as follows: a combination of NF and SV2 (Developmental Studies Hybridoma Bank) for labeling α-motor axon terminals and axons, anti-S100 (Dako, Z0311) to enhance labeling of all SCs, anti-Ki67 (rat), anti-SPP1 (Abcam, ab8448), and anti-CD44 (Thermo Fisher Scientific, 50-143-16). Secondary antibodies consisted of Alex Fluors that were conjugated to the secondary antibodies (Life Technologies). α-BTX conjugated

to Alexa Fluor 555 (Invitrogen, B35451) was used to label the acetylcholine receptors (AChR), and 4′,6-diamidino-2-phenylindole (DAPI) was used to label all nuclei.

A Nikon A1 high-sensitivity confocal laser scanning microscope with 40× oil immersion objective was used to capture 16-bit, 512×512-pixel frame size, Z-stack images with 1 μm interval. A minimum of 20-30 NMJs were acquired per animal.

4.3.4 NMJ Feature Quantification

Fiji software was used for quantitative analysis of confocal micrographs. All analyses were performed on maximum intensity projections using guidelines described in detail in the NMJ-Morph image processing pipeline.[163] The obtained images were preserved as nd2 Nikon files and subsequently imported into ImageJ software, with channels consolidated into a single tiff image prior to their separation for individual component analysis. Initial preparations involved the division and cropping of images to ensure each contained a singular NMJ, enabling individual analysis of each NMJ. The analysis was constrained to en-face NMJs only.

For each channel, a threshold was set using the thresholding tool to produce a binary mask that most closely resembled the real image of the NMJ component being analyzed. The binary mask was selected and measured to provide the area and perimeter of the selected channel (**Figure 4.2**). The endplate mask was generated by applying the 'Create background' FIJI tool on the AChR mask, which completely fills in the AChR mask. Endplate area and diameter were also measured (**Figure 4.2A**). This process was repeated for every NMJ image, for each of the NMJ components.

The 'Overlap' and 'SC Coverage' measurements (**Fig 4.2D,E**) were derived in accordance to NMJ-Morph guidelines. Briefly, the following calculations were used:

$$Overlap, SC\ Coverage = \left[\frac{AchR\ Area - unoccupied\ area\ of\ AChR}{AChR\ Area}\right] \times 100$$

$$Synaptic, SC\ Coverage\ Area\ = AchR\ Area - unnocupied\ area\ of\ AChR$$

The unoccupied area denotes regions lacking colocalization with α-BTX. Following the generation of a binary mask for calculating the AChR, nerve teriminal, and tSC areas (**Figure 4.3A-C**), the masks were processed, inverted as needed, and merged to measure unoccupied areas of AChR. Beyond structural area measurements, attention was given to NMJs manifesting visible polyinnervation—characterized by the convergence of at least two axons onto a single NMJ (**Figure 4.3F**). Furthermore, the presence of axon terminal blebs per NMJ was recorded (**Figure 4.3F**).

4.3.5 NMJ UMAP and k-means clustering analysis

Raw data for all sixteen NMJ features described above were imported into *R*. The numeric dataset underwent Z-score normalization through the scale() function in *R*. This normalization ensured a transformation of every individual feature to attain a mean of 0 and a standard deviation of 1, critical for subsequent analyses. Uniform Manifold Approximation and Projection (UMAP) was performed, using the 'umap' package on R, on the scaled data using a fixed seed to ensure reproducibility. Our decision on the optimal number of clusters—set at four—was steered by a combination of unbiased clustering methods combined with domain insights. Notably, our emphasis was on segregating the densely populated region on the UMAP associated with the 2-

month-old *Sod1*$^{-/-}$ NMJs from control NMJs, while also achieving a graded cluster distinction within the control region. Using the kmeans() function in *R* each NMJ was assigned to a specific cluster. The generated clusters were then visualized and overlaid on the original UMAP plot to depict the identified groupings distinctly. All plots were generated using ggplot2.

4.3.6 Quantification of Perisynaptic and Extrasynaptic Ki67+ Nuclei

Muscle fiber bundles from 2-month-old *S100GFP*-tg and *S100GFP*-tg *Sod1*$^{-/-}$ were processed and stained with anti-Ki67, DAPI, α-BTX, and anti-S100B to delineate nuclei and cellular structures. Confocal imaging was performed using a Nikon A1 microscope, with images captured at 20X and 40X magnifications. The imaging focused on fields containing NMJs along with visualization of the surrounding areas. Classification of perisynaptic Ki67+ nuclei involved those being DAPI+ Ki67+ and overlapping with α-BTX stain. Perisynaptic Ki67+ GFP+ nuclei were identified as DAPI+ Ki67+ S100GFP+ and overlapping with an endplate (α-BTX stain). Extrasynaptic Ki67+ nuclei were those located within 50 μm from the nearest endplate. The quantification was normalized by the number of NMJs per image field to ensure comparability across different fields and conditions. A minimum of 50 NMJs were analyzed across each sample.

4.3.7 Single cell isolation via FACS

For tissue collection, mice were anesthetized with 3% isoflurane, then euthanized by cervical dislocation, bilateral pneumothorax, and removal of the heart. Hind limb muscles (TA and GTN) of control and experimental mice were quickly harvested using sterile surgical tools and placed in separate plastic petri dishes containing cold phosphate-buffered saline (PBS). Using surgical scissors, muscle tissues were minced and transferred into 50 mL conical tubes containing

20 mL of digest solution (2.5 U/mL Dispase II and 0.2% [~1000 U/mL] Collagenase Type II, 1 mg/mL of hyaluronidase in Dulbecco's modified Eagle medium [DMEM] per mouse). Samples were incubated on a rocker placed in a 37℃ incubator for 60 min with manual pipetting the solution up and down to break up tissue every 30 min using an FBS-coated 10 mL serological pipette. Once the digestion was completed, 20 mL of F12 media containing 20% heat inactivated FBS was added into each sample to inactivate enzyme activity. The solution was then filtered through a 70 mm cell strainer into a new 50 mL conical tube and centrifuged again at 300g for 5 min. Live cells were sorted from the suspension via addition of 1 μg of propidium iodide (PI) stain into each experimental sample and all samples were filtered through 70 mm cell strainers before the FACS. Cell sorting was done using a BD FACS Aria III Cell Sorter (BD Biosciences, San Jose, CA). GFP+ PI- and GFP- PI- cells were sorted into 0.02% BSA PBS solution for immediate processing.

4.3.8 scRNA sequencing

Freshly isolated single cells were sorted into staining solution, enumerated by hemocytometer, and re- suspended into PBS. Cells were loaded into the 10X Genomics chromium single cell controller for each sample and captured into nanoliter-scale gel bead-in-emulsions. cDNAs were prepared using the single cell protocol as per manufacturer's instructions and sequenced on a NovaSeq instrument (Illumina) with 26 bases for read 1 and 98 bases for read 2.

4.3.9 scRNA-Seq data processing and analysis

Cell Ranger 7.1.0 (10X Genomics) was used to process raw data. The CellRanger workflow aligns sequencing reads to the mm10 transcriptome using the STAR aligner and exports count data[164]. The CellRanger count command was run with default parameters. Filtered feature

barcode data were imported into Seurat (v4.3)[165]. Ambient RNA was removed using Decontx[166] and only cells with greater than 200 genes and <10% mitochondrial reads were included in our analysis. Scaling, normalization, variable gene selection, dimensionality reduction, and clustering were performed with default settings using the Seurat. Cell types were assigned to each cluster using known marker genes. Pathway analysis was performed using enrichGO() function in clusterProfiler[167] with the default parameters and used gene markers that were upregulated (log2FC > 1) in the tSC-B cluster compared to all other muscle-resident Schwann cells as the gene list. Upregulated genes were determined using the FindMarkers() function in Seurat. Secreted signaling intercellular interaction analysis was performed using the CellChat package with standard parameters and setting the CellChat database to "Secreted Signaling".[168]

4.3.10 Whole-tissue RNA extraction and RT-qPCR Analysis

GTN and TA muscle samples were homogenized in TRIzol reagent (Invitrogen, Thermo Fisher Scientific) using a bead mill. RNA was isolated by phenol/chloroform extraction and RNA yield was determined using a NanoDrop Spectrophotometer (NanoDrop 2000c, Thermo Fisher Scientific). Genomic DNA was removed by incubation with DNase I (Ambion, Thermo Fisher Scientific, AM2222) followed by its heat inactivation. Total RNA (1 μg) was reverse-transcribed to cDNA using SuperScript III Master Mix, Random Hexamers, and dNTPs (Invitrogen, Thermo Fisher Scientific) and RT-qPCR performed on a CFX96 Real-Time PCR Detection System (Bio-Rad, 1855195) in triplicate 20 μL reactions of iTaq Universal SYBR Green Supermix (Bio-Rad, 1725124) with 1 μM forward and reverse primer. Relative mRNA expression was determined using the $2^{-\Delta\Delta CT}$ method with Gapdh serving as a control for the samples. Primer sequences used in this study can be found in **Table 4.1**.

Table 4.1: Primers used for RT-qPCR

Name	Sequence
Mki67 (Fwd)	AATCCAACTCAAGTAAACGGGG
Mki67 (Rev)	TTGGCTTGCTTCCATCCTCA
Ccnd1 (Fwd)	AGACCATTCCCTTGACTGC
Ccnd1 (Rev)	AAGCAGTTCCATTTGCAGC
Agrn (Fwd)	TTCCTCAGCAACTACAAACCTG
Agrn (Rev)	TTCACACACAGCACCAAAGC
Gap43 (Fwd)	ATAACTCCCCGTCCTCCAAGG
Gap43 (Rev)	GTTTGGCTTCGTCTACAGCGT
Ngfr (Fwd)	TGCCTGGACAGTGTTACGTT
Ngfr (Rev)	ACAGGGAGCGGACATACTCT
Sox10 (Fwd)	AGATCCAGTTCCGTGTCAATAA
Sox10 (Rev)	GCGAGAAGAAGGCTAGGTG
Ntn1 (Fwd)	GCTGCAAGTGCAACGGCCAC
Ntn1 (Rev)	ATCGGTTGCAGGTGATGCCC
Gdnf (Fwd)	CCAGTGACTCCAATATGCCTG
Gdnf (Rev)	CTCTGCGACCTTTCCCTCTG
Cd68 (Fwd)	CGCCATTCAGCTCAGTCAGA
Cd68 (Rev)	CCACGTTTTAGCCAACAGCC
Gapdh (Fwd)	CACCATCTTCCAGGAGCGAG
Gapdh (Rev)	CCTTCTCCATGGTGGTGAAGAC
Bdnf (Fwd)	TCATACTTCGGTTGCATGAAGG
Bdnf (Rev)	AGACCTCTCGAACCTGCCC
c-Jun (Fwd)	CCTTCTACGACGATGCCCTC
c-Jun (Rev)	GGTTCAAGGTCATGCTCTGTTT
Tnc (Fwd)	CTACCACAGAGGCCTTGCC
Tnc (Rev)	AGCAGCTTCCCAGAATCCAC

4.3.11 Statistical analysis

Data are presented as the mean ± SEM**.** All statistical analyses were performed using GraphPad Prism 8 (GraphPad Software) and *R*. Between-group differences were tested by two-tailed unpaired students t-tests (2 groups) or by a one-way analysis of variance (ANOVA) followed

by Dunnett's multiple comparisons test. A two-way ANOVA followed by Tukey's multiple comparison's test was executed when two factors were involved. Differences were considered to be statistically significant at the $P < 0.05$ level (*p < 0.05, **p<0.01, ***p < 0.001, ns: not significant).

4.4 Results

4.4.1 Sod1$^{-/-}$ mice display dramatic denervation and reinnervation between 1 and 3 months of age.

To directly validate prior findings that suggest an early-life transient NMJ denervation and regenerative event in *Sod1*$^{-/-}$ mice[156], we performed functional, molecular, and morphological assessments of NMJ integrity on *S100GFP*-tg S*od1*$^{-/-}$ mice between 1 and 3 months of age. We first measured gastrocnemius (GTN) muscle contractile properties in situ in anesthetized mice using both nerve stimulation and direct muscle stimulation (**Figure 4.1A**). Comparing these two measurements provides an indication of the level of functional NMJ neurotransmission[169]. As indicated by the representative experimental records in **Figure 1B**, forces developed by muscles of 2-month-old *S100GFP*-tg S*od1*$^{-/-}$ mice during nerve stimulation were approximately 33% lower than controls, whereas the forces generated in response to direct muscle stimulation were not significantly different between the genotypes (**Figure 4.1B**). Thus, when comparing forces developed during nerve stimulation to those developed during direct muscle stimulation, a deficit of 25% was observed for 2-month-old *S100GFP*-tg S*od1*$^{-/-}$ mice compared with controls (**Figure 4.1C**) indicating the presence of a population of fibers that were not activated in response to nerve stimulation at this age. In contrast to the deficit observed at 2 months for *S100GFP*-tg S*od1*$^{-/-}$ mice, the nerve-to-muscle stimulation force ratio for *S100GFP*-tg mice remained consistent at approximate 1.0 across all ages consistent with a high degree of fidelity in functional

neurotransmission in control mice across all NMJs during this time window (**Figure 4.1C**). The impairments in neurotransmission in *S100GFP*-tg S*od1*$^{-/-}$ mice were observed only at 2 months, as indicated by no significant difference in the forces elicited by nerve and direct muscle stimulation at 1 month or 3 months (Fig 4.1c).

To investigate the activation of denervation response pathways in *S100GFP*-tg S*od1*$^{-/-}$ mice, we analyzed whole muscles by RT-qPCR and demonstrated increased mRNA levels compared to controls for putative genes involved in neuromuscular denervation, Schwann cell activation, and axonal growth (**Figure 4.1D**). These included genes associated with post-synaptic organization (Chrna1, Agrn)[170,171], Schwann cell repair and trophic support (Ngfr, Gdnf)[47,85], cell proliferation (Mki67, Ccnd1)[172–174], Schwann cell development (Sox10)[175], synapse elimination (Cd68)[71,176], and pre-synaptic axonal projection (Gap43, Ntn1)[177,178]. Transcriptional activation of denervation responsive genes and genes indicative of Schwann cell activation was observed in both GTN and tibialis anterior (TA) muscles in *S100GFP*-tg S*od1*$^{-/-}$ mice. Together, our functional data and qPCR data show that between 1 and 3 months of age *S100GFP*-tg S*od1*$^{-/-}$ mice experience transient but recoverable functional neuromuscular alterations with upregulation of molecular pathways known to be associated with NMJ remodeling. We next aimed to directly assess the integrity of the NMJs morphologically and define the cellular response of the tSCs.

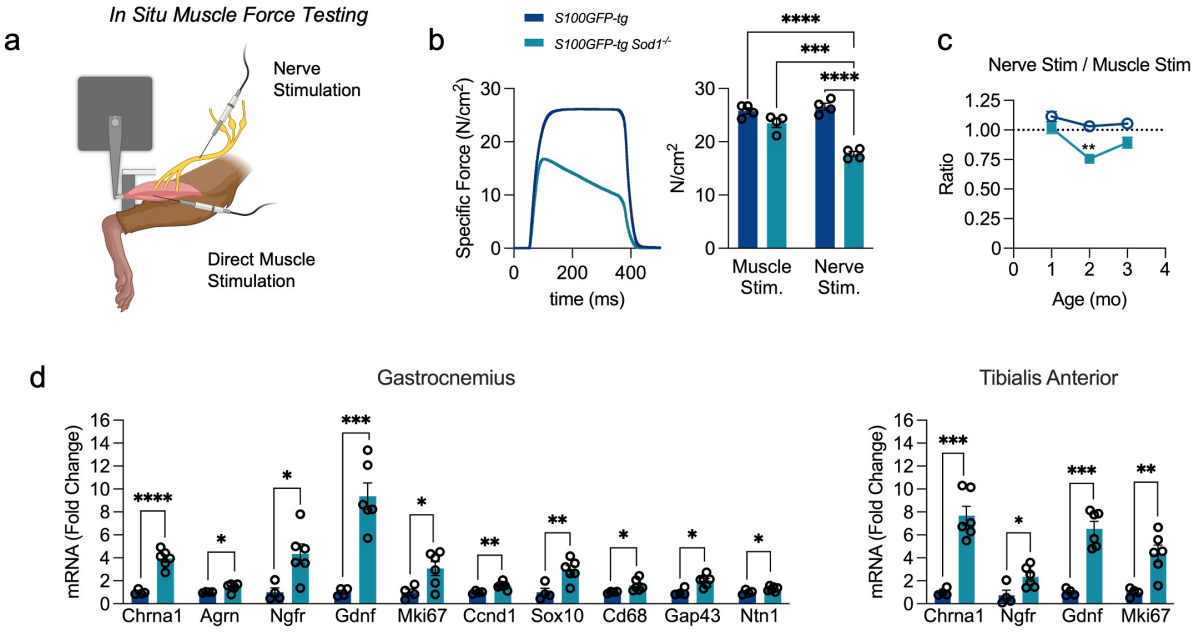

Figure 4.1: Muscle mechanics and transcriptional profiling of canonical markers reveal a marked but transient denervation/reinnervation response in young *S100GFP*-tg S*od1*$^{-/-}$ mice. (**A**) Illustration of in situ muscle force testing protocol used to determine NMJ transmission. Evoked muscle forces were evaluated in gastrocnemius (GTN) muscles from anesthetized mice by stimulating directly at the muscle or by indirect stimulation of the sciatic nerve. (**B**) Representative force traces for muscles of *S100GFP*-tg (blue) and *S100GFP*-tg *Sod1*$^{-/-}$ (teal) mice. Specific forces (N/cm^2) (n = 4 per genotype) evoked during maximum tetanic contractions. (**C**) Ratio of maximum isometric forces elicited by nerve stimulation relative to direct muscle stimulation across 1-3 months of age in *S100GFP*-tg *Sod1*$^{-/-}$ (n = 3-5) and *S100GFP*-tg control mice (n = 3-5). (**D**) RT-qPCR of canonical markers of NMJ regeneration, Schwann cell repair activation, cell proliferation, and axonal projection in whole GTN (n = 4-6) and tibialis anterior (TA) muscles (n = 4-6) of *S100GFP*-tg *Sod1*$^{-/-}$ and *S100GFP*-tg control mice. Open circles indicate values for each individual mouse and bars represent the mean response ± SEM. *P ≤ 0.05, **P ≤ 0.01, ***P ≤ 0.001, ****P ≤ 0.0001 *S100GFP*-tg vs *S100GFP*-tg *Sod1*$^{-/-}$ by two tailed unpaired t-test or 1-way ANOVA for multiple comparisons

4.4.2 The remodeling of neuromuscular junctions is associated with increased numbers of tSCs and larger synaptic areas

In addition to the functional and molecular assessments described above, we directly assessed the cellular and morphological response during the denervation-reinnervation event exhibited by *Sod1*$^{-/-}$ mice. We performed detailed imaging of fixed fiber bundles derived from *S100GFP*-tg S*od1*$^{-/-}$ and *S100GFP*-tg controls at 1, 2, and 3 months of age. Our comprehensive analysis covered NMJ structure, accounting for 16 distinct features related to pre- and post-

synaptic structures as well as tSC number and morphology (**Figure 4.2A,B**). Detailed descriptions of each morphological feature and how it was derived are described in **Figure 4.3**. Our findings revealed generalized decreases in *S100GFP*-tg *Sod1*$^{-/-}$ mice compared to controls in the nerve terminal perimeter and the overlap of the nerve terminal with AChRs by 33% and 60% respectively (**Figure 4.2C**). Meanwhile, the area of AChRs was observed to be 30% larger in S100GFP-tg *Sod1*$^{-/-}$ mice compared to controls. In addition, the total tSC area and count per NMJ were 60% and 3-fold greater, respectively, in the *S100GFP*-tg *Sod1*$^{-/-}$ group compared to controls (**Figure 4.2D**). As a result of the large increase in tSC number, the area per tSC was 38% smaller in *S100GFP*-tg *Sod1*$^{-/-}$ mice, suggesting a reduced tSC domain at the NMJ. Given that both central and peripheral glia respond to neuronal injury by increasing cell number[43,179], increased tSC number and area at the NMJ are likely acting to protect or promote NMJ integrity during the early neuromuscular events linked to the *Sod1*$^{-/-}$ phenotype.

Both the degree of overlap and the size of the synaptic area serve as indicators of how well the pre- and post-synaptic components are in physical congruence[163]. These markers are robust histological indicators of nerve-to-muscle connections. The percentage of overlap between the nerve terminal and AChR was decreased at 2 months but returned to control levels by 3 months in *S100GFP*-tg *Sod1*$^{-/-}$ mice (**Fig 4.2E**). Re-establishment of control levels of overlap could be explained primarily by presynaptic responses, compensatory postsynaptic changes, or a combination. Our analysis revealed an expansion in synaptic area between 2 and 3 months in *S100*GFP-tg *Sod1*$^{-/-}$ mice driven largely by an enlargement in nerve terminal area at the age of 3 months (**Fig 4.4C**). The restoration in the degree of overlap coupled with the reduction in denervated NMJs (characterized by NMJs with less than 10% overlap) (**Figure 4.2E**) observed at 3 months collectively indicate muscle reinnervation.

In addition to considering specific features associated with NMJ structure individually, we also successfully distilled the 16 features of NMJ morphology measured into an overall assessment of the state of the NMJs through unbiased clustering using uniform manifold approximation and projection (UMAP) (**Figure 4.2F**) and k-means clustering (**Fig 4.2G**). This analysis resulted in four distinct NMJ clusters (**Fig 4.2G**). Clusters 1, 2 and 3 were predominantly composed of WT animals (all ages) and 1-month old *Sod1*$^{-/-}$ mice. Cluster 4, on the other hand, was only composed of NMJs from *Sod1*$^{-/-}$ mice, with nearly 76% of the NMJs in 2-month-old mice appearing in cluster 4. Consistent with the findings described above indicative of NMJ regeneration and reinnervation by 3 months in *Sod1*$^{-/-}$ mice, the majority of NMJs at this age appeared in one of the clusters associated with WT "innervated" NMJs; however, about 46% of the NMJs retained features that placed them in cluster 4 (**Fig 4.2G**). The radar plots and representative images depicted in **Figure 4.2H,I** illustrate the distinctive NMJ feature compositions within each cluster. Clusters 1 through 3 exhibited a high degree of overlap, with each subsequent cluster containing progressively larger NMJs. Cluster 4 is distinctive, presenting NMJs exhibiting higher numbers of tSCs, smaller nerve terminal dimensions, larger post-synaptic proportions, prevalent poly-innervation, and axonal blebbing. These results illuminate the heterogeneity and dynamic nature of NMJ morphology as well as the spectrum of structural modifications observable during NMJ remodeling both during normal development and in muscles experiencing partial denervation.

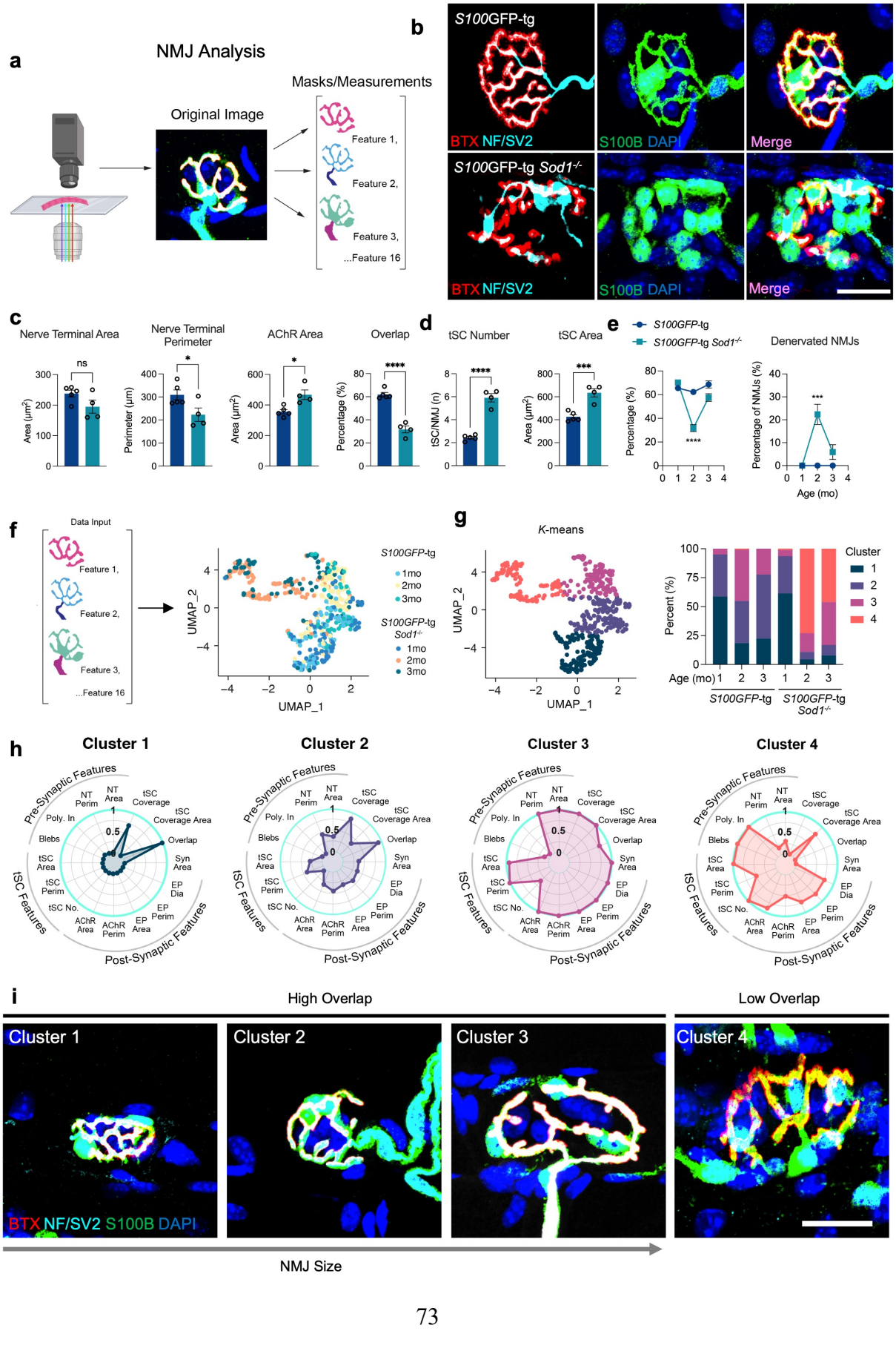
a
NMJ Analysis
Original Image
Masks/Measurements
Feature 1,
Feature 2,
Feature 3,
...Feature 16
b
S100GFP-tg
BTX NF/SV2
S100B DAPI
Merge
S100GFP-tg Sod1-/-
c
Nerve Terminal Area
Nerve Terminal Perimeter
AChR Area
Overlap
ns
Area (μm2)
Perimeter (μm)
Percentage (%)
d
tSC Number
tSC Area
tSC/NMJ (n)
e
S100GFP-tg
S100GFP-tg Sod1-/-
Denervated NMJs
Percentage of NMJs (%)
Age (mo)
f
Data Input
UMAP_1
UMAP_2
1mo
2mo
3mo
g
K-means
Percent (%)
Cluster
h
Cluster 1
Cluster 2
Cluster 3
Cluster 4
Pre-Synaptic Features
Post-Synaptic Features
tSC Features
NT Area
NT Perim
tSC Coverage
tSC Coverage Area
Overlap
Syn Area
EP Dia
EP Perim
EP Area
AChR Perim
AChR Area
tSC No.
tSC Perim
tSC Area
Blebs
Poly. In
i
High Overlap
Low Overlap
BTX NF/SV2 S100B DAPI
NMJ Size

Figure 4.2: The remodeling of neuromuscular junctions (NMJs) is associated with greater tSC numbers and larger synaptic areas in *S100GFP*-tg *Sod1*$^{-/-}$ mice. (A) Schematic of NMJ analysis – consisting of collecting NMJs images from muscle fiber bundles followed by the generation of feature masks and their measurements. Additional details on the generation of the masks are provided in **Figure 4.**2 and Methods. (**B)** NMJs stained with S100B (Schwann cells; Green), NF/SV2 (Nerve; Cyan), bungarotoxin (AChR; Red), and DAPI (nucleus; Blue) in 2-month-old *S100GFP*-tg control and *S100GFP*-tg *Sod1*$^{-/-}$ mice. (**C, D)** Quantification of nerve terminal area, nerve terminal perimeter, AChR area, percentage overlap between AChR area and nerve terminal area, and tSC number and tSC area. (**E**) Overlap between nerve terminal and AChR and the % of denervated NMJs for muscles of *S100GFP*-tg and *S100GFP*-tg *Sod1*$^{-/-}$ mice from 1-3 months of age. (**F)** The 16 distinct morphological features from all NMJs (n = 563) across all recorded timepoints and genotypes were used to generate a UMAP visualization of the heterogeneity of NMJ structure. (**G**), UMAP displayed using k-means clustering and the percentage of clusters represented across all animal groups. (**H)** Radar plots indicating the NMJ features (n = 16) profiled across the four identified clusters. The innermost radius of the plot indicates a value of "0" representing the smallest relative mean value across all clusters, whereas the outermost cyan colored circle represents "1" - the maximum relative mean value for a specified feature. Values for all features across all NMJs analyzed are provided in **Figure 4.3**. (**I)** Representative NMJs in clusters 1-4. Open circles indicate average for each individual mouse of no fewer than 20 NMJs analyzed per muscle and bars represent means across animals ± SEM. *Denotes $p < 0.05$ vs *S100GFP*-tg *Sod1*$^{-/-}$ by two tailed unpaired t-test. Scale bar equals 25 μm and images constrained to the same dimensions.

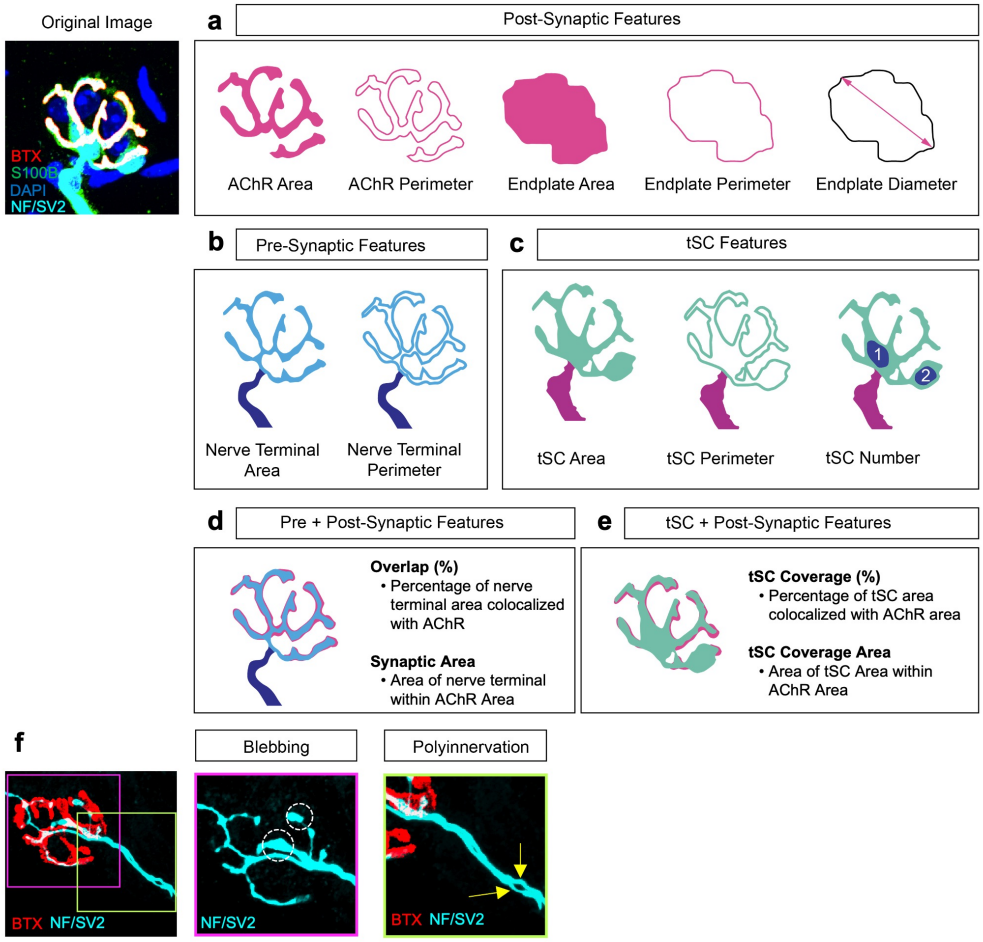

Figure 4.3: NMJ features analyzed. Binary masks were generated from the original image, and 16 en face NMJ morphological features were measured that represented the **(A),** post-synaptic (AChR and Endplate), **(B)**, pre-synaptic (nerve terminal, axonal blebbing, polyinnervation), and **(C)**, tSC structures. These pixel measurements are visualized by distinct colorations in each mask: red for post-synaptic features, light blue for pre-synaptic features, and green for tSC structures. **(D)**, In addition, the percentage "Overlap" between axon terminal and AChR areas were measured. This overlap was further quantified in terms of synaptic area (μm^2), denoting the area where the nerve terminal co-localizes with the AChR region. **(E)** Similarly, the "tSC coverage" was determined representing the tSC area that overlaps with the AChR region, and measured the "tSC Coverage Area," which is the expanse of tSC found within the AChR area. **(F)** The number of axon terminal blebs and and the presence of polyinnervation were also assessed for each NMJ.

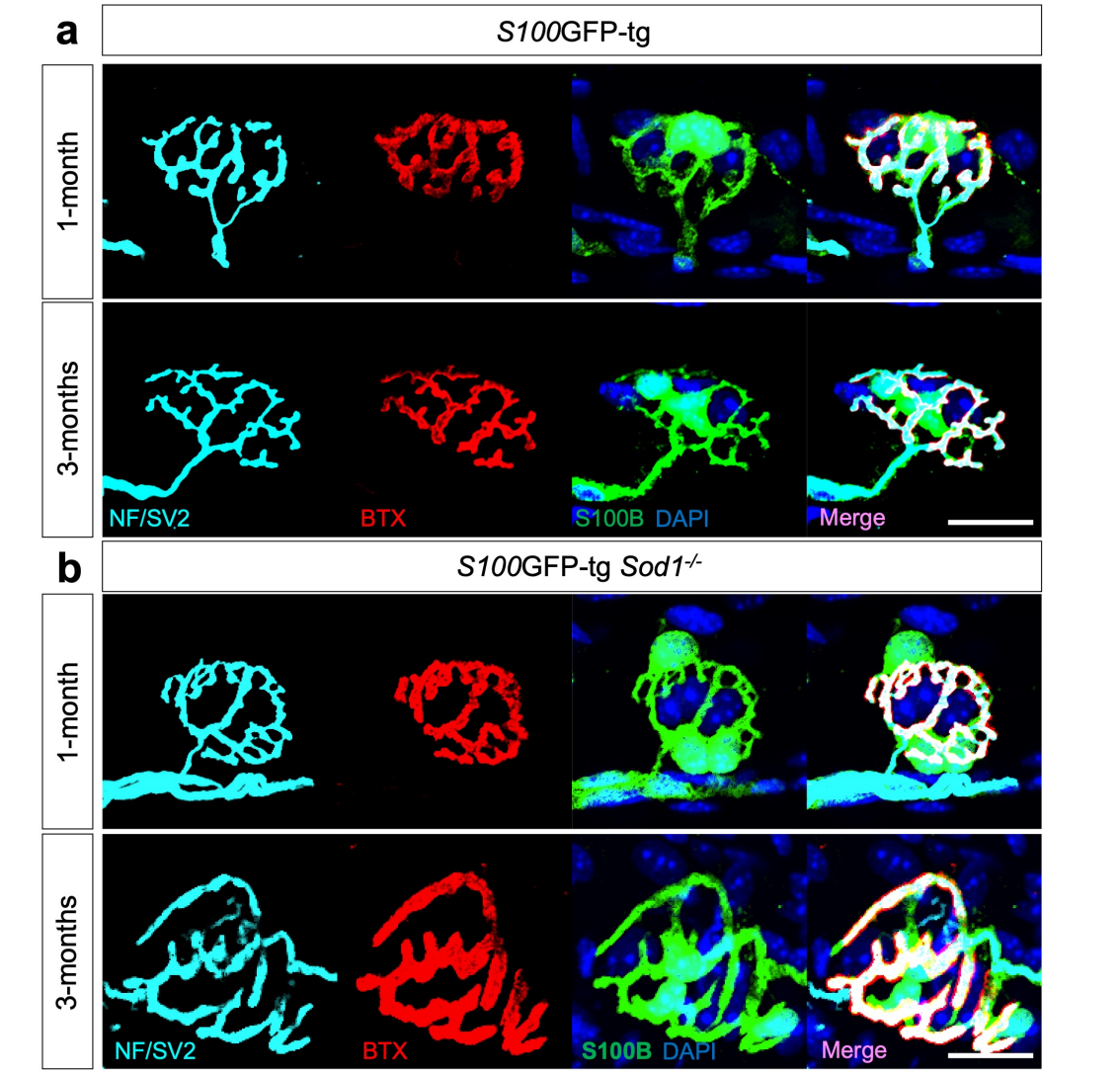
a
S100GFP-tg
1-month
3-months
NF/SV2
BTX
S100B DAPI
Merge
b
S100GFP-tg Sod1-/-
1-month
3-months
NF/SV2
BTX
S100B DAPI
Merge

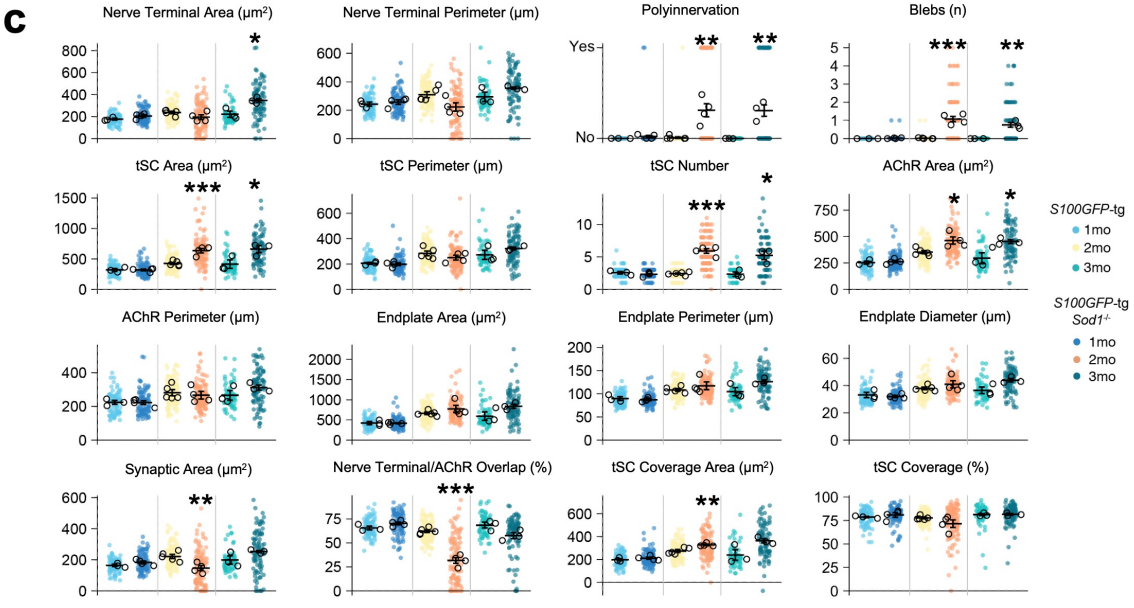
c
Nerve Terminal Area (µm²)
Nerve Terminal Perimeter (µm)
Polyinnervation
Yes
No
Blebs (n)
tSC Area (µm²)
tSC Perimeter (µm)
tSC Number
AChR Area (µm²)
AChR Perimeter (µm)
Endplate Area (µm²)
Endplate Perimeter (µm)
Endplate Diameter (µm)
Synaptic Area (µm²)
Nerve Terminal/AChR Overlap (%)
tSC Coverage Area (µm²)
tSC Coverage (%)
S100GFP-tg
1mo
2mo
3mo
S100GFP-tg Sod1-/-
1mo
2mo
3mo

Figure 4.4: Analysis of NMJ in *S100GFP*-tg and *S100GFP*-tg *Sod1*$^{-/-}$ mice. (A,B) Images of representative NMJs from 1- and 3-month-old mice, stained for S100B (indicating Schwann cells in Green), NF/SV2 (Nerve in Cyan), bungarotoxin (AChR in Red), and DAPI (Nucleus in Blue). **(A)** Shows NMJs from S100GFP-tg mice, while **B** are NMJs from *S100*GFP-tg *Sod1*$^{-/-}$ mice. **(C)** Graphical representation of NMJ features in *S100GFP*-tg and *S100GFP*-tg *Sod1*$^{-/-}$ mice aged 1, 2, and 3 months. Each colored dot represents a single NMJ. Black circles denote the average for all NMJs in an individual animal. The horizontal bars show the overall mean for each group, while error bars illustrate the mean ± SEM. *Denotes $p < 0.05$ *S100GFP*-tg vs *S100GFP*-tg *Sod1*$^{-/-}$ by two tailed unpaired t-test. Scale bar equals 25 µm and images constrained to the same dimensions.

Based on our findings that NMJs in 2-month-old *Sod1*$^{-/-}$ mice were characterized by higher numbers of tSCs than observed in other groups, we aimed to verify the presence of proliferation of *S100*GFP+ cells at the NMJs in these mice. To directly test this, we stained muscle bundles with an anti-Ki67 antibody (**Figure 4.5**). We found large numbers of Ki67+ nuclei in the fiber bundles from *Sod1*$^{-/-}$ mice compared to age matched WT mice. Moreover, the majority of Ki67+ nuclei originated from cells that were also *S100*GFP+ positive. Ki67+ cells were observed both in perisynaptic and extrasynaptic locations (within 50 microns of the nearest NMJ). These observations corroborate our earlier finding of a 3-fold increase in tSCs, in *Sod1*$^{-/-}$ mice at two months of age when compared to wild-type controls (**Figure 4.2D**).

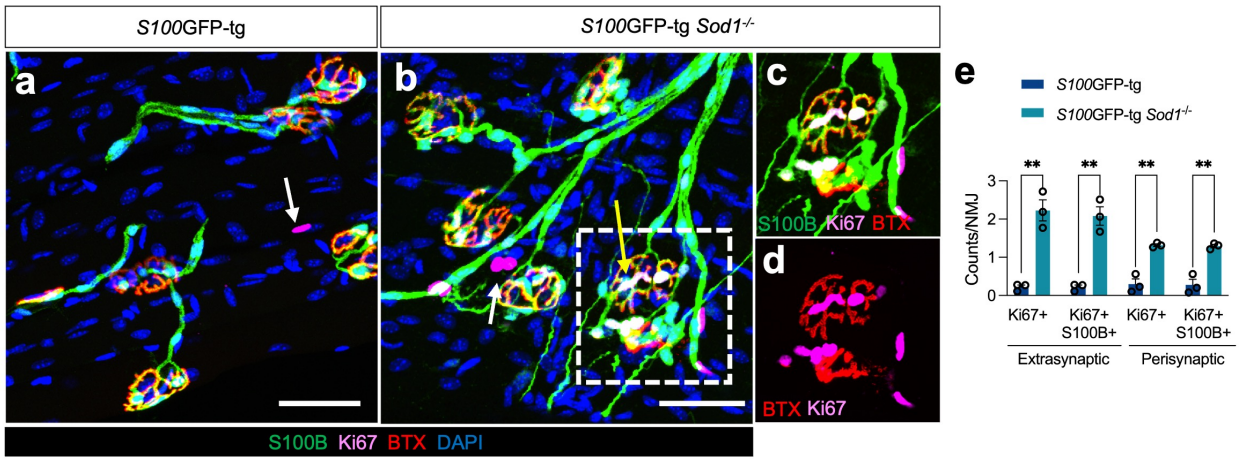

Figure 4.5: Enhanced proliferation of tSCs at the NMJ in 2-month-old *S100GFP*-tg *Sod1*$^{-/-}$ mice. Muscle fiber imaging from *S100GFP*-tg (**A**) and *S100GFP*-tg *Sod1*$^{-/-}$ (**B**) mice, immunostained for S100B (green), Ki67 (magenta), α-bungarotoxin (red), and DAPI (blue). White arrows point to extrasynaptic nuclei positive for Ki67 but lacking GFP, while the yellow arrow highlights a perisynaptic Ki67+GFP+ nucleus. **(C)** Enlarged view of two NMJs from the highlighted region in b, detailing the S100B, Ki67, and BTX stains. (**D**) The same NMJs from c, but focused on BTX and Ki67, revealing multiple Ki67+ nuclei in close proximity to the endplate. **(E)** Quantification of extraysnaptic and perisynaptic nuclei either singly labeled for Ki67 or double labeled for Ki67 and GFP. A minimum of 50 NMJs were used per animal. Open circles indicate average values for each individual mouse and bars show the means across animals ± SEM. **Denotes $p < 0.01$ vs *S100GFP*-tg *Sod1*$^{-/-}$ by two tailed unpaired t-test. Scale bars equals 50 μm.

Collectively, our functional and morphological data strongly support the existence of a key regenerative window centered around 2 months of age in *Sod1*$^{-/-}$mice that is ideal for studying the cellular and molecular changes in muscle Schwann cells during NMJ remodeling and reinnervation. We also present compelling evidence that this remodeling process includes, at least in part, the growth of Schwann cells located in the muscle at the NMJ and a promotion of increased synaptic area through nerve terminal growth. Thus, we next aimed to define the transcriptional response of muscle-resident Schwann cells during NMJ remodeling.

4.4.3 scRNA-Seq reveals a unique muscle-resident Schwann cell subtype

While the classification of Schwann cells has largely relied on histological examination and scRNA-Seq from nerve extracts[180], transcriptomic data on muscle-resident Schwann cells, especially tSCs, remain scant[181,182]. A particular challenge faced by these studies is the rarity of tSCs and the extensive tissue requirement, limiting the cell numbers previously analyzed to as few as 100 individual cells. To overcome this limitation and gain a thorough understanding of the transcriptomic changes in muscle-resident Schwann cells, as well as other cells in the muscle microenvironment during NMJ remodeling, we used scRNA-Seq on pooled TA and GTN muscles from both *S100GFP*-tg and *S100GFP*-tg *Sod1*$^{-/-}$ mice at 2 months of age (**Fig 4.6A**). After digesting the muscles, we sorted GFP+ PI- and GFP- PI- single cells using fluorescence-activated cell sorting (FACS) and then subjected the cells to droplet-based scRNA-Seq. Post sequencing and

quality control, we successfully isolated a rich population of both GFP+ and GFP- cells (**Figure 4.6B**). Our unbiased clustering approach using uniform manifold approximation and projection (UMAP) classified 15,256 cells [*S100GFP*-tg (n =5,260); *S100GFP*-tg *Sod1*$^{-/-}$ (n = 9,996)] into 11 non-Schwann cell clusters and 4 Schwann cell clusters including 2 myelin Schwann cell clusters and 2 terminal Schwann cell (tSC) clusters (**Fig 4.6C**). All the identified Schwann cell clusters displayed classic SC markers such as *S100b* and *Sox10*. Notably, clusters of myelin Schwann cells were marked by the expression of myelin-associated genes like *Mbp* and *Mpz* (**Figure 4.6D**), while tSC clusters presented the expression of recently reported non-myelin SC markers, *Ng2* and *Kir4.1* (**Figure 4.6D**)[181,183]. Additionally, tSC clusters prominently expressed the essential NMJ organizing gene, Agrn[147], the neurotrophic receptor gene, nerve growth factor receptor (Ngfr), and cyclin-D1 (Ccnd1) a recognized gene associated with Schwann cell proliferation (**Figure 4.6D**)[174]. Both *S100GFP*-tg and *S100GFP*-tg *Sod1*$^{-/-}$ samples displayed a comparable total number of Schwann cells (1,739 and 1,673, respectively).

Our data indicates the presence of at least two distinct tSC subgroups, which we termed tSC-A and tSC-B. Remarkably, we observed 8.5-fold greater representation of the tSC-B subgroup in *S100GFP*-tg *Sod1*$^{-/-}$ mice than in *S100GFP*-tg control mice accounting for 35.9% of the total SC population in *Sod1*$^{-/-}$ mice compared with just 4.3% for control mice (**Figure 4.6E**). In addition, the *S100GFP*-tg *Sod1*$^{-/-}$samples showed a lower percentage of myelin SCs (47.8%) when compared to the 78.8% in the control group. Both tSC clusters prominently displayed the previously identified tSC marker, Cd44[184], as well as the synaptic adhesion molecule, Cadm1. One significant observation was the robust expression in tSCs of Sox6, which is crucial for neurogenesis[185] and prevents early cell cycle exit in glial oligodendrocyte precursor cells[186] but is absent in adult mouse myelin SCs[187]. Within the tSC-B subgroup, we identified specific expression

of genes such as Pde10a, which is notably prevalent in the CNS[5], as well as Runx2 and Tnc, which were specific to tSC-B (**Figure 4.6F**) and have both recently been found at elevated levels in muscle-resident Schwann cells in Sod1G93A mice and in acutely denervated mouse muscles[182].

Pathway analysis revealed that genes upregulated in the tSC-B cluster, compared to the other muscle-resident Schwann cell types, were primarily involved in processes like synapse organization (*Gap43, Tnc, Sema3e, Negr1, Cadm1, Ntng1*), neuron projection extension (*Postn, Plxna4, Sema3e*), neuron migration (Adgrl3, Chl1, Ptpzr1) and extracellular matrix organizing processes (*Adamtsl1*, *Col27a1*, *Col5a2*, *Lgals3*) (**Figure 4.6G, Figure 4.7**). The tSC-B cluster also showed downregulated biological processes involved in myelination, myelin assembly and Schwann cell differentiation (**Figure 4.6H**). Overall, our findings delineate two distinct tSC subtypes, tSC-A and tSC-B, with the latter manifesting an enrichment in 2-month-old *Sod1*$^{-/-}$ mice and presenting a transcriptomic signature linked to cell adhesion, synapse organization, and axon regeneration. Based on these findings, we hypothesize that tSC-B is a critical sub-population of tSCs for successful NMJ reinnervation.

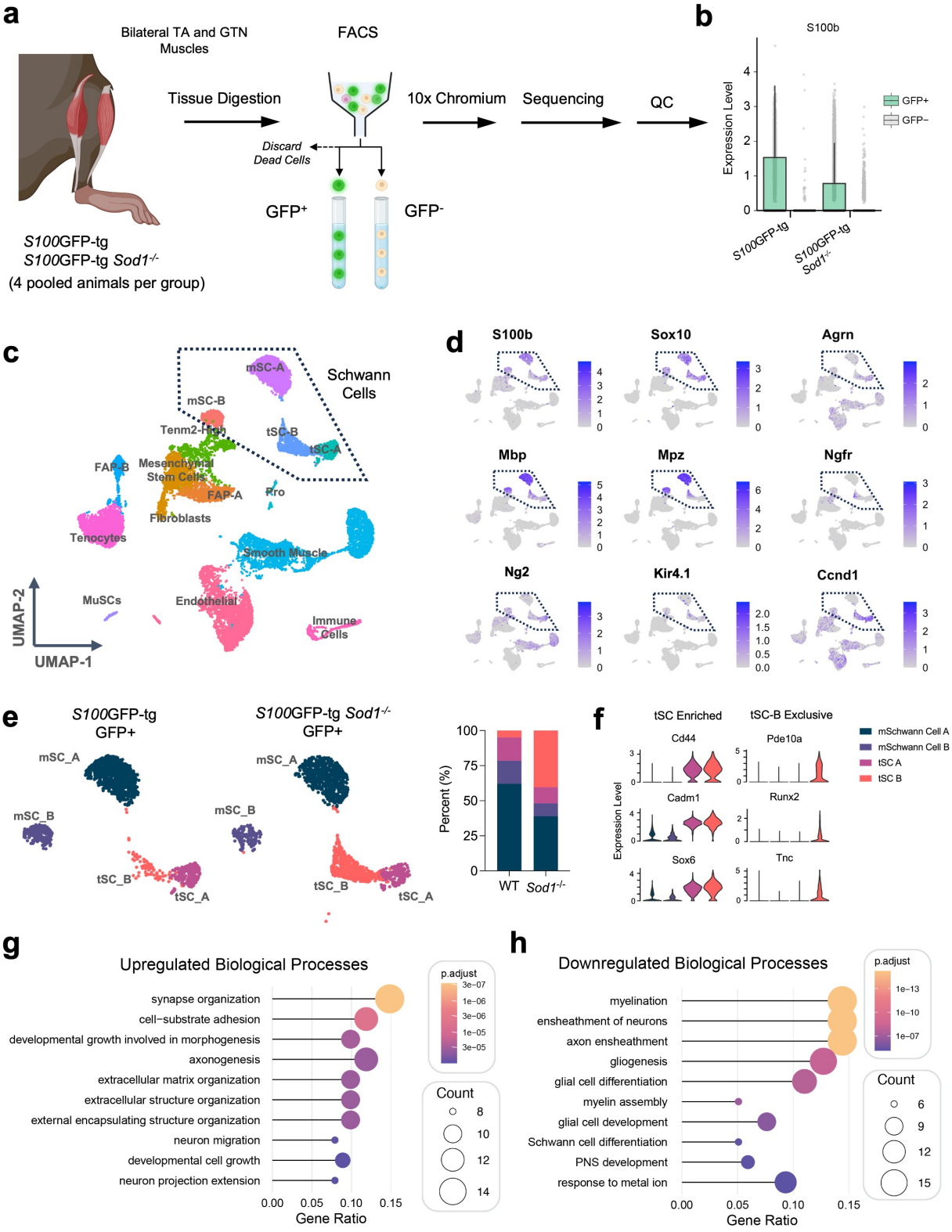
a
Bilateral TA and GTN Muscles
FACS
Tissue Digestion
10x Chromium
Sequencing
QC
Discard Dead Cells
GFP+
GFP-
S100GFP-tg
S100GFP-tg Sod1-/-
(4 pooled animals per group)
b
S100b
Expression Level
GFP+
GFP−
S100GFP-tg
S100GFP-tg Sod1-/-
c
Schwann Cells
mSC-A
mSC-B
tSC-B
tSC-A
Tenm2-High
FAP-B
Mesenchymal Stem Cells
FAP-A
Rro
Fibroblasts
Tenocytes
Smooth Muscle
MuSCs
Endothelial
Immune Cells
UMAP-2
UMAP-1
d
S100b
Sox10
Agrn
Mbp
Mpz
Ngfr
Ng2
Kir4.1
Ccnd1
e
S100GFP-tg GFP+
S100GFP-tg Sod1-/- GFP+
mSC_A
mSC_B
tSC_B
tSC_A
Percent (%)
WT
Sod1-/-
f
tSC Enriched
tSC-B Exclusive
mSchwann Cell A
mSchwann Cell B
tSC A
tSC B
Cd44
Pde10a
Cadm1
Runx2
Sox6
Tnc
Expression Level
g
Upregulated Biological Processes
synapse organization
cell−substrate adhesion
developmental growth involved in morphogenesis
axonogenesis
extracellular matrix organization
extracellular structure organization
external encapsulating structure organization
neuron migration
developmental cell growth
neuron projection extension
Gene Ratio
p.adjust
Count
h
Downregulated Biological Processes
myelination
ensheathment of neurons
axon ensheathment
gliogenesis
glial cell differentiation
myelin assembly
glial cell development
Schwann cell differentiation
PNS development
response to metal ion
Gene Ratio
p.adjust
Count

Figure 4.6: Identification of diverse muscle-resident Schwann cell subtypes via single cell RNA-Sequencing (scRNA-Seq). (A) Schematic outline of the experimental design: bilateral gastrocnemius (GTN) (n = 8) and tibialis anterior (TA) (n = 8) muscles were harvested from 2-month-old *S100GFP*-tg (n = 4) and *S100GFP*-tg *Sod1*$^{-/-}$ mice (n = 4), subjected to FACS to isolate live GFP+ and GFP- cells, followed by library preparation with 10X Chromium, scRNA-Seq, and quality control (QC). **(B)** S100b expression plot across GFP+ and GFP- groups. **(C)** UMAP reduction of resulting clusters. In total, 15 clusters were classified. Notably, four distinct clusters of muscle-resident Schwann cells were identified. **(D)** UMAP plots illustrating the transcript levels of markers for pan-Schwann cells (S100b, Sox10), myelin Schwann cells (Mbp, Mpz), terminal Schwann cells (Agrn, Ng2, Kir4.1), proliferation (Ccnd1), and a SC repair phenotype (Ngfr). **(E)** UMAP plot and quantification (%) of GFP+ muscle-resident Schwann cells. Cluster analysis determined two myelin Schwann cell clusters (mSC-A and mSC-B) and two tSC clusters (tSC-A and tSC-B). **(F)** Expression plots displaying markers highly expressed in tSCs (Cd44, Cadm1, Sox6) and exclusive to tSC-B (Pde10a, Runx2, Tnc). **(G)** Upregulated and **(H)** downregulated biological processes in tSC-B compared to tSC-A and myelin Schwann cells. Pathway descriptions correspond to gene ontology terms representing distinct biological processes.

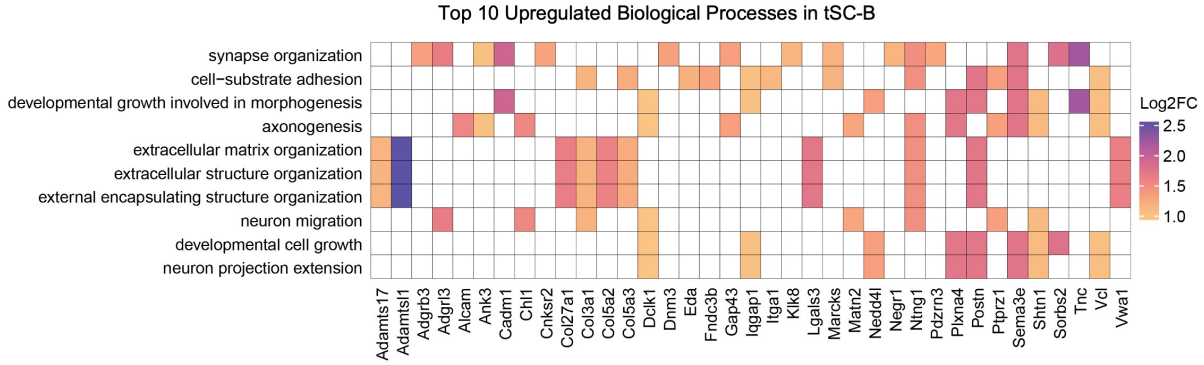

Figure 4.7: Genes involved in promoting synaptic function and regeneration are upregulated in tSC-B compared to tSC-A and myelin Schwann cells. Heatplot shows the top-10 gene ontology (GO) terms associated with genes upregulated in tSC-B compared to all other muscle-resident Schwann cells identified in this study.

4.5 Discussion

To our knowledge, the current study boasts the most detailed scRNA-Seq repository to date of muscle-resident Schwann cells, encompassing tSCs, across both healthy and partially denervated muscles. The results presented elucidate the critical role of a previously unrecognized reactive population of tSCs that has synapse promoting, cell adhesion, and ECM organizing properties. One prior study isolated tSCs using a dual mouse reporter that expressed both NG2-

dsRed and S100GFP and performed bulk-RNA Seq[181], but bulk sequencing doesn't allow for the distinction between different tSC subtypes or illuminate cell specific responses to NMJ remodeling.

The synaptic regenerative signature we identified in tSCs during their response to denervation is distinctly characterized by the expression of *Gap43* and *Ntng1*. GAP43 is noted for its concentrated presence within regenerating growth cones of neurons and plays an indispensable role in axon guidance[188]. The expression of GAP43 is not exclusive to neurons but is also found in reactive astrocytes and in tSCs after denervation, correlating with the elongation of tSC processes[189,190]. Beyond axonal guidance, GAP43 is also involved in the transfer of mitochondria between astrocytes and glioblastoma cells[191]. Given that mitochondria are abundant within growth cones to meet energy demands[192], one might speculate that *Gap43*+ tSCs promote axon regeneration through mitochondrial transfer, thereby contributing to metabolic support. This proposition opens new areas for exploring unconventional pathways of axon regeneration and delineating the multifaceted roles of GAP43 in neural repair mechanisms. Netrins are also important for axon guidance and has been shown to promote SC migration and proliferation[55,193]. Recently, NTNG1 was discerned to facilitate signaling interactions between tSCs and sensory neurons, crucial for organogenesis in both hairy and non-hairy skin[194]. The expression of *Ntn1g* in muscle-resident tSCs could function to support reinnervation of the endplate after denervation. Collectively, the expression of synaptic related genes in tSCs highlights the potential for new therapeutic targets to promote NMJ repair.

Cellular proliferation is universally recognized as a fundamental mechanism in various tissue regeneration processes. The proliferation dynamics of myelin Schwann cells have been extensively studied, with nerve injuries recognized as their primary trigger. A pertinent example

is the marked 3 to 4-fold elevation in Schwann cell numbers observed within a week of sciatic nerve injury[140]. Although inhibition of Cyclin D1 mediated Schwann cell proliferation was ineffective in preventing nerve regeneration in the distal sciatic nerve stump[195], that study did not examine muscle-resident Schwann cells nor perform any functional assessment of NMJ transmission. tSCs not only proliferate after nerve injury but also extend cytoplasmic processes, promoting axonal sprouting, although the cellular signals remain under studied[43,44]. Further highlighting the importance of tSCs for nerve regeneration, a recent study used an anti-GD3 antibody to selectively eliminate tSCs after a peroneal nerve injury. The result was a reduction in the number of tSCs, decreased muscle reinnervation, and impaired functional recovery[152]. Our study significantly expands on these previous studies by providing novel understanding of the role of SPP1 -signaling acting on Schwann cells near the NMJ and its importance for the regeneration of NMJs.

Our research further highlights the *Sod1*$^{-/-}$ mice as a useful model for understanding NMJ repair processes and tSC responses during the remodeling of innervation. In support of this contention are our observations during the remodeling phase, of key characteristics reminiscent of NMJ regeneration, such as increased AChR area, tSC proliferation[43], polyinnervation[196], and axonal blebbing[53]. Unlike nerve injury, which denervates every muscle fiber leading to a lack of NMJ structural diversity, young *Sod1*$^{-/-}$ mice recapitulate what we postulate to be a more faithful representation of heterogeneous NMJ remodeling in the context of normal aging and/or degenerative neuromuscular diseases. Recognizing the potency of this model for investigating NMJ diversity and the response of muscle-resident Schwann cells to denervation propelled our decision to perform single-cell RNA sequencing (scRNA-Seq) of muscle niche cells, emphasizing GFP+ Schwann cells, which identified two distinct subtypes each for myelin Schwann cells and

tSCs. A particular tSC subtype demonstrated traits related to ECM organization and synapse promotion and was considerably enriched in the *Sod1*$^{-/-}$ muscles at 2-months of age, supporting their important role in NMJ regeneration.

Overall, our research deepens the existing knowledge on the intricate cellular processes of NMJ regeneration orchestrated by Schwann cells. These insights not only expand our understanding of neuromuscular biology but also present promising avenues for targeted therapeutic strategies. Such innovations hold the potential to revolutionize the treatment landscape for debilitating neuromuscular disorders, including ALS and sarcopenia.

Chapter 5 SPP1 Signaling Is Critical for Muscle Reinnervation

5.1 Abstract

Understanding the cellular mechanisms underlying neuromuscular junction (NMJ) reinnervation is vital for addressing muscle denervation associated with nerve injury. This chapter delves into the role of muscle-resident Schwann cells, focusing on secreted phosphoprotein 1 (SPP1) signaling dynamics between myelin-producing Schwann cells and terminal Schwann cells (tSCs) in *Sod1*$^{-/-}$ mice. We employed an intercellular communication network analysis using a subset of cells from our single-cell RNA sequencing (scRNA-Seq) dataset described in Chapter 4 and performed targeted RT-qPCR to examine gene expression within the SPP1 pathway. Histological analyses using fluorescently labeled antibodies further validated protein localizations. Additionally, acute recoverable nerve injury models in mice were used to investigate the temporal dynamics of SPP1 gene expression post-injury and its influence on muscle reinnervation. Our analysis revealed a marked induction of SPP1 signaling in *S100GFP*-tg *Sod1*$^{-/-}$ mice, notably in myelin Schwann cells, with significant communication with tSCs. This novel signaling mechanism was implicated in enhancing tSC proliferation and survival during muscle denervation, important for successful NMJ remodeling and reinnervation. Post-nerve injury analyses showed a striking elevation in *Spp1* expression and its receptors, peaking shortly after injury and normalizing as reinnervation progressed. Intriguingly, inhibition of Spp1 signaling through neutralizing antibody administration resulted in reduced muscle reinnervation efficiency and a decrease in tSC numbers at the NMJ. This study uncovers a novel SPP1-driven intercellular communication between myelin

Schwann cells and tSCs, playing a pivotal role in the NMJ reinnervation process. The pronounced expression of Spp1 during early nerve regeneration stages and its subsequent normalization aligns with muscle reinnervation milestones, suggesting SPP1 signaling is crucial for efficient muscle reinnervation. Furthermore, the impairment of muscle reinnervation upon SPP1 signaling inhibition highlights its potential as a therapeutic target in neuromuscular recovery post-injury. These findings provide significant insights into the molecular interactions that facilitate NMJ repair and underscore the potential of targeting SPP1 pathways in therapeutic strategies for neuromuscular regeneration.

5.2 Introduction

Neuromuscular junctions (NMJs) serve as critical communication hubs between motor neurons and muscle fibers, orchestrating muscle contraction and voluntary movement. The integrity and efficient reinnervation of NMJs are fundamental to maintaining muscle function, particularly following nerve injuries. Recent studies have increasingly focused on the cellular mechanisms underlying NMJ repair, with Schwann cells emerging as key players in this process. These glial cells, especially those residing in muscles, have shown remarkable adaptability and functionality in response to neuromuscular damage, making them a focal point of research in neuromuscular regeneration[182].

Schwann cells can be broadly categorized into myelinating and non-myelinating types, with terminal Schwann cells (tSCs) representing a specialized subset of the latter group[44,151]. These cells are known for their role in synaptic maintenance and the facilitation of NMJ recovery post-injury [40,42]. Schwann cells respond dynamically to nerve damage, undergoing phenotypic changes that enable them to support axonal regrowth and remyelination[69,78,79,81]. This adaptability is partly

attributed to their ability to engage in complex intercellular communication, particularly through secretory pathways[197–199].

Secreted phosphoprotein 1 (SPP1), commonly known as osteopontin, has emerged as a significant player in the field of cellular signaling, particularly within the context of skeletal muscle health and disease[199]. SPP1 plays a critical role in macrophage physiology, especially in conditions such as muscular dystrophy. Studies have shown that SPP1 is upregulated in dystrophic muscles, contributing to the inflammatory environment characteristic of these conditions. For instance, in patients with Duchenne Muscular Dystrophy (DMD), elevated levels of SPP1 have been correlated with disease severity and progression[200], primarily due to its role in recruiting and activating macrophages that exacerbate muscle damage through inflammatory pathways[201]. In muscular dystrophies, macrophages infiltrate muscle tissue in response to injury, where SPP1 signaling influences their phenotype, switching them from a regenerative, anti-inflammatory state to a pro-inflammatory one[201–203]. This switch exacerbates muscle damage, fibrosis, and impairs regeneration. Despite the considerable focus on SPP1 in the context of muscular dystrophy and macrophage function, its specific signaling dynamics with Schwann cells, particularly in nerve repair, is less explored. The limited data in this area highlight a significant gap in our understanding of SPP1 signaling in neuromuscular health.

This study aims to elucidate the role of SPP1 in the NMJ regeneration process, particularly focusing on its signaling between myelin-producing Schwann cells and tSCs in the *Sod1*$^{-/-}$ mouse model. Leveraging our scRNA-Seq dataset, we investigate the gene expression profiles and protein localizations associated with SPP1 signaling in healthy and partially denervated skeletal muscles. Furthermore, we utilize acute recoverable nerve injury models in mice to examine the temporal

dynamics of SPP1 expression and its impact on muscle reinnervation following injury. Our findings uncover a novel intercellular communication mechanism mediated by SPP1 signaling, significantly enhancing tSC proliferation and survival during muscle denervation. This mechanism is critical for successful NMJ remodeling and reinnervation. Our study not only provides new insights into the molecular interactions critical for NMJ repair but also highlights the therapeutic potential of targeting SPP1 signaling in neuromuscular regeneration strategies.

5.3 Methods

5.3.1 Nerve injuries and neutralization of intramuscular Spp1

Male C57BL/6J mice, aged between 10 - 16 weeks, were subjected to bilateral sciatic or peroneal nerve crush to induce muscle denervation in both legs. Forceps were employed to produce the crush. Mice assigned to sciatic nerve injury protocols had tissues harvested at intervals of 0, 7, 14, or 28 days following the injury. For those undergoing peroneal nerve injury, a 10 μL intramuscular injection of Spp1 neutralizing antibody (4 μg, AF808, R&D Systems) was administered into the tibialis anterior (TA) muscles, utilizing a Hamilton syringe. This injection routine was repeated every two days post the initial injury. Control mice received saline injections concurrent with the day of injury and repeated every two days thereafter. Seven days post injury (DPI), all mice were anesthetized and TA muscles were assessed for contractile functionality and collected for NMJ imaging.

5.3.2 In situ Force Testing

Mice were anesthetized with initial intraperitoneal injections of Avertin (tribromoethanol, 250 mg/kg) with supplemental injections to maintain an adequate level of anesthesia during all procedures. Gastrocnemius (GTN) or tibialis anterior (TA) muscle contractile properties were

measured in situ, as described by Larkin et al. (2011)[161]. In anesthetized mice, the whole GTN or TA muscle was isolated from surrounding muscle and connective tissue using great care not to damage the nerve and/or blood vessels during the dissection. A 4-0 silk suture was tied around the distal tendon and the tendon was severed. The animal was then placed on a temperature-controlled platform warmed to maintain body temperature at 37°C. The hindlimb was secures to the platform, and the tendon was tied to the lever arm of a servomotor (model 6650LR, Cambridge Technology). A continual drip of saline warmed to 37°C was administered to the muscles to maintain temperature. Muscles were activated either by stimulation of the tibial (GTN muscle) or common peroneal (TA muscle) nerve using a bipolar platinum wire electrode or by direct stimulation of the muscle via cuff electrodes wrapped around the proximal and distal ends of the muscle. Custom-designed software (LabVIEW 2018; National Instruments, Austin, TX) controlled electrical pulse properties and servomotor activity and recorded data from the force transducer. The voltage of 0.2 ms stimulus pulses was increased, and optimal muscle length (Lo) was subsequently adjusted, to give maximum twitch force. The Lo was measured with digital calipers. Muscles were held at Lo and subjected to 300 ms trains of pulses with increase stimulation frequencies maximum isometric force (Po) was achieved. Previously established Lf-to-Lo ratios of 0.6 for TA muscles were used to calculate Lf for each muscle. The physiological cross-sectional area (CSA) of muscles was determined by dividing the mass of the muscle by the product of Lf and 1.06 g/cm3, the density of mammalian skeletal muscle[162]. Po was normalized by the CSA to calculate specific Po (sPo), as a measure of intrinsic force generating capacity. Functional innervation was assessed by calculating the ratio of force production in response to nerve stimulation relative to the force elicited by direct muscle stimulation. A value of 1.0 indicates high fidelity of the nerve-muscle

functional connections, while the extent to which the ratio is less than 1.0 provides an indication of the fraction of muscle fibers that are unable to respond to nerve stimulation.

5.3.3 NMJ Feature Quantification

Fiji software was used for quantitative analysis of confocal micrographs. All analyses were performed on maximum intensity projections using guidelines described in detail in the NMJ-Morph image processing pipeline.[163] The obtained images were preserved as nd2 Nikon files and subsequently imported into ImageJ software, with channels consolidated into a single tiff image prior to their separation for individual component analysis. Initial preparations involved the division and cropping of images to ensure each contained a singular NMJ, enabling individual analysis of each NMJ. The analysis was constrained to en-face NMJs only.

For each channel, a threshold was set using the thresholding tool to produce a binary mask that most closely resembled the real image of the NMJ component being analyzed. The binary mask was selected and measured to provide the area and perimeter of the selected channel. The endplate mask was generated by applying the 'Create background' FIJI tool on the AChR mask, which completely fills in the AChR mask. Endplate area and diameter were also measured. This process was repeated for every NMJ image, for each of the NMJ components.

The 'Overlap' and 'SC Coverage' measurements were derived in accordance to NMJ-Morph guidelines. Briefly, the following calculations were used:

$$Overlap, SC\ Coverage = \left[\frac{AchR\ Area - unoccupied\ area\ of\ AChR}{AChR\ Area}\right] \times 100$$

$$Synaptic, SC\ Coverage\ Area\ =\ AchR\ Area - unnocupied\ area\ of\ AChR$$

The unoccupied area denotes regions lacking colocalization with α-BTX. Following the generation of a binary mask for calculating the AChR, nerve terminal, and tSC areas, the masks were processed, inverted as needed, and merged to measure unoccupied areas of AChR. Beyond structural area measurements, attention was given to NMJs manifesting visible polyinnervation—characterized by the convergence of at least two axons onto a single NMJ.

5.3.4 Whole-tissue RNA extraction and RT-qPCR Analysis

GTN and TA muscle samples were homogenized in TRIzol reagent (Invitrogen, Thermo Fisher Scientific) using a bead mill. RNA was isolated by phenol/chloroform extraction and RNA yield was determined using a NanoDrop Spectrophotometer (NanoDrop 2000c, Thermo Fisher Scientific). Genomic DNA was removed by incubation with DNase I (Ambion, Thermo Fisher Scientific, AM2222) followed by its heat inactivation. Total RNA (1 μg) was reverse-transcribed to cDNA using SuperScript III Master Mix, Random Hexamers, and dNTPs (Invitrogen, Thermo Fisher Scientific) and RT-qPCR performed on a CFX96 Real-Time PCR Detection System (Bio-Rad, 1855195) in triplicate 20 μL reactions of iTaq Universal SYBR Green Supermix (Bio-Rad, 1725124) with 1 μM forward and reverse primer. Relative mRNA expression was determined using the $2^{-\Delta\Delta CT}$ method with Gapdh serving as a control for the samples. Primer sequences used in this study can be found in **Table 5.1**.

Table 5.1: Primers used for RT-qPCR

Name	Sequence

Spp1 (Fwd)	AGCAAGAAACTCTTCCAAGCAA
Spp1 (Rev)	GTGAGATTCGTCAGATTCATCCG
Cd44-pan (F)	TCGATTTGAATGTAACCTGCCG
Cd44-pan (R)	CAGTCCGGGAGATACTGTAGC
Cd44v6 (Fwd)	GGCCACCACACAGAGTCATT
Cd44v6(Rev)	CGCCGCTCTTAGTGCTAGAT
Tgf-β1 (Fwd)	CTGCTGACCCCCACTGATAC
Tgf-β1 (Rev)	AGCCCTGTATTCCGTCTCCT
Tgfbr2 (Fwd)	AGCGGGGAATTTACAGAATG
Tgfbr2 (Rev)	GAGGAATGACAGCGATGCTA
Ccnd1 (Fwd)	AGACCATTCCCTTGACTGC
Ccnd1 (Rev)	AAGCAGTTCCATTTGCAGC
Ngfr (Fwd)	TGCCTGGACAGTGTTACGTT
Ngfr (Rev)	ACAGGGAGCGGACATACTCT
Gdnf (Fwd)	CCAGTGACTCCAATATGCCTG
Gdnf (Rev)	CTCTGCGACCTTTCCCTCTG
Gapdh (Fwd)	CACCATCTTCCAGGAGCGAG
Gapdh (Rev)	CCTTCTCCATGGTGGTGAAGAC

5.3.5 Statistical analysis

Data are presented as the mean ± SEM**.** All statistical analyses were performed using GraphPad Prism 8 (GraphPad Software) and *R*. Between-group differences were tested by two-tailed unpaired students t-tests (2 groups) or by a one-way analysis of variance (ANOVA) followed by Dunnett's multiple comparisons test. A two-way ANOVA followed by Tukey's multiple comparison's test was executed when two factors were involved. Differences were considered to be statistically significant at the $P < 0.05$ level (*p < 0.05, **p<0.01, ***p < 0.001, ns: not significant).

5.4 Results

5.4.1 Intercellular communication network analysis reveals a novel SPP1 signaling dynamic between myelin SCs and terminal SCs

To elucidate the interactions between muscle-resident Schwann cells and other cells within the skeletal muscle niche during the robust NMJ remodeling event identified in young *Sod1*$^{-/-}$ mice, we performed an intercellular communication network analysis on a subset of cells from our scRNA-Seq dataset, described in Chapter 4, using CellChat[168]. Information flow for secreted signaling pathways was performed to identify signaling pathways that are changed in *S100GFP*-tg *Sod1*$^{-/-}$ muscles relative to control. We observed that Growth Arrest Specific (GAS) signaling, a crucial regulator of proliferation inhibition, was predominantly expressed in myelin SCs of *S100GFP*-tg compared to *S100GFP*-tg *Sod1*$^{-/-}$ mice (**Figure 5.1-2**). GAS incoming signaling pattern was found to be low in the proliferating cell and tSC-B cell clusters (**Figure 5.1A**). Interestingly, the PERIOSTIN and SPP1 signaling network displayed an information flow magnitude that was amplified by 40-fold in the *S100GFP*-tg *Sod1*$^{-/-}$ group relative to the *S100GFP*-tg group (**Figure 5.1A**). Both periostin and SPP1 signaling have been implicated in promoting tumor cell growth and are also known to be upregulated following nerve injury.

Our finding of marked induction of SPP1 signaling in *S100GFP*-tg *Sod1*$^{-/-}$ mice is compelling in light of a recent study finding that SPP1 promotes Schwann cell proliferation and survival, and its expression is notably upregulated in myelin Schwann cells following human peripheral nerve injury[198]. Exploring SPP1 signaling in our dataset, we identified a predominant expression of Spp1 in myelin SCs (**Figure 5.1B,C**). While SPP1 appears to communicate with almost every cell type, a marked increase in inferred SPP1 signaling was observed in *Sod1*$^{-/-}$ mice (Fig 5c). Moreover, heightened incoming signals were predicted in tSC-B cells, alongside other cells, including mesenchymal stem cells and proliferative cells (**Figure 5.1C**, **Figure 5.2B**). Notably, a significant communication probability was observed between myelin Schwann cells,

mainly mSC-A, and tSCs in *Sod1*$^{-/-}$ mice, facilitated through Spp1-Cd44 and Spp1-(Itgav-Itgab1) signaling (**Fig 5.1D**).

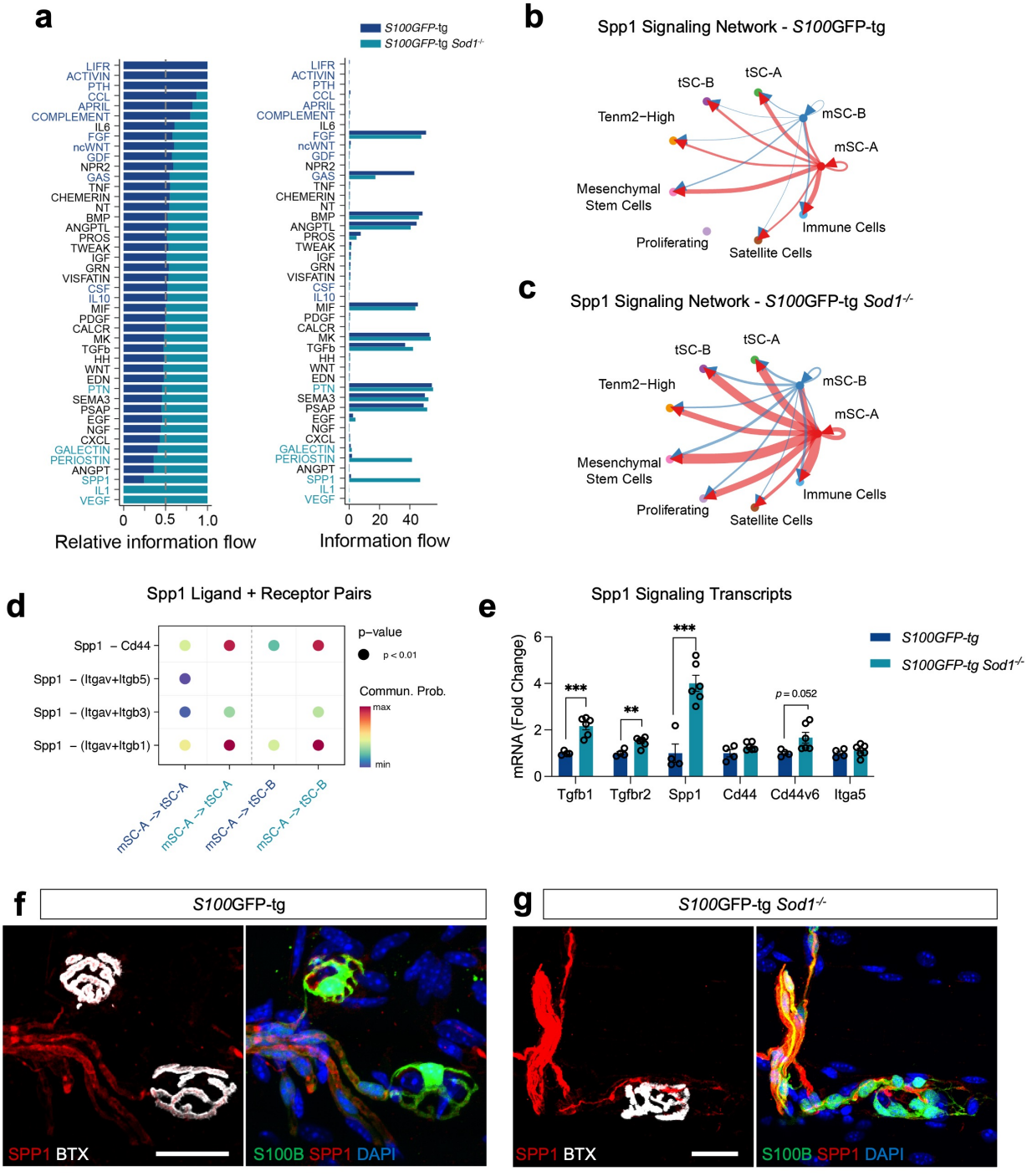

Figure 5.1: Intercellular communication infers an SPP1 signaling dynamic between mSC and tSC. a, Secreted signaling pathways enriched in the muscle-resident SC network in *S100GFP*-tg and *S100GFP*-tg *Sod1*$^{-/-}$ mice. Dashed line through the middle on the 'Relative Information Flow' plot represents equal probability that a signaling pathway is active in both groups. Deviations away from the dashed line indicate greater information flow for a specific group. Information flow plot shows the strength of a specific signaling pathway in the overall signaling landscape **b, c,** Circle plots displaying the SPP1 signaling network across cell clusters for (**b**) *S100GFP*-tg and (**c**) *S100GFP*-tg *Sod1*$^{-/-}$ mice. The thickness of connecting lines represents the communication likelihood between paired cell clusters, with arrowheads demarcating communication directionality. **d,** Dotplot visualizing signaling of the Spp1 ligand to Cd44 and integrin receptors, denoting interactions between a distinct population of mSCs (mSC-A) and tSCs (tSC-A and tSC-B) in both *S100GFP*-tg (blue) and *S100GFP*-tg *Sod1*$^{-/-}$ (teal) mice. **e**, mRNA levels determined by qPCR for several presumed components of the Spp1 signaling pathway for muscles of *S100GFP*-tg (n = 4) and *S100GFP*-tg *Sod1*$^{-/-}$ (n = 6) mice. **f,g**, Representative immunofluorescent images of NMJs stained with Spp1 (Red), S100B (Green), BTX (White), and DAPI (Blue). Open circles indicate values for individual mice and bars represent the mean across animals ± SEM **P ≤ 0.01, ***P ≤ 0.001, *S100GFP*-tg vs *S100GFP*-tg *Sod1*$^{-/-}$ by two tailed unpaired t-test. Scale bars represent 25 μm.

To validate our CellChat findings, we performed targeted RT-qPCR to evaluate the expression levels of key genes within the SPP1 pathway in GTN muscles isolated from 2-month-old *S100GFP*-tg and *S100GFP*-tg *Sod1*$^{-/-}$ mice (**Figure 5.1E**). We showed upregulation in the expression of Tgfb1, Tgfbr2, and Spp1 in *Sod1*$^{-/-}$ mice. While Cd44 levels remained unchanged, we detected a borderline significant elevation in Cd44v6 ($p = 0.052$), the specific receptor variant of Cd44 known to bind SPP1. We next sought to confirm our scRNA-Seq and bioinformatic findings by pinpointing the protein localization of SPP1 in muscle fibers. Histological analysis using an Spp1 antibody on fixed muscle fiber bundles revealed pronounced localization of Spp1 in myelin SCs near the NMJ, with intensified staining observed in *Sod1*$^{-/-}$ mice (**Figure 5.1G**) compared to control (**Figure 5.1G**). In addition, we validated the protein localization of CD44 in tSCs (**Figure 5.2C**). Taken together, our findings illuminate a novel Spp1 signaling mechanism involving both myelin SCs and tSCs, which could play a role in enhancing the tSC proliferation and survival during muscle denervation important for successful NMJ remodeling and reinnervation.

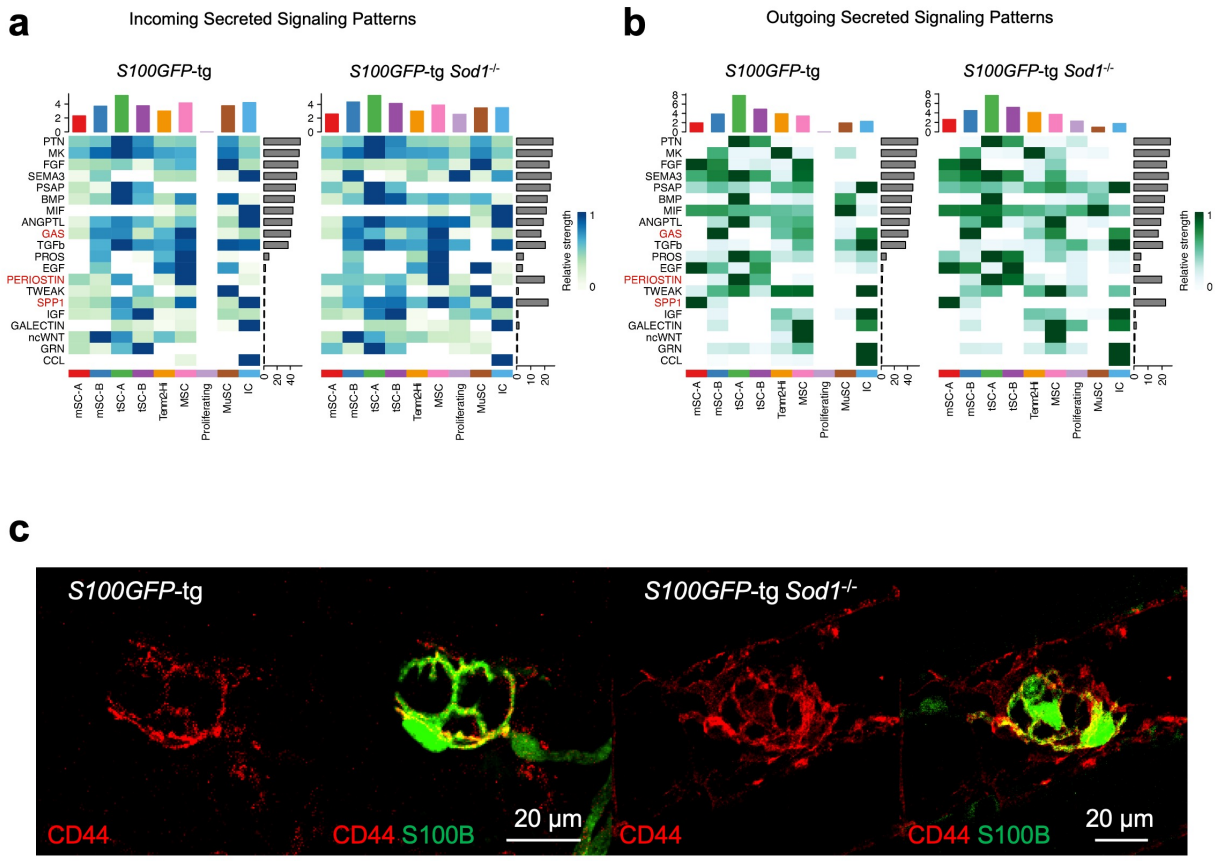

Figure 5.2: Top 20 intercellular secreted signaling pathways and validation of CD44 protein localization. a, Incoming and **(b)** outgoing secreted signaling patterns in 2-month-old *S100GFP*-tg *Sod1*$^{-/-}$. Rows delineate distinct signaling pathways, while columns indicate individual cell clusters. Intensity of heatmap color signifies relative signaling strength: darker hues indicate higher signaling strength, and lighter ones suggest weaker signaling. Pathways designated with a red font highlight those most dysregulated in Sod1-/- relative to control. mSC, myelin Schwann cells; tSC, terminal Schwann cells; MSC, mesenchymal stem cells; MuSC, muscle stem cells; IC, immune cells. **c,** Representative immunofluorescent images of NMJs stained for CD44 (Red) and S100B (Green).

5.4.2 SPP1 gene expression is markedly increased in muscles following nerve injury

To explore whether an acute recoverable nerve injury alters the gene expression dynamics of SPP1 signaling in skeletal muscle, we performed sciatic nerve crush procedures on 2-month-old C57BL/6 mice (**Figure 5.3A**). Subsequently, we assessed transcript levels of denervation response pathways and genes involved in SPP1 signaling in GTN muscles in naïve non-injured controls, and 7-, 14-, and 28-days post injury (DPI). We observed a striking elevation in Spp1

expression, and its receptors Cd44 and Itgav, peaking at 7 DPI and subsequently reverting to baseline levels by 14 DPI (**Fig 5.3B**). This temporal trend closely parallels the known post nerve injury gene expression pattern of Chrna1[158], suggesting an inverse relationship with muscle innervation. In addition, Tgfb1 and its receptor Tgfbr2, proposed to be upstream of SPP1 signaling were also elevated at 7 DPI, with Tgfbr2 expression being reduced at 28 DPI compared to uninjured controls. Gene expression for NGFR and GDNF, which are associated with Schwann cell mediated nerve regeneration, were also highly expressed at 7 DPI, while the cell proliferation gene, Ccnd1, was elevated at 7 DPI and persisted at high levels out to 14 DPI. Protein localization of Spp1 was also validated using immunofluorescent imaging of muscle fiber bundles, which showed SPP1 localized to myelin Schwann cells, as well as other GFP+ cells and GFP- cells (**Figure 5.4**). The pronounced Spp1 expression during the initial nerve regeneration phase and its subsequent normalization is consistent with known muscle reinnervation milestones and implicates the potential involvement of Spp1 in muscle reinnervation.

5.4.3 Inhibition of muscle Spp1 after acute nerve injury results in reduced muscle reinnervation and fewer tSCs

To determine the role of Spp1 signaling in muscle reinnervation and its potential mediation of tSC responses post-nerve injury, we carried out peroneal nerve crush injuries on control *S100GFP*-tg mice and administered intramuscular injections of either an SPP1 neutralizing antibody (Spp1-nAb) or saline (**Figure 6.3C**). Evaluations of recovery of functional neurotransmission as assessed by the ability of nerve stimulation to activate muscle contractions and tSC characteristics were conducted at 7 DPI. To expedite the evaluation of the onset of muscle reinnervation and reduce the number of muscle injections, nerve injuries were strategically performed near the nerve entry point of the TA muscle, with muscles receiving injections at the

time of injury and every two days thereafter. Evoked force measurements by direct muscle stimulation showed no difference between the saline- and Spp1-nAb-treated groups; however, nerve evoked muscle forces were 43% lower for muscles of mice treated with Spp1-nAb (**Figure 5.3D**). Furthermore, nerve-to-muscle force ratios in Spp1-nAb administered mice were 38% lower than for muscles of saline-treated mice. Collectively, these findings suggest that functional reinnervation post-injury was either impaired or delayed by neutralizing intramuscular Spp1 signaling.

We concurrently evaluated the effects of intramuscular SPP1 neutralization on tSCs in fixed muscle fiber bundles following injury histologically (**Figure 5.3E**). Mice treated with Spp1-nAb at 7 DPI displayed a pronounced decrease in the nerve terminal area, perimeter, and synaptic area in comparison to the saline-treated controls (**Figure 5.3F**). In terms of denervated NMJs, the Spp1-nAb-treated group exhibited a significantly higher proportion of denervated muscle fibers relative to the saline-treated group (67% Spp1-nAb vs 33% saline), and NMJ synaptic area was also lower in Spp1-nAb mice. Further examination of tSC characteristics revealed a diminished number of tSCs per NMJ and a smaller tSC area for muscles that had SPP1 signaling inhibited (**Fig 5.3F**). Taken together, this evidence, coupled with our functional analyses, underscores the role of Spp1 in muscle reinnervation and its involvement in augmenting the tSC count at the NMJ.

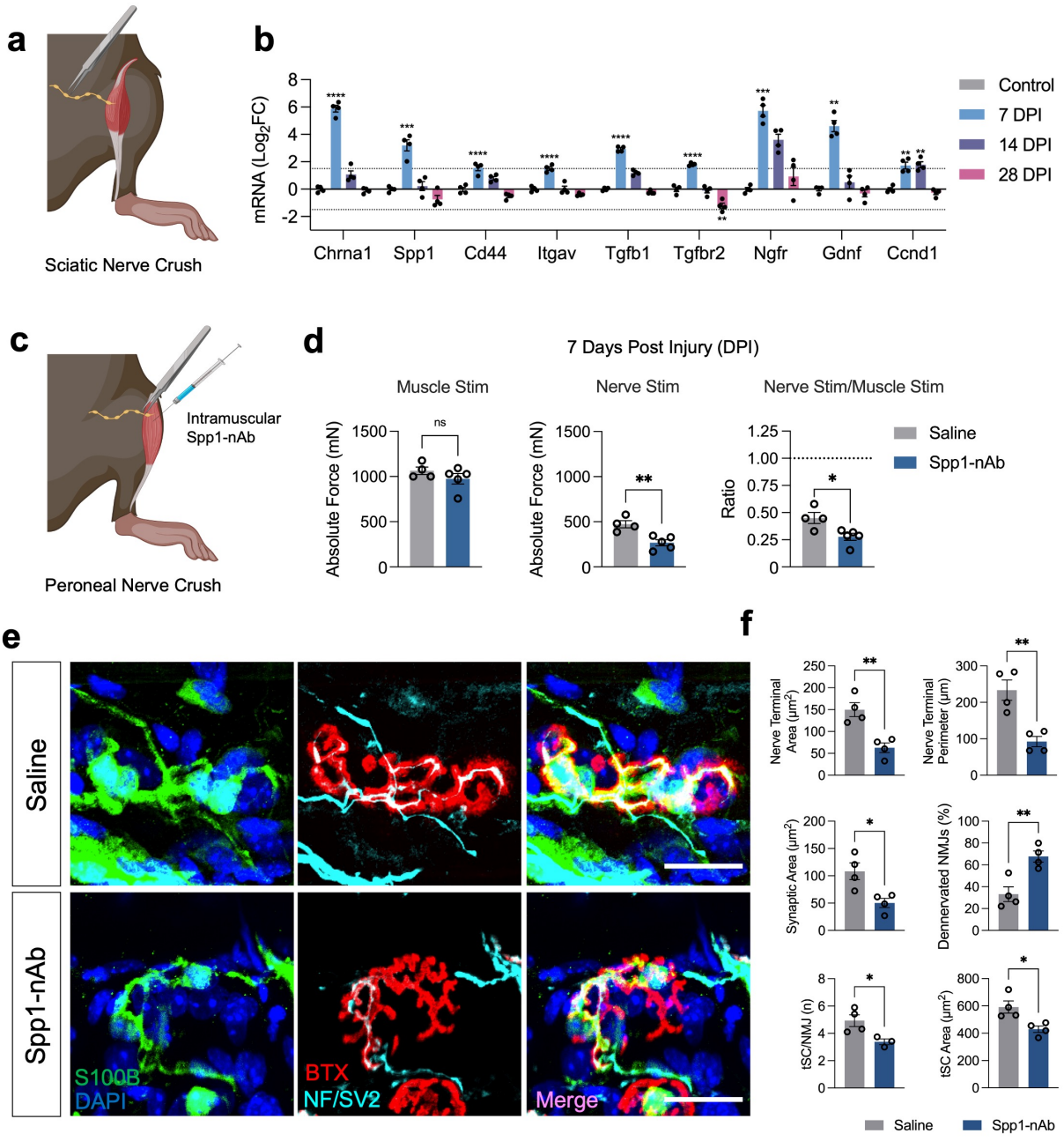
a
Sciatic Nerve Crush
b
mRNA (Log2FC)
Control
7 DPI
14 DPI
28 DPI
Chrna1
Spp1
Cd44
Itgav
Tgfb1
Tgfbr2
Ngfr
Gdnf
Ccnd1
c
Intramuscular
Spp1-nAb
Peroneal Nerve Crush
d
7 Days Post Injury (DPI)
Muscle Stim
Nerve Stim
Nerve Stim/Muscle Stim
Absolute Force (mN)
Ratio
ns
Saline
Spp1-nAb
e
Saline
Spp1-nAb
S100B
DAPI
BTX
NF/SV2
Merge
f
Nerve Terminal Area (μm²)
Nerve Terminal Perimeter (μm)
Synaptic Area (μm²)
Denervated NMJs (%)
tSC/NMJ (n)
tSC Area (μm²)
Saline
Spp1-nAb

Figure 5.3: SPP1 signaling promotes tSC proliferation and muscle fiber reinnervation after nerve injury. a, Sciatic nerve crush injuries were performed, and gastrocnemius (GTN) muscles of C57BL/6 mice were harvested 0 (Control), 7, 14, and 28 days post injury (DPI). **b,** mRNA levels for denervation markers (Chrna1), components of SPP1 signaling (*Spp1, Cd44, Itgav, Tgfb1, Tgfbr2*), genes associated with SC mediated nerve regeneration (Ngfr, Gdnf), and cell proliferation (Ccnd1) at each time point. **c,** Peroneal nerve injuries were induced, and tibialis anterior (TA) muscles were intramuscularly injected with either Spp1-nAb or saline (control) at time of injury and every 2 days thereafter. **d,** Data are shown for force (mN) evoked by direct muscle stimulation, with nerve stimulation, and ratio of force elicited by nerve and direct muscle stimulation at 7 DPI for saline- (gray) and Spp1-nAb-treated (blue) groups. **e,** Representative immunofluorescent images of NMJs at 7 DPI stained with S100B (green), DAPI (Blue), BTX (Red), and NF/SV2 (Cyan). **f,** Quantification of NMJ nerve terminal area and perimeter, synaptic area, percentage of denervated (>10% overlap) NMJs, tSC number and area. Open circles indicate values for individual mice and bars represent the mean across animals ± SEM. Scale bars represent 25 μm. *P ≤ 0.05, **P ≤ 0.01, ***P ≤ 0.001, ****P ≤ 0.0001 by two tailed unpaired t-test (Saline vs Spp1-nAb) or 1-way ANOVA (7, 14, 28 DPI vs Control) for multiple comparisons.

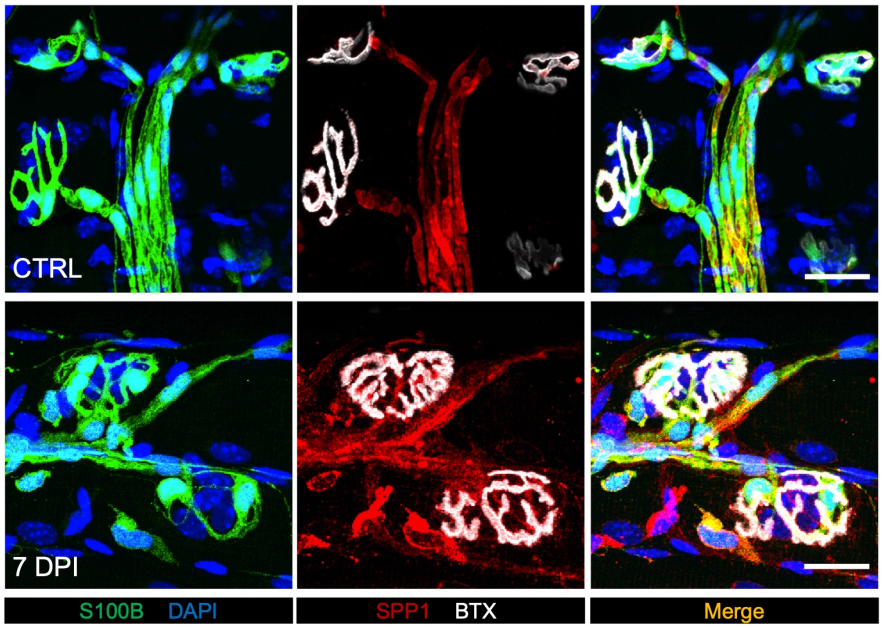

Figure 5.4: Localization of Spp1 Protein within Skeletal Muscle Fibers. Representative immunofluorescent images of muscle fiber bundles from *S100GFP*-tg mice, captured 7 days post-injury (7 DPI) following sciatic nerve crush, juxtaposed with non-injured controls (CTRL). The staining showcases S100B (Green), SPP1 (Red), BTX (White), and DAPI (Blue). Scale bar represents 25 μm.

5.5 Discussion

Our data also demonstrate that this reactive phenotype is underpinned by an intricate SPP1 signaling mechanism, bridging myelin Schwann cells and tSCs. Our observations of marked

elevations in both SPP1 gene expression and protein immunofluorescence in the acute phase post muscle denervation is consistent with prior reports of induction of Spp1 in samples from nerve injury patients[198], and we show for the first time that Spp1 expression has functional relevance for the efficacy and/or efficiency of the response of tSCs to effect NMJ reinnervation. This significant conclusion is supported by our observations of increased tSC numbers following peroneal nerve injury that were notably decreased following intramuscular administration of an Spp1-nAb resulting in a diminished synaptic contact area, a pronounced percentage of denervated NMJs, and impaired recovery of functional innervation. Collectively, our findings suggest a pivotal role of SPP1 signaling, facilitated by myelin Schwann cells, in regulating tSC proliferation and reinnervation of denervated NMJs.

While upregulation of SPP1 in muscles of patients suffering from Duchenne Muscular Dystrophy (DMD)[200] and in mice following exercise[199] has been reported, our study uncovers a novel cellular origin contributing to this signaling — originating from muscle-resident myelin Schwann cells, rather than or perhaps in addition to macrophages targeting Fibro/adipogenic progenitors (FAPs)[199,201,202]. The strong induction of SPP1 signaling pathway transcripts we observed concurrent with intense Spp1 immunofluorescence in skeletal muscle after nerve injury suggests Spp1 may have multiple functions to mediate muscle reinnervation. Integral to muscle reinnervation is Wallerian degeneration, a process governed by dynamic interactions among immune cells, FAPs, and Schwann cells. Thus, it is reasonable to hypothesize that SPP1 engages with multiple cell types in response to severe nerve trauma, such as nerve crush or nerve transection, to facilitate myelin clearance, ECM remodeling, and axon regeneration. In contrast, our observations, based on both imaging for protein and scRNA-Seq, of no significant Spp1 signaling stemming from immune cells in muscles of *Sod1*$^{-/-}$ mice disrupts conventional

understanding of SPP1 signaling in muscle. These findings open the door for additional studies of the necessity for engaging immune cells during transient physiological innervation remodeling. Spp1 signaling between glial cell subtypes is further supported by recent investigations showing elevated levels of SPP1 in nerve samples post-injury, which positively correlated with Schwann cell proliferation and survival[198]. Furthermore, SPP1 has neuroprotective roles in the eye and is expressed by reactive astrocytes to promote retinal ganglion cell survival after traumatic optic nerve damage[204]. Beyond this regenerative aspect, SPP1 is implicated in pathological contexts, including tumor growth and metastasis, highlighting its versatility and likely the complexity of its regulation in promoting cell survival and growth in various contexts and cell types.

Overall, our research deepens the existing knowledge on the intricate cellular processes of NMJ regeneration orchestrated by Schwann cells. Specifically, we highlight the importance of SPP1 signaling and elucidate the distinct roles played by specialized subtypes of muscle-resident Schwann cells.

Chapter 6 Conclusions and Future Work

The goal of this dissertation was to fill knowledge gaps relating to the cell biology and physiology of muscle-resident Schwann cells and whether alterations in the regulation of these or perhaps other proliferating cells limit motor unit expansion and/or reinnervation in conditions associated with disruption of muscle fiber innervation. These conditions include traumatic injury, neuromuscular degenerative disease, and normal aging. Through a combination of in vivo and in vitro investigations, the research described in the dissertation elucidates the roles of key cellular players and signaling pathways in neuromuscular junction (NMJ) maintenance and repair.

In Chapter 2, we focus on proliferating cells, in general, and the impact of cellular senescence on skeletal muscle function. By employing a genetic model to eliminate p16-expressing senescent cells in aged mice, the study presents evidence for a modest contribution of the presence of senescent cells to the modulation of skeletal muscle health. Since the publication of this study, additional research has emerged, shedding more light on this area. Notably, a study using a combination of senolytic drugs, Dasatinib and Quercetin (DQ), demonstrated efficacy in reducing the expression of genes associated with senescence in female mice and implicated FAPs as the primary cell undergoing cellular senescence[105]. However, when this approach was applied to human subjects, examining vastus lateralis muscle biopsies from elderly women and men treated with DQ, the results were less pronounced. These human studies revealed only modest changes in skeletal muscle, primarily marked by decreased expression of *Gadd45A* and *Runx1*. One of the challenges highlighted in this research is the low abundance of *p16* transcripts in skeletal muscle

tissue, which makes it challenging to evaluate the specific effects of removing senescent cells through isolated muscle biopsies. Additionally, the application of findings from human muscle biopsies may not comprehensively represent the dynamics of other proliferative cell types, such as Schwann cells. This is partly due to the non-uniform distribution of these cells within the muscle tissue, which complicates the extrapolation of data from muscle biopsies to broader cellular phenomena in neuromuscular physiology.

Based on the contributions of NMJ degeneration and denervation-induced fiber loss to sarcopenia[7,205] and the importance of Schwann cell proliferation for the maintenance of muscle fiber innervation[43], the remainder of the dissertation turns to examination of the support and regeneration of neuromuscular synapses through the lens of the Schwann cells. In vitro experiments described in Chapter 3 build on reports[71,75] of a significant role of reactive oxygen species (ROS) as regulators of Schwann cell phenotype. Earlier studies have established the significant role of ROS in triggering the de-differentiation of Schwann cells, a necessary precursor for nerve and NMJ repair[71,75]. Building upon these findings, our in vitro experiments used primary rat Schwann cells and extended the exposure to ROS-inducing agents to 48 hours, significantly longer than the one-hour duration used in the earlier studies. This prolonged treatment period allows for a more thorough investigation into how Schwann cells respond to sustained oxidative stress. We observed that extended exposure to ROS-inducing agents led to the upregulation of essential markers of nerve repair and NMJ organization, such as GDNF, NGFR, and AGRN. Moreover, the study shows that conditioned media from ROS-activated Schwann cells significantly enhance post-synaptic AChR clustering in differentiated myotubes, indicating a direct Schwann cell-to-muscle signaling axis that facilitates NMJ organization. This finding aligns with previous research, such as a study demonstrating that rat nerve–muscle co-cultures treated

with SC-CM exhibited notably larger AChR clusters compared to controls. This correlation with existing literature underscores the growing understanding of the intricate interactions at the NMJ, particularly the influence of Schwann cells on synaptic structure and function.[206]. Despite this progress, critical questions remain. Notably, the precise biochemical mechanisms by which Schwann cell-derived factors mediate their effects to enhance AChR clustering are yet to be elucidated. Additionally, it is essential to explore how the secretion of Schwann cell-derived factors are modulated under different physiological and pathological conditions, such as aging, injury, or disease states, to fully appreciate their role in maintaining neuromuscular health.

Chapters 4 and 5 move to in vivo analyses of muscle-resident Schwann cells, with a particular emphasis on terminal Schwann cells (tSCs), during NMJ remodeling. Utilizing a novel genetic mouse model deficient in Sod1 and expressing GFP in Schwann cells, the research identifies a crucial 'regenerative window' in early adulthood, optimal for studying the dynamics of NMJ remodeling and Schwann cell responses. Chapter 4 describes how partial denervation and NMJ remodeling coincide with an increased number of tSCs and the emergence of a novel synapse-promoting Schwann cell subtype. This discovery suggests a pivotal role for these cells in NMJ regeneration and improved neuromuscular transmission. In addition, intercellular communication analysis identified elevated SPP1 signaling from myelin Schwann cells in 2-month-old *Sod1*$^{-/-}$ mice. This signaling was inferred to target tSCs expressing CD44 and ITGA5, suggesting a novel interaction that may drive tSC proliferation and muscle reinnervation.

Finally, Chapter 5 extends these bioinformatic intercellular communication analysis to validate the importance of SPP1 signaling to facilitate muscle fiber reinnervation. Using temporary recoverable nerve injury models in wild-type mice, we showed acute, transient spikes in SPP1 signaling post-injury. Subsequent experiments demonstrated that inhibiting SPP1 signaling

resulted in diminished muscle reinnervation and a reduction in tSC numbers at the NMJ. These findings underscore a previously unrecognized role of SPP1 in NMJ regeneration and highlight the importance of Schwann cell-mediated mechanisms in maintaining neuromuscular function.

Overall, this dissertation offers crucial insights into the cellular and molecular mechanisms underpinning the health and repair of neuromuscular junctions, which hold potential for developing therapies for neuromuscular disorders like Sarcopenia. Building on the discoveries made, future research should aim to delve deeper into the dynamics of muscle-resident Schwann cells following muscle denervation. Several potential avenues that warrant future studies are described in the remainder of this chapter.

Identifying novel signaling pathways between Schwann cells and skeletal muscle fibers

The investigation into direct intercellular signaling between Schwann cells and muscle fibers remains a relatively uncharted area in neuromuscular research. To date, only a limited number of studies have addressed this critical aspect of cellular communication[40–42,138,207]. One of the main challenges in this field is the scarcity of terminal Schwann cells (tSCs) within the skeletal muscle milieu and the technical challenge of disrupting the strong association of Schwann cells to nerve axons. High-throughput transcriptomic techniques, such as single nuclei RNA Sequencing (snRNA-Seq), have consistently isolated far fewer tSCs compared to other cell types and myonuclei present in skeletal muscle[208–211]. This disparity poses significant hurdles in conducting comprehensive bioinformatic analyses to unravel direct intercellular signaling pathways between Schwann cells and muscle fibers.

To overcome these limitations and gain a more accurate insight into the signaling landscape between Schwann cells and muscle fibers, future research should consider leveraging S100GFP-

tg mice. These mice, engineered to express GFP in Schwann cells, provide a unique opportunity to selectively enrich GFP+ cells. Isolating nuclei from these enriched cells, alongside the isolation of whole skeletal muscle nuclei would allow researchers to employ snRNA-Seq to achieve a more representative and detailed analysis of intercellular communication. This approach would enable the identification of key signaling pathways that are critical for sustaining neuromuscular health and functionality.

Dissecting muscle-resident Schwann cell dynamics in aged mice

A decline in Schwann cell function with aging is associated with declining neuromuscular health that warrants further exploration. Recent research presents conflicting findings about the presence and behavior of terminal Schwann cells (tSCs) in aged muscles. While the Snyder-Warwick Lab observed a decrease in tSC numbers in older mice[212], a recent study reported more tSC counts in aged extensor digitorum longus (EDL) and soleus muscles compared young but noted a reduction in their coverage of the NMJ[213]. Regardless of these discrepancies in tSC numbers, a broader consensus emerges from bulk RNA sequencing data of isolated Schwann cells from aged mice[52,213]. These data reveal a distinctive upregulation of pro-inflammatory molecules in aged tSCs compared to young tSCs, in mouse muscles from S100B-GFP;NG2-DsRed mice. Intriguingly, genes typically associated with synaptogenesis or those activated in repair Schwann cells do not appear to be upregulated in aged tSCs or aged Schwann cells extracted from injured nerves compared to young mice and rats, respectively[52,213]. This pattern indicates a potential shift in the functional role of Schwann cells during aging, away from regeneration and repair. This diminished functionality could be a key factor in the progression of age-associated neuromuscular degeneration. Given these insights, future research should focus on in-depth single-cell multiomic

analyses of muscle-resident Schwann cells from both young and old skeletal muscles. Such studies would involve assessing the epigenomic and transcriptomic landscapes to identify specific pathways that are altered during aging.

Determine the role of SPP1 in age-associated neuromuscular degeneration

The research presented in this dissertation emphasizes the significance of SPP1 signaling in NMJ regeneration, particularly in the context of partially denervated muscles in *Sod1*$^{-/-}$ mice and WT mice post-nerve injury. Our scRNA-Seq data, complemented by histological analyses, suggest that muscle-resident Schwann cells are key contributors to SPP1-mediated signaling. However, considering the substantial increase in SPP1 expression following injury and the established role of macrophages in SPP1 signaling in muscular dystrophies[200–202], it is plausible that macrophages also play a significant role in the SPP1 signaling network, alongside Schwann cells.

Given the age-related prevalence of partial muscle denervation and the emergence of a role for SPP1 in muscle repair, future research should focus on the responsiveness of tSCs to SPP1 signaling in the context of aging. It is reasonable to hypothesize that while SPP1 signaling may remain elevated in the partially denervated milieu of aged muscles, the expression of SPP1 receptors on tSCs could be diminished. Such a reduction in receptor expression might lead to decreased responsiveness of tSCs to SPP1, potentially contributing to their impaired proliferative capacity and, subsequently, to inadequate NMJ regeneration in aging muscles.

Addressing this hypothesis will require a series of focused studies. A longitudinal analysis to track and quantify the expression levels of SPP1 and its receptors, such as CD44 and ITGA5, across different ages in both healthy and denervated muscle tissues, will be crucial. This approach

would shed light on the changes in Schwann cell-specific SPP1 signaling associated with aging and denervation. Additionally, advanced molecular imaging techniques like fluorescence in situ hybridization (FISH) or immunohistochemistry should be employed to profile the expression of SPP1 receptors on tSCs in aged muscle tissues. This would help identify potential changes in receptor dynamics contributing to altered SPP1 responsiveness during aging.

Moreover, experimenting with animal models to manipulate the SPP1 signaling pathway within aged muscles in vivo would be insightful. This could involve strategies to enhance receptor expression on tSCs or to adjust the levels of SPP1 within the muscles. Assessing the impact of these interventions on muscle reinnervation and NMJ regeneration could illuminate the therapeutic potential of targeting SPP1 signaling in age-related neuromuscular conditions.

Collectively, this research framework aims to dissect the complexities of SPP1 signaling in aging muscles, particularly focusing on its interactions with tSCs and the wider neuromuscular system. The insights gained from this research, informed by the findings of this dissertation, could be pivotal in developing targeted approaches to mitigate age-associated neuromuscular degeneration and bolster the regenerative capacity of the neuromuscular system.

Deciphering the role of increased ROS in Schwann cells in contributing to neuromuscular degeneration

Previous studies, including those from our laboratory and collaborators, have demonstrated that *Sod1*$^{-/-}$ mice exhibit progressive neuromuscular degeneration beginning at around six months of age. Intriguingly, research has also shown that specific interventions, such as expressing Sod1 in motor neurons or expressing catalase into skeletal muscle in these *Sod1*$^{-/-}$ mice, can mitigate the

neuromuscular degenerative phenotype[214,215]. These findings suggest the presence of a critical ROS threshold in skeletal muscle, beyond which neuromuscular degeneration is triggered.

This hypothesis raises the question of whether modulating ROS levels specifically in muscle-resident Schwann cells could alleviate skeletal muscle degeneration under conditions of elevated oxidative stress. To investigate this, a tailored genetic model could be employed, featuring the overexpression of catalase or Sod1 specifically in Schwann cells within the *Sod1*$^{-/-}$ mouse model. Such an approach would allow for a detailed examination of the impact of ROS modulation in Schwann cells on the overall neuromuscular health.

Further expanding on this line of inquiry, it would be valuable to conditionally overexpress these antioxidant proteins in Schwann cells in wild-type adult mice. This experiment would provide insights into whether enhancing the antioxidant capacity of Schwann cells in a typical aging scenario could preserve their functionality and potentially delay or prevent neuromuscular degeneration. Conducting longitudinal studies in these genetically modified animals could shed light on the long-term effects of enhanced ROS-scavenging in Schwann cells and its implications for maintaining neuromuscular junction integrity and muscle health in aging.

Bibliography

1. Crimmins, E. M. Lifespan and Healthspan: Past, Present, and Promise. *Gerontologist* **55**, 901–911 (2015).
2. Moore, A. Z. *et al.* Difference in Muscle Quality over the Adult Life Span and Biological Correlates in the Baltimore Longitudinal Study of Aging. *J Am Geriatr Soc* **62**, 230–236 (2014).
3. von Haehling, S., Morley, J. E. & Anker, S. D. An overview of sarcopenia: Facts and numbers on prevalence and clinical impact. *J Cachexia Sarcopenia Muscle* **1**, 129–133 (2010).
4. Goates, S. *et al.* Economic Impact of Hospitalizations in US Adults with Sarcopenia. *Journal of Frailty and Aging* **8**, 93–99 (2019).
5. Xie, Z. *et al.* Cellular and subcellular localization of PDE10A, a striatum-enriched phosphodiesterase. *Neuroscience* **139**, 597–607 (2006).
6. Valdez, G. *et al.* Attenuation of age-related changes in mouse neuromuscular synapses by caloric restriction and exercise. *Proc Natl Acad Sci U S A* **107**, 14863–14868 (2010).
7. Moreira-Pais, A., Ferreira, R., Oliveira, P. A. & Duarte, J. A. A neuromuscular perspective of sarcopenia pathogenesis: deciphering the signaling pathways involved. *Geroscience* **44**, 1199–1213 (2022).

8. Gonzalez-Freire, M., de Cabo, R., Studenski, S. A. & Ferrucci, L. The Neuromuscular Junction: Aging at the Crossroad between Nerves and Muscle. *Front Aging Neurosci* **6**, 208 (2014).

9. Sanes, J. R. & Lichtman, J. W. DEVELOPMENT OF THE VERTEBRATE NEUROMUSCULAR JUNCTION. *https://doi.org/10.1146/annurev.neuro.22.1.389* **22**, 389–442 (2003).

10. Godfrey, E. W., Nitkin, R. M., Wallace, B. G., Rubin, L. L. & Mcmahan, U. J. *Components of Torpedo Electric Organ and Muscle That Cause Aggregation of Acetylcholine Receptors on Cultured Muscle Cells*. http://rupress.org/jcb/article-pdf/99/2/615/1642981/615.pdf (1984).

11. Weatherbee, S. D., Anderson, K. V. & Niswander, L. A. LDL-receptor-related protein 4 is crucial for formation of the neuromuscular junction. *Development* **133**, 4993–5000 (2006).

12. Zhang, W., Coldefy, A.-S., Hubbard, S. R. & Burden, S. J. Agrin Binds to the N-terminal Region of Lrp4 Protein and Stimulates Association between Lrp4 and the First Immunoglobulin-like Domain in Muscle-specific Kinase (MuSK) * □ S. *Journal of Biological Chemistry* **286**, 40624–40630 (2011).

13. Ohkawara, B. *et al.* LRP4 third b-propeller domain mutations cause novel congenital myasthenia by compromising agrin-mediated MuSK signaling in a position-specific manner. (2013) doi:10.1093/hmg/ddt578.

14. Dechiara, T. M. & Bowen, D. C. The Receptor Tyrosine Kinase MuSK Is Required for Neuromuscular Junction Formation In Vivo. *Cell* **85**, 501–512 (1996).

15. Bishop, D. L., Misgeld, T., Walsh, M. K., Gan, W.-B. & Lichtman, J. W. *Axon Branch Removal at Developing Synapses by Axosome Shedding tensively here. Multiple motor*

neurons initially send branches that converge at each muscle fiber's synaptic site (Balice-Gordon and Lichtman, 1990; Brown et al. *Neuron* vol. 44 http://www.neuron.org/cgi/content/full/44/4/651/ (2004).

16. Missias, A. C., Chu, G. C., Klocke, B. J., Sanes, J. R. & Merlie, J. P. Maturation of the Acetylcholine Receptor in Skeletal Muscle: Regulation of the AChR γ-to-ϵ Switch. *Dev Biol* **179**, 223–238 (1996).
17. Cetin, H., Beeson, D., Vincent, A. & Webster, R. The Structure, Function, and Physiology of the Fetal and Adult Acetylcholine Receptor in Muscle. *Front Mol Neurosci* **13**, (2020).
18. Sanes, J. R. & Lichtman, J. W. Induction, assembly, maturation and maintenance of a postsynaptic apparatus. *Nat Rev Neurosci* **2**, 791–805 (2001).
19. Balice-Gordon, R. J., Chua, C. K., Nelson, C. C. & Lichtman, J. W. Gradual loss of synaptic cartels precedes axon withdrawal at developing neuromuscular junctions. *Neuron* **11**, 801–815 (1993).
20. Prakash, Y. S., Miller, S. M., Huang, M. & Sieck, G. C. *Morphology of diaphragm neuromuscular junctions on different fibre types*. *Journal of Neurocytology* vol. 25 (1996).
21. Stanley, E. F. & Drachman, D. B. Denervation accelerates the degradation of junctional acetylcholine receptors. *Exp Neurol* **73**, 390–396 (1981).
22. Lyons, P. R. & Slater, C. R. Structure and function of the neuromuscular junction in young adult mdx mice. *J Neurocytol* **20**, 969–981 (1991).
23. Iyer, S. R., Shah, S. B. & Lovering, R. M. The Neuromuscular Junction: Roles in Aging and Neuromuscular Disease. *International Journal of Molecular Sciences 2021, Vol. 22, Page 8058* **22**, 8058 (2021).

24. Hepple, R. T. & Rice, C. L. The Journal of Physiology Innervation and neuromuscular control in ageing skeletal muscle. *The Authors. The Journal of Physiology C* **594**, 1965–1978 (2016).

25. Heckman, C. J. & Enoka, R. M. Motor Unit. *Compr Physiol* **2**, 2629–2682 (2012).

26. Milner-Brown, H. S., Stein, R. B. & Yemm, R. The orderly recruitment of human motor units during voluntary isometric contractions. *J Physiol* **230**, 359–370 (1973).

27. Erminio, F., Buchthal, F. & Rosenfalck, P. Motor unit territory and muscle fiber concentration in paresis due to peripheral nerve injury and anterior horn cell involvement. *Neurology* **9**, 657–657 (1959).

28. C Kiernan DSc, A. M. *et al.* Seminar Amyotrophic lateral sclerosis. *Lancet* **377**, 942–55 (2011).

29. Brown, M. C. & Ironton, R. Sprouting and regression of neuromuscular synapses in partially denervated mammalian muscles. *J Physiol* **278**, 325–348 (1978).

30. Galganski, M. E., Fuglevand, A. J. & Enoka, R. M. Reduced control of motor output in a human hand muscle of elderly subjects during submaximal contractions. *https://doi.org/10.1152/jn.1993.69.6.2108* **69**, 2108–2115 (1993).

31. Erim, Z., Beg, M. F., Burke, D. T. & De Luca, C. J. Effects of aging on motor-unit control properties. *J Neurophysiol* **82**, 2081–2091 (1999).

32. Semmler, J. G., Steege, J. W., Kornatz, K. W. & Enoka, R. M. Motor-unit synchronization is not responsible for larger motor-unit forces in old adults. *J Neurophysiol* **84**, 358–366 (2000).

33. R. Deschenes, M. Motor Unit and Neuromuscular Junction Remodeling with Aging. *Current Aging Sciencee* **4**, 209–220 (2012).

34. Gordon, T., Thomas, C. K., Munson, J. B. & Stein, R. B. The resilience of the size principle in the organization of motor unit properties in normal and reinnervated adult skeletal muscles. *https://doi.org/10.1139/y04-081* **82**, 645–661 (2011).

35. Hegedus, J., Putman, C. T. & Gordon, T. Time course of preferential motor unit loss in the SOD1G93A mouse model of amyotrophic lateral sclerosis. *Neurobiol Dis* **28**, 154–164 (2007).

36. Sulaiman, W. & Gordon, T. Neurobiology of Peripheral Nerve Injury, Regeneration, and Functional Recovery: From Bench Top Research to Bedside Application. *Ochsner J* **13**, 100 (2013).

37. Sunderland, S. A CLASSIFICATION OF PERIPHERAL NERVE INJURIES PRODUCING LOSS OF FUNCTION. *Brain* **74**, 491–516 (1951).

38. Liu, P. *et al.* Role of macrophages in peripheral nerve injury and repair. *Neural Regen Res* **14**, 1335–1342 (2019).

39. Martins, R. S., Bastos, D., Siqueira, M. G., Heise, C. O. & Teixeira, M. J. Traumatic injuries of peripheral nerves: a review with emphasis on surgical indication. *Arq Neuropsiquiatr* **71**, 811–814 (2013).

40. Robitaille, R. Modulation of Synaptic Efficacy and Synaptic Depression by Glial Cells at the Frog Neuromuscular Junction. *Neuron* **21**, 847–855 (1998).

41. Castonguay, A. & Robitaille, R. Differential Regulation of Transmitter Release by Presynaptic and Glial Ca2+ Internal Stores at the Neuromuscular Synapse. *Journal of Neuroscience* **21**, 1911–1922 (2001).

42. Todd, K. J., Darabid, H. & Robitaille, R. Perisynaptic glia discriminate patterns of motor nerve activity and influence plasticity at the neuromuscular junction. *Journal of Neuroscience* **30**, 11870–11882 (2010).

43. Love, F. M. & Thompson, W. J. *Schwann Cells Proliferate at Rat Neuromuscular Junctions during Development and Regeneration*. (1998).

44. Kang, H., Tian, L., Mikesh, M., Lichtman, J. W. & Thompson, W. J. Terminal schwann cells participate in neuromuscular synapse remodeling during reinnervation following nerve injury. *Journal of Neuroscience* **34**, 6323–6333 (2014).

45. Son, Y. J. & Thompson, W. J. Schwann cell processes guide regeneration of peripheral axons. *Neuron* **14**, 125–132 (1995).

46. Höke, A. *et al.* Glial Cell Line-Derived Neurotrophic Factor Alters Axon Schwann Cell Units and Promotes Myelination in Unmyelinated Nerve Fibers. *Journal of Neuroscience* **23**, 561–567 (2003).

47. Trupp, M. *et al.* Peripheral expression and biological activities of GDNF, a new neurotrophic factor for avian and mammalian peripheral neurons. *Journal of Cell Biology* **130**, 137–148 (1995).

48. Braun, S., Croizat, B., Lagrange, M. C., Waiter, J. M. & Poindron, P. Neurotrophins increase motoneurons' ability to innervate skeletal muscle fibers in rat spinal cord-human muscle cocultures. *J Neurol Sci* **136**, 17–23 (1996).

49. Springer, J. E. *et al.* cDNA sequence and differential mRNA regulation of two forms of glial cell line-derived neurotrophic factor in Schwann cells and rat skeletal muscle. *Exp Neurol* **131**, 47–52 (1995).

50. Zhao, C., Veltri, K., Li, S., Bain, J. R. & Fahnestock, M. NGF, BDNF, NT-3, and GDNF mRNA Expression in Rat Skeletal Muscle following Denervation and Sensory Protection. *https://home.liebertpub.com/neu* **21**, 1468–1478 (2004).

51. Nguyen, Q. T., Parsadanian, A. S., Snider, W. D. & Lichtman, J. W. Hyperinnervation of neuromuscular junctions caused by GDNF overexpression in muscle. *Science (1979)* **279**, 1725–1729 (1998).

52. Painter, M. W. *et al.* Diminished Schwann cell repair responses underlie age-associated impaired axonal regeneration. *Neuron* **83**, 331–343 (2014).

53. Taetzsch, T. & Valdez, G. NMJ maintenance and repair in aging. *Current Opinion in Physiology* vol. 4 57–64 Preprint at https://doi.org/10.1016/j.cophys.2018.05.007 (2018).

54. Sousa-Victor, P. *et al.* Geriatric muscle stem cells switch reversible quiescence into senescence. *Nature 2014 506:7488* **506**, 316–321 (2014).

55. Dun, X. P. & Parkinson, D. B. Role of Netrin-1 Signaling in Nerve Regeneration. *International Journal of Molecular Sciences 2017, Vol. 18, Page 491* **18**, 491 (2017).

56. Curtis, R. *et al.* GAP-43 is expressed by nonmyelin-forming Schwann cells of the peripheral nervous system. *Journal of Cell Biology* **116**, 1455–1464 (1992).

57. Sun, K. L. W., Correia, J. P. & Kennedy, T. E. Netrins: versatile extracellular cues with diverse functions. *Development* **138**, 2153–2169 (2011).

58. Keino-Masu, K. *et al.* Deleted in Colorectal Cancer (DCC) Encodes a Netrin Receptor. *Cell* **87**, 175–185 (1996).

59. Rosenberg, A. F., Isaacman-Beck, J., Franzini-Armstrong, C. & Granato, M. Schwann Cells and Deleted in Colorectal Carcinoma Direct Regenerating Motor Axons Towards Their Original Path. *Journal of Neuroscience* **34**, 14668–14681 (2014).

60. Meijers, R., Smock, R. G., Zhang, Y. & Wang, J. H. Netrin Synergizes Signaling and Adhesion through DCC. *Trends Biochem Sci* **45**, 6–12 (2020).

61. Webber, C. A. *et al.* Schwann cells direct peripheral nerve regeneration through the Netrin-1 receptors, DCC and Unc5H2. *Glia* **59**, 1503–1517 (2011).

62. Goslin, K., Schreyer, D. J., Skene, J. H. P. & Banker, G. Development of neuronal polarity: GAP-43 distinguishes axonal from dendritic growth cones. *Nature 1988 336:6200* **336**, 672–674 (1988).

63. Benowitz, L. I. & Routtenberg, A. GAP-43: an intrinsic determinant of neuronal development and plasticity. *Trends Neurosci* **20**, 84–91 (1997).

64. Aigner, L. *et al.* Overexpression of the Neural Growth-Associated Protein GAP-43 Induces Nerve Sprouting in the Adult Nervous System of Transgenic Mice. *Cell* **83**, 269–278 (1995).

65. Maier, D. L. *et al.* Disrupted cortical map and absence of cortical barrels in growth-associated protein (GAP)-43 knockout mice. *Proc Natl Acad Sci U S A* **96**, 9397–9402 (1999).

66. Denny, J. B. Molecular Mechanisms, Biological Actions, and Neuropharmacology of the Growth-Associated Protein GAP-43. *Curr Neuropharmacol* **4**, 293 (2006).

67. Strittmatter, S. M., Cannon, S. C., Ross, E. M., Higashijima, T. & Fishman, M. C. GAP-43 augments G protein-coupled receptor transduction in Xenopus laevis oocytes. *Proc Natl Acad Sci U S A* **90**, 5327 (1993).

68. Holahan, M. R. A shift from a pivotal to supporting role for the growth-associated protein (GAP-43) in the coordination of axonal structural and functional plasticity. *Front Cell Neurosci* **11**, 282924 (2017).

69. Jessen, K. R., Mirsky, R. & Lloyd, A. C. Schwann Cells: Development and Role in Nerve Repair. *Cold Spring Harb Perspect Biol* **7**, 1–15 (2015).

70. Jessen, K. R. & Mirsky, R. Negative regulation of myelination: Relevance for development, injury, and demyelinating disease. *Glia* **56**, 1552–1565 (2008).

71. Duregotti, E. *et al.* Mitochondrial alarmins released by degenerating motor axon terminals activate perisynaptic schwann cells. *Proc Natl Acad Sci U S A* **112**, E497–E505 (2015).

72. Burdon, R. H., Gill, V. & Rice-Evans, C. Oxidative Stress and Tumour Cell Proliferation. *Free Radic Res Commun* **11**, 65–76 (1990).

73. Burdon, R. H., Gill, V. & Rice-Evans, C. Cell proliferation and oxidative stress. *Free Radic Res* **7**, 149–159 (1989).

74. Day, A. M. *et al.* Inactivation of a Peroxiredoxin by Hydrogen Peroxide Is Critical for Thioredoxin-Mediated Repair of Oxidized Proteins and Cell Survival. *Mol Cell* **45**, 398–408 (2012).

75. Negro, S. *et al.* Hydrogen peroxide is a neuronal alarmin that triggers specific RNAs, local translation of Annexin A2, and cytoskeletal remodeling in Schwann cells. *RNA* **24**, 915–925 (2018).

76. Zhang, W., Liu, H. T. & Tu, H. *MAPK signal pathways in the regulation of cell proliferation in mammalian cells*. *Cell Research* http://www.cell-research.com (2002).

77. Sun, Y. *et al.* Signaling pathway of MAPK/ERK in cell proliferation, differentiation, migration, senescence and apoptosis. *Journal of Receptors and Signal Transduction* **35**, 600–604 (2015).

78. Harrisingh, M. C. *et al.* The Ras/Raf/ERK signalling pathway drives Schwann cell dedifferentiation. *EMBO J* **23**, 3061 (2004).

79. Napoli, I. *et al.* A central role for the ERK-signaling pathway in controlling Schwann cell plasticity and peripheral nerve regeneration in vivo. *Neuron* **73**, 729–742 (2012).

80. Lindwall Blom, C., Mårtensson, L. B. & Dahlin, L. B. Nerve injury-induced c-jun activation in schwann cells is JNK independent. *Biomed Res Int* **2014**, (2014).

81. Jessen, K. R. & Mirsky, R. The success and failure of the schwann cell response to nerve injury. *Front Cell Neurosci* **13**, 1–14 (2019).

82. Chao, M. V. Neurotrophins and their receptors: A convergence point for many signalling pathways. *Nature Reviews Neuroscience 2003 4:4* **4**, 299–309 (2003).

83. Hempstead, B. L. Deciphering proneurotrophin actions. *Handb Exp Pharmacol* **220**, 17–32 (2014).

84. Roux, P. P. & Barker, P. A. Neurotrophin signaling through the p75 neurotrophin receptor. *Prog Neurobiol* **67**, 203–233 (2002).

85. Boyd, J. G. & Gordon, T. Neurotrophic Factors and Their Receptors in Axonal Regeneration and Functional Recovery after Peripheral Nerve Injury. *Mol Neurobiol* **27**, 277–323 (2003).

86. Khursigara, G. *et al.* A Prosurvival Function for the p75 Receptor Death Domain Mediated via the Caspase Recruitment Domain Receptor-Interacting Protein 2. *The Journal of Neuroscience* **21**, 5854 (2001).

87. Harrington, A. W., Kim, J. Y. & Yoon, S. O. Activation of Rac GTPase by p75 Is Necessary for c-jun N-Terminal Kinase-Mediated Apoptosis. *Journal of Neuroscience* **22**, 156–166 (2002).

88. Taveggia, C. Schwann cells–axon interaction in myelination. *Curr Opin Neurobiol* **39**, 24–29 (2016).

89. Hayflick, L. & Moorhead, P. S. The serial cultivation of human diploid cell strains. *Exp Cell Res* **25**, 585–621 (1961).

90. Coppé, J. P., Desprez, P. Y., Krtolica, A. & Campisi, J. The Senescence-Associated Secretory Phenotype: The Dark Side of Tumor Suppression. *https://doi.org/10.1146/annurev-pathol-121808-102144* **5**, 99–118 (2010).

91. Saito, Y. & Chikenji, T. S. Diverse Roles of Cellular Senescence in Skeletal Muscle Inflammation, Regeneration, and Therapeutics. *Front Pharmacol* **12**, 739510 (2021).

92. Zhu, Y. *et al.* The Achilles' heel of senescent cells: from transcriptome to senolytic drugs. *Aging Cell* **14**, 644–658 (2015).

93. Guzman, S. D. *et al.* Removal of p16 INK4 Expressing Cells in Late Life has Moderate Beneficial Effects on Skeletal Muscle Function in Male Mice. *Frontiers in Aging* **2**, 821904 (2021).

94. López-Otín, C., Blasco, M. A., Partridge, L., Serrano, M. & Kroemer, G. The hallmarks of aging. *Cell* **153**, 1194 (2013).

95. Ferrucci, L., Hesdorffer, C., Bandinelli, S. & Simonsick, E. M. Frailty as a Nexus Between the Biology of Aging ,. **32**, 475–488.

96. Ori, A. *et al.* Integrated Transcriptome and Proteome Analyses Reveal Organ-Specific Proteome Deterioration in Old Rats. *Cell Syst* **1**, 224–237 (2015).

97. Schaum, N. *et al.* Ageing hallmarks exhibit organ-specific temporal signatures. *Nature* **583**, 596–602 (2020).

98. Bortz, W. M. A conceptual framework of frailty: A review. *Journals of Gerontology - Series A Biological Sciences and Medical Sciences* **57**, 283–288 (2002).

99. Cesari, M., Pahor, M. Target population for clinical trials. *Journal of Nutrition, Health and Aging* **13**, 729–732 (2009).

100. Valdez, G. *et al.* Attenuation of age-related changes in mouse neuromuscular synapses by caloric restriction and exercise. *Proc Natl Acad Sci U S A* **107**, 14863–14868 (2010).

101. Di Micco, R., Krizhanovsky, V., Baker, D. & d'Adda di Fagagna, F. Cellular senescence in ageing: from mechanisms to therapeutic opportunities. *Nat Rev Mol Cell Biol* **22**, 75–95 (2021).

102. Faget, D. V, Ren, Q. & Stewart, S. A. Unmasking senescence: context-dependent effects of SASP in cancer. *Nat Rev Cancer* **19**, 439–453 (2019).

103. Baker, D. J. *et al.* Naturally occurring p16 Ink4a-positive cells shorten healthy lifespan. *Nature* **530**, 184–189 (2016).

104. Xu, M. *et al.* Senolytics improve physical function and increase lifespan in old age. *Nat Med* **24**, 1246–1256 (2018).

105. Zhang, X. *et al.* Characterization of cellular senescence in aging skeletal muscle. *Nature Aging 2022 2:7* **2**, 601–615 (2022).

106. Sousa-Victor, P. *et al.* Geriatric muscle stem cells switch reversible quiescence into senescence. *Nature* **506**, 316–321 (2014).

107. García-Prat, L. *et al.* Autophagy maintains stemness by preventing senescence. *Nature* **529**, 37–42 (2016).

108. Demaria, M. *et al.* An essential role for senescent cells in optimal wound healing through secretion of PDGF-AA. *Dev Cell* **31**, 722–733 (2014).

109. Laberge, R.-M. *et al.* Mitochondrial DNA damage induces apoptosis in senescent cells. *Cell Death Dis* **4**, e727 (2013).

110. Brooks, S. V & Faulkner, J. A. Contractile properties of skeletal muscles from young, adult and aged mice. *J Physiol* **404**, 71–82 (1988).

111. Mayeuf-Louchart, A. *et al.* MuscleJ: a high-content analysis method to study skeletal muscle with a new Fiji tool. *Skelet Muscle* **8**, 25 (2018).

112. da Silva, P. F. L. *et al.* The bystander effect contributes to the accumulation of senescent cells in vivo. *Aging Cell* **18**, (2019).

113. Von Zglinicki, T., Wan, T. & Miwa, S. Senescence in Post-Mitotic Cells: A Driver of Aging? *Antioxid Redox Signal* **34**, 308–323 (2021).

114. Wang, Y. X. & Rudnicki, M. A. Satellite cells, the engines of muscle repair. *Nature reviews. Molecular cell biology* vol. 13 127–133 Preprint at https://doi.org/10.1038/nrm3265 (2011).

115. Abou-Khalil, R. *et al.* Role of muscle stem cells during skeletal regeneration. *Stem Cells* **33**, 1501–1511 (2015).

116. Verdijk, L. B. *et al.* Satellite cell content is specifically reduced in type II skeletal muscle fibers in the elderly. *Am J Physiol Endocrinol Metab* **292**, E151-7 (2007).

117. Verdijk, L. B. *et al.* Satellite cells in human skeletal muscle; from birth to old age. *Age (Dordr)* **36**, 545–547 (2014).

118. Kumari, R. & Jat, P. Mechanisms of Cellular Senescence: Cell Cycle Arrest and Senescence Associated Secretory Phenotype. *Front Cell Dev Biol* **9**, 645593 (2021).

119. Yousefzadeh, M. J. *et al.* Tissue specificity of senescent cell accumulation during physiologic and accelerated aging of mice. *Aging Cell* **19**, e13094 (2020).

120. Mitchell, W. K. *et al.* Sarcopenia, dynapenia, and the impact of advancing age on human skeletal muscle size and strength; a quantitative review. *Front Physiol* **3**, 260 (2012).

121. Tidball, J. G. & Villalta, S. A. Regulatory interactions between muscle and the immune system during muscle regeneration. *Am J Physiol Regul Integr Comp Physiol* **298**, R1173-87 (2010).

122. Chazaud, B. Inflammation and Skeletal Muscle Regeneration: Leave It to the Macrophages! *Trends Immunol* **41**, 481–492 (2020).

123. Yun, M. H. Cellular senescence in tissue repair: every cloud has a silver lining. *Int J Dev Biol* **62**, 591–604 (2018).

124. Da Silva-Álvarez, S. *et al.* Cell senescence contributes to tissue regeneration in zebrafish. *Aging Cell* **19**, e13052 (2020).

125. Wang, Y., Wehling-Henricks, M., Samengo, G. & Tidball, J. G. Increases of M2a macrophages and fibrosis in aging muscle are influenced by bone marrow aging and negatively regulated by muscle-derived nitric oxide. *Aging Cell* **14**, 678–688 (2015).

126. Saito, Y., Chikenji, T. S., Matsumura, T., Nakano, M. & Fujimiya, M. Exercise enhances skeletal muscle regeneration by promoting senescence in fibro-adipogenic progenitors. *Nat Commun* **11**, 1–16 (2020).

127. Di Micco, R., Krizhanovsky, V., Baker, D. & d'Adda di Fagagna, F. Cellular senescence in ageing: from mechanisms to therapeutic opportunities. *Nat Rev Mol Cell Biol* **22**, 75–95 (2021).

128. Farr, J. N. *et al.* Targeting cellular senescence prevents age-related bone loss in mice. *Nat Med* **23**, 1072–1079 (2017).

129. Dungan, C. M. *et al.* Deletion of SA β-Gal+ cells using senolytics improves muscle regeneration in old mice. *Aging Cell* (2021) doi:10.1111/acel.13528.

130. Sies, H. & Jones, D. P. Reactive oxygen species (ROS) as pleiotropic physiological signalling agents. *Nature Reviews Molecular Cell Biology 2020 21:7* **21**, 363–383 (2020).

131. Pizzino, G. *et al.* Oxidative Stress: Harms and Benefits for Human Health. *Oxid Med Cell Longev* **2017**, (2017).

132. HARMAN, D. Aging: A Theory Based on Free Radical and Radiation Chemistry. *J Gerontol* **11**, 298–300 (1956).

133. Paiva, C. N. & Bozza, M. T. Are Reactive Oxygen Species Always Detrimental to Pathogens? *Antioxid Redox Signal* **20**, 1000 (2014).

134. Zhang, J. *et al.* ROS and ROS-Mediated Cellular Signaling. *Oxid Med Cell Longev* **2016**, (2016).

135. Miller, I. P., Pavlović, I., Poljšak, B., Šuput, D. & Milisav, I. Beneficial Role of ROS in Cell Survival: Moderate Increases in H2O2 Production Induced by Hepatocyte Isolation Mediate Stress Adaptation and Enhanced Survival. *Antioxidants* **8**, (2019).

136. Muller, F. L. *et al.* Denervation-induced skeletal muscle atrophy is associated with increased mitochondrial ROS production. *Am J Physiol Regul Integr Comp Physiol* **293**, 1159–1168 (2007).

137. Forman, H. J. & Zhang, H. Targeting oxidative stress in disease: promise and limitations of antioxidant therapy. *Nature Reviews Drug Discovery 2021 20:9* **20**, 689–709 (2021).

138. Auld, D. S. & Robitaille, R. Glial cells and neurotransmission: an inclusive view of synaptic function. *Neuron* **40**, 389–400 (2003).

139. Vincent, A. M., Kato, K., McLean, L. L., Soules, M. E. & Feldman, E. L. Sensory Neurons and Schwann Cells Respond to Oxidative Stress by Increasing Antioxidant Defense Mechanisms. *Antioxid Redox Signal* **11**, 425 (2009).

140. Siironen, J., Collan, Y. & Röyttä, M. Axonal reinnervation does not influence Schwann cell proliferation after rat sciatic nerve transection. *Brain Res* **654**, 303–311 (1994).

141. Chen, B., Chen, Q., Parkinson, D. B. & Dun, X. P. Analysis of Schwann Cell Migration and Axon Regeneration Following Nerve Injury in the Sciatic Nerve Bridge. *Front Mol Neurosci* **12**, 499927 (2019).

142. Lingappan, K. NF-κB in oxidative stress. *Curr Opin Toxicol* **7**, 81–86 (2018).

143. Lo, Y. Y. C., Wong, J. M. S. & Cruz, T. F. Reactive Oxygen Species Mediate Cytokine Activation of c-Jun NH2-terminal Kinases. *Journal of Biological Chemistry* **271**, 15703–15707 (1996).

144. Zochodne, D. W. THE MICROENVIRONMENT OF INJURED AND REGENERATING PERIPHERAL NERVES. (2000) doi:10.1002/1097-4598(2000)999:9.

145. Yang, J. F., Cao, G., Koirala, S., Reddy, L. V. & Ko, C. P. Schwann cells express active agrin and enhance aggregation of acetylcholine receptors on muscle fibers. *Journal of Neuroscience* **21**, 9572–9584 (2001).

146. Wang, C. Y. *et al.* Regulation of neuromuscular synapse development by glial cell line-derived neurotrophic factor and neurturin. *Journal of Biological Chemistry* **277**, 10614–10625 (2002).

147. Glass, D. J. *et al.* Agrin acts via a MuSK receptor complex. *Cell* **85**, 513–523 (1996).

148. Sugiura, Y. & Lin, W. Neuron–glia interactions: the roles of Schwann cells in neuromuscular synapse formation and function. *Biosci Rep* **31**, 295–302 (2011).

149. Fischer, L. R. *et al.* Amyotrophic lateral sclerosis is a distal axonopathy: Evidence in mice and man. *Exp Neurol* **185**, 232–240 (2004).

150. Killian, J. M., Wilfong, A. A., Burnett, L., Appel, S. H. & Boland, D. Decremental motor responses to repetitive nerve stimulation in ALS. *Muscle Nerve* **17**, 747–754 (1994).

151. Santosa, K. B., Keane, A. M., Jablonka-Shariff, A., Vannucci, B. & Snyder-Warwick, A. K. Clinical relevance of terminal Schwann cells: An overlooked component of the neuromuscular junction. *Journal of Neuroscience Research* vol. 96 1125–1135 Preprint at https://doi.org/10.1002/jnr.24231 (2018).

152. Jablonka-Shariff, A., Balta, E., Santosa, K. B., Lu, C. Y. & Snyder-Warwick, A. K. Terminal Schwann Cells Are Essential for Neuromuscular Junction Function and Recovery after Nerve Injury. *Plast Reconstr Surg* **151**, 792–803 (2023).

153. Ahn, B. *et al.* Scavenging mitochondrial hydrogen peroxide by peroxiredoxin 3 overexpression attenuates contractile dysfunction and muscle atrophy in a murine model of accelerated sarcopenia. *Aging Cell* **21**, (2022).

154. Su, Y. *et al.* Transgenic expression of SOD1 specifically in neurons of Sod1 deficient mice prevents defects in muscle mitochondrial function and calcium handling. *Free Radic Biol Med* **165**, 299–311 (2021).

155. Larouche, J. A. *et al.* Murine muscle stem cell response to perturbations of the neuromuscular junction are attenuated with aging. *Elife* **10**, (2021).

156. Sataranatarajan, K. *et al.* Molecular changes in transcription and metabolic pathways underlying muscle atrophy in the CuZnSOD null mouse model of sarcopenia. *Geroscience* **42**, 1101–1118 (2020).

157. Goldman, D., Brenner, H. R. & Heinemann, S. *Acetylcholine Receptor a-, p-, y-, and &Subunit mRNA levels Are Regulated by Muscle Activity*. *Neuron* vol. 1 (1988).

158. Ma, J. *et al.* Gene expression of myogenic regulatory factors, nicotinic acetylcholine receptor subunits, and GAP-43 in skeletal muscle following denervation in a rat model. *Journal of Orthopaedic Research* **25**, 1498–1505 (2007).

159. Zuo, Y. *et al.* Fluorescent Proteins Expressed in Mouse Transgenic Lines Mark Subsets of Glia, Neurons, Macrophages, and Dendritic Cells for Vital Examination. *Journal of Neuroscience* **24**, 10999–11009 (2004).

160. Huang, T.-T. *et al. Superoxide-Mediated Cytotoxicity in Superoxide Dismutase-Deficient Fetal Fibroblasts The importance of CuZnSOD and MnSOD in pro*. *ARCHIVES OF BIOCHEMISTRY AND BIOPHYSICS* vol. 344 (1997).

161. Larkin, L. M. *et al.* Skeletal muscle weakness due to deficiency of CuZn-superoxide dismutase is associated with loss of functional innervation. *Am J Physiol Regul Integr Comp Physiol* **301**, R1400-7 (2011).

162. Burkholder, T. J., Fingado, B., Baron, S. & Lieber, R. L. Relationship between muscle fiber types and sizes and muscle architectural properties in the mouse hindlimb. *J Morphol* **221**, 177–190 (1994).

163. Jones, R. A. *et al.* Correction to NMJ-morph reveals principal components of synaptic morphology influencing structure - Function relationships at the neuromuscular junction (Open Biology (2016) 6 (160240) DOI: 10.1098/rsob.160335). *Open Biology* vol. 7 Preprint at https://doi.org/10.1098/rsob.160240 (2017).

164. Dobin, A. *et al.* STAR: ultrafast universal RNA-seq aligner. *Bioinformatics* **29**, 15–21 (2013).

165. Butler, A., Hoffman, P., Smibert, P., Papalexi, E. & Satija, R. Integrating single-cell transcriptomic data across different conditions, technologies, and species. *Nature Biotechnology 2018 36:5* **36**, 411–420 (2018).

166. Yang, S. *et al.* Decontamination of ambient RNA in single-cell RNA-seq with DecontX. *Genome Biol* **21**, (2020).

167. Wu, T. *et al.* clusterProfiler 4.0: A universal enrichment tool for interpreting omics data. *The Innovation* **2**, 100141 (2021).

168. Jin, S. *et al.* Inference and analysis of cell-cell communication using CellChat. *Nat Commun* **12**, (2021).

169. Personius, K. E. & Sawyer, R. P. Variability and failure of neurotransmission in the diaphragm of mdx mice. *Neuromuscular Disorders* **16**, 168–177 (2006).

170. Missias, A. C., Chu, G. C., Klocke, B. J., Sanes, J. R. & Merlie, J. P. Maturation of the Acetylcholine Receptor in Skeletal Muscle: Regulation of the AChR γ-to-ϵ Switch. *Dev Biol* **179**, 223–238 (1996).

171. Bezakova, G. & Ruegg, M. A. New insights into the roles of agrin. *Nature Reviews Molecular Cell Biology 2003 4:4* **4**, 295–309 (2003).

172. Gerdes, J. *et al. CELL CYCLE ANALYSIS OF A CELL PROLIFERATION-ASSOCIATED HUMAN NUCLEAR ANTIGEN DEFINED BY THE MONOCLONAL ANTIBODY Ki-67'. THE JOURNAL OF IMMUNOLOGY* vol. 133 http://journals.aai.org/jimmunol/article-pdf/133/4/1710/1031649/1710.pdf (1984).

173. Sherr, C. J. D-type cyclins. *Trends Biochem Sci* **20**, 187–190 (1995).

174. Atanasoski, S., Shumas, S., Dickson, C., Scherer, S. S. & Suter, U. Differential Cyclin D1 Requirements of Proliferating Schwann Cells during Development and after Injury. *Molecular and Cellular Neuroscience* **18**, 581–592 (2001).

175. Britsch, S. *et al.* The transcription factor Sox10 is a key regulator of peripheral glial development. *Genes Dev* **15**, 66–78 (2001).

176. Perry, V. H., Brown, M. C. & Gordon, S. BriefDefinitive Report THE MACROPHAGE RESPONSE TO CENTRAL AND PERIPHERAL NERVE INJURY A Possible Role for Macrophages in Regeneration.

177. Aigner, L. *et al. Overexpression of the Neural Growth-Associated Protein GAP-43 Induces Nerve Sprouting in the Adult Nervous System of Transgenic Mice*. *Cell* vol. 83 (1995).

178. Serafini, T. *et al.* The netrins define a family of axon outgrowth-promoting proteins homologous to C. elegans UNC-6. *Cell* **78**, 409–424 (1994).

179. Petrenko, V., Mihhailova, J., Salmon, P. & Kiss, J. Z. Apoptotic neurons induce proliferative responses of progenitor cells in the postnatal neocortex. *Exp Neurol* **273**, 126–137 (2015).

180. Gerber, D. *et al.* Transcriptional profiling of mouse peripheral nerves to the single-cell level to build a sciatic nerve atlas (Snat). *Elife* **10**, (2021).

181. Castro, R. *et al.* Specific labeling of synaptic schwann cells reveals unique cellular and molecular features. *Elife* **9**, (2020).

182. Proietti, D. *et al.* Activation of skeletal muscle-resident glial cells upon nerve injury. *JCI Insight* **6**, (2021).

183. Procacci, N. M. *et al.* Kir4.1 is specifically expressed and active in non-myelinating Schwann cells. *Glia* **71**, 926–944 (2023).

184. Gorlewicz, A. *et al.* CD44 is expressed in non-myelinating Schwann cells of the adult rat, and may play a role in neurodegeneration-induced glial plasticity at the neuromuscular junction. *Neurobiol Dis* **34**, 245–258 (2009).

185. Lee, K. E. *et al.* Positive feedback loop between Sox2 and Sox6 inhibits neuronal differentiation in the developing central nervous system. *Proc Natl Acad Sci U S A* **111**, 2794–2799 (2014).

186. Stolt, C. C. *et al.* SoxD Proteins Influence Multiple Stages of Oligodendrocyte Development and Modulate SoxE Protein Function. *Dev Cell* **11**, 697–709 (2006).

187. Ittner, E. *et al.* SoxD transcription factor deficiency in Schwann cells delays myelination in the developing peripheral nervous system. *Sci Rep* **11**, (2021).

188. Shen, Y., Mani, S., Donovan, S. L., Schwob, J. E. & Meiri, K. F. Growth-Associated Protein-43 Is Required for Commissural Axon Guidance in the Developing Vertebrate Nervous System. *Journal of Neuroscience* **22**, 239–247 (2002).

189. Hung, C. C. *et al.* Astrocytic GAP43 Induced by the TLR4/NF-κB/STAT3 Axis Attenuates Astrogliosis-Mediated Microglial Activation and Neurotoxicity. *Journal of Neuroscience* **36**, 2027–2043 (2016).

190. Woolf, C. J. *et al. Denervation of the Motor Endplate Results in the Rapid Expression by Terminal Schwann Cells of the Growth-associated Protein GAP-43*. *The Journal of Neuroscience* vol. 12 (1992).

191. Watson, D. C. *et al.* GAP43-dependent mitochondria transfer from astrocytes enhances glioblastoma tumorigenicity. *Nat Cancer* **4**, 648–664 (2023).

192. Smith, G. M. & Gallo, G. The role of mitochondria in axon development and regeneration. *Dev Neurobiol* **78**, 221–237 (2018).

193. Lv, J. *et al.* Netrin-1 induces the migration of Schwann cells via p38 MAPK and PI3K-Akt signaling pathway mediated by the UNC5B receptor. *Biochem Biophys Res Commun* **464**, 263–268 (2015).

194. Meltzer, S. *et al.* A role for axon-glial interactions and Netrin-G1 signaling in the formation of low-threshold mechanoreceptor end organs. (2022) doi:10.1073/pnas.

195. Yang, D. P. *et al.* Schwann cell proliferation during Wallerian degeneration is not necessary for regeneration and remyelination of the peripheral nerves: Axon-dependent removal of newly generated Schwann cells by apoptosis. *Molecular and Cellular Neuroscience* **38**, 80–88 (2008).

196. Vannucci, B. *et al.* What is Normal? Neuromuscular junction reinnervation after nerve injury. *Muscle Nerve* **60**, 604–612 (2019).

197. Taylor, J. S. H. & Bampton, E. T. W. Factors secreted by Schwann cells stimulate the regeneration of neonatal retinal ganglion cells. *J Anat* **204**, 25 (2004).

198. Wang, J. B. *et al.* SPP1 promotes Schwann cell proliferation and survival through PKCα by binding with CD44 and αvβ3 after peripheral nerve injury. *Cell Biosci* **10**, (2020).

199. Liu, L. *et al.* Exercise reprograms the inflammatory landscape of multiple stem cell compartments during mammalian aging. *Cell Stem Cell* **30**, 689-705.e4 (2023).

200. Pegoraro, E. *et al.* SPP1 genotype is a determinant of disease severity in Duchenne muscular dystrophy. *Neurology* **76**, 219–226 (2011).

201. Vetrone, S. A. *et al.* Osteopontin promotes fibrosis in dystrophic mouse muscle by modulating immune cell subsets and intramuscular TGF-β. *Journal of Clinical Investigation* **119**, 1583–1594 (2009).

202. Coulis, G. *et al. Single-cell and spatial transcriptomics identify a macrophage population associated with skeletal muscle fibrosis*. https://www.science.org (2023).

203. Capote, J. *et al.* Osteopontin ablation ameliorates muscular dystrophy by shifting macrophages to a pro-regenerative phenotype. *Journal of Cell Biology* **213**, 275–288 (2016).

204. Li, S. & Jakobs, T. C. Secreted phosphoprotein 1 slows neurodegeneration and rescues visual function in mouse models of aging and glaucoma. *Cell Rep* **41**, (2022).

205. Mitchell, W. K. *et al.* Sarcopenia, dynapenia, and the impact of advancing age on human skeletal muscle size and strength; a quantitative review. *Front Physiol* **3**, 260 (2012).

206. Feng, Z. & Ko, C. P. Schwann cells promote synaptogenesis at the neuromuscular junction via transforming growth factor-β1. *Journal of Neuroscience* **28**, 9599–9609 (2008).

207. Darabid, H., St-Pierre-See, A. & Robitaille, R. Purinergic-Dependent Glial Regulation of Synaptic Plasticity of Competing Terminals and Synapse Elimination at the Neuromuscular Junction. *Cell Rep* **25**, 2070-2082.e6 (2018).

208. Orchard, P. *et al.* Human and rat skeletal muscle single-nuclei multiomic integrative analyses nominate causal cell types, regulatory elements, and SNPs for complex traits. *Genome Res* **31**, 2258–2276 (2021).

209. Jing, Y. *et al.* Single-nucleus profiling unveils a geroprotective role of the FOXO3 in primate skeletal muscle aging. *Protein Cell* **14**, 499–514 (2023).

210. Dos Santos, M. *et al.* Single-nucleus RNA-seq and FISH identify coordinated transcriptional activity in mammalian myofibers. *Nature Communications 2020 11:1* **11**, 1–16 (2020).

211. Petrany, M. J. *et al.* Single-nucleus RNA-seq identifies transcriptional heterogeneity in multinucleated skeletal myofibers. *Nature Communications 2020 11:1* **11**, 1–12 (2020).

212. Snyder-Warwick, A. K. *et al.* Hypothalamic Sirt1 protects terminal Schwann cells and neuromuscular junctions from age-related morphological changes. *Aging Cell* **17**, e12776 (2018).

213. Hastings, R. L. *et al.* Cellular and molecular evidence that synaptic Schwann cells contribute to aging of mouse neuromuscular junctions. *Aging Cell* **22**, e13981 (2023).

214. Xu, H., Ranjit, R., Richardson, A. & Van Remmen, H. Muscle mitochondrial catalase expression prevents neuromuscular junction disruption, atrophy, and weakness in a mouse model of accelerated sarcopenia. *J Cachexia Sarcopenia Muscle* **12**, 1582–1596 (2021).

215. Sakellariou, G. K. *et al.* Neuron-specific expression of CuZnSOD prevents the loss of muscle mass and function that occurs in homozygous CuZnSOD-knockout mice. *FASEB J* **28**, 1666–1681 (2014).